THE EFFECT OF TOPOGRAPHY ON THE SEISMIC WAVEFIELD

By

Ulrika Miller

RECOMMENDED:

Dr. Douglas Christensen

Dr. Michael West

Dr. Carl Tape
Advisory Committee Chair

Dr. Paul McCarthy
Chair, Department of Geosciences

APPROVED:

Dr. Paul Layer
Dean, College of Natural Science and Mathematics

Dr. John Eichelberger
Dean of the Graduate School

12/7/14

Date

THE EFFECT OF TOPOGRAPHY ON THE SEISMIC WAVEFIELD

A

THESIS

Presented to the Faculty

of the University of Alaska Fairbanks

in Partial Fulfillment of the Requirements

for the Degree of

MASTER OF SCIENCE

By

Ulrika Miller, B.S.

Fairbanks, Alaska

December 2014

Abstract

Active tectonic settings exhibit deformation manifested by earthquakes and by strong topographic variations due to erosion and uplift. Seismic waves from these earthquakes will clearly be influenced by the topographic variations, but it is challenging to isolate the effects of topography from the effects of variations in 3D seismic wave-speed structure. Here we design a realistic numerical experiment to investigate the effects of topography on the regional seismic wavefield. We choose southern California as a target region. We perform several sets of 3D seismic wavefield simulations for 137 earthquake sources ranging from M_{w} 3.4 to 5.4. We test the influence of topography within a homogeneous model and a layered model, and for each model we establish the shortest resolvable period for each path between a source and station. By examining the path-specific shortest resolvable periods, we are able to make some generalizations. Topography has the strongest influence on surface waves, particularly for waveforms with travel paths that are nodal to the source radiation; in these directions, the wave amplitudes are relatively low, so any multi-pathing or scattering effects due to topography are more easily identified. The topographic effects are stronger for shorter periods and for longer paths. The influence of topography on the seismic waveforms arises from both the change in the topographic surface, but also the change in the wave-speed structure that arises from perturbing the topography for a 1D (or 3D) wave-speed model. These generalizations of the influence of topography provide a basis for further numerical investigations or for where to search within a regional set of observations for the topographic effects. Topography should be included within simulation-based seismic imaging applications, especially those at high frequencies, in order to eliminate the possibility of attributing topographically-caused waveforms to subsurface variations in structure.

Table of Contents

List of Figures

Page

Page

Page

List of Tables

Acknowledgements

This work was supported in part by a grant of HPC resources from the Arctic Region Supercomputing Center at the University of Alaska Fairbanks (UAF) where we conducted the computational earthquake simulations. I am thankful for the financial support from the UAF Graduate School for a thesis completion fellowship, from the Society of Exploration Geophysics, from teaching assistantships from the UAF Department of Geosciences, and from the National Science Foundation (grant EAR 1215959). I also appreciate the financial support from the Geophysical Society of Alaska, ConocoPhillips Alaska, and British Petroleum Alaska. Several figures have been created using Generic Mapping Tools (*Wessel and Smith*, 1991). I thank Carl Tape for providing data and for advising the study. I thank my additional thesis committee members, Douglas Christensen and Michael West, for their comments and suggestions over the course of this study.

Chapter 1
Introduction

Topography can significantly influence earthquake ground motion (e.g., *Geli et al.*, 1988; *Hartzell et al.*, 1994). There are other structures within the Earth that can also influence ground motion: large-scale crustal heterogeneities, such as sedimentary basins (*Guidotti et al.*, 2011), small-scale crustal heterogeneities (*Frankel and Clayton*, 1986), and complexity associated with faults or the earthquake rupture (*Pyrak-Nolte et al.*, 1990; *Dunham et al.*, 2011). However, these quantities are difficult to determine from observations of ground motion recorded by seismometers on the surface of the Earth. The topographic variations at the surface also influence earthquake ground motion. Topographic data are readily available with relatively high resolution (e.g., *Lee et al.*, 2009) and low uncertainties. The objective of this study is to quantify the effects of topography on the seismic wavefield by performing a series of seismic wavefield simulations within relatively simple wave-speed models. Our same methodology can be readily extended to models with 3D variations in wave speeds.

To make our investigation as realistic as possible, we choose a region with active tectonics that exhibits a broad range of earthquakes, as well as strong topographic variations: southern California, including the offshore region (Figure 1.1). This region has a relief of almost 9 km, from -4.2 km below sea level (west and oceanward of the continental shelf) to 3.9 km above sea level (the Sierra Nevada). The slope of topography provides a perspective on the regions where topography changes the most rapidly (Figure 1.2). This large range in vertical variation should, in theory, impart stronger influences on the seismic wavefield, allowing us to better analyze the effects of topography. The topography in this region is characterized by a power law (Appendix A.1), which is a normal occurrence for the Earth topography. An additional reason for selecting southern California is that there are existing high-quality earthquake models and also 3D wave-speed models that produce synthetic seismograms with good agreement with observations (e.g., *Komatitsch et al.*, 2004; *Tape et al.*, 2009a). By performing our investigation in southern California, we will provide a possible step toward the ultimate goal of identifying the topographic effects within observed seismograms in structurally complex settings.

The underlying equation that is solved in this study is the 3D seismic wave equation. The complexity of the models of interest, such as those with realistic topographic surfaces, require numerical solutions, as analytical solutions do not exist. Different numerical methods have been developed to calculate seismic wave propagation. Finite difference methods (FDM) are widely used and employ a set of grid points to approximate spatial and temporal derivatives of the wave equation (*Shearer*, 2009). Another approach is the pseudospectral method that solves the wave equation by transforming it into generalized coordinates (*Carcione*, 1994). However, both methods

cannot handle sharp variations in topography or accommodate free-surface boundary conditions well (*Komatitsch and Tromp*, 1999). The pseudospectral method also needs quite regular meshes which leads to difficulty in computational parallelization (*Dumbser and Käser*, 2006).

The finite element method (FEM) solves the wave equation by dividing the model into a series of volume element and approximates the solution by a polynomial (*Shearer*, 2009). The Discontinuous Galerkin method (DGM) is an adaptation of FEM where the solution across the element interfaces can be discontinuous (*Dumbser and Käser*, 2006). The disadvantage of FEM and Galerkin methods is that both require extensive computational costs to solve large linear systems of equations (*Komatitsch and Tromp*, 1999). Finite volume is able to utilize either FDM or FEM schemes by honoring relevant conservation laws (*Latychev et al.*, 2005). This method assess the fluid-solid boundary problem that exists in the weak formulation of FDM and FEM and reduces the computational costs compared to a low-order FDM. On the other hand, simulations that use unstructured meshes face challenges in obtaining accurate waveforms (*Brossier et al.*, 2008). The spectral element method (SEM) is an application of local spectral methods to finite-element meshes, whereby the underlying discretization of grid points on the mesh is designed to optimize the solution to the wave equation (*Komatitsch and Tromp*, 1999). Similarly to FEM, this method can accommodate free surface, topography, and other geological discontinuities (*Komatitsch et al.*, 2004). Another advantage of this method is that it can handle very distorted mesh elements and mesh size variation (*Peter et al.*, 2011). For seismological applications, SEM has been successfully implemented for 3D global and regional scale simulations (*Komatitsch et al.*, 2002, 2004). Additionally, it is well suited to parallel implementations on large clusters (*Carrington et al.*, 2008; *Peter et al.*, 2011).

Advances in high-performance computing (*Komatitsch et al.*, 2002) have allowed seismologists to incorporate realistic topographic surfaces into 3D structural models (*Komatitsch et al.*, 2004; *Lee et al.*, 2008). Performing simulations with realistic ground surface variations is desirable because topography influences ground motion (*Lee et al.*, 2014). Topography can strongly influence wave propagation, especially for surface waves and at high frequencies (*Lee et al.*, 2008, 2009). The topographic effects is more pronounced for surface waves than it is for body waves, which do not interact much with the surface (*Ma et al.*, 2007).

Specific studies documenting the topographic effect on seismic waves have been demonstrated on a variety of scales and in different regions of the world. *Lee et al.* (2008) confirmed initial studies that the wavefield is amplified on mountain areas and that topography attenuates the amplitudes at high frequencies. He also demonstrated that a mountainous area adjacent to a sedimentary basin can prolong the duration of ground motion (*Lee et al.*, 2009). Topographic ridges can complicate wave propagation by amplification, reflections, and multi-pathing (*Lee et al.*, 2008, 2009). Wavefield complexity also appears in the higher frequency range when numerical simulations are

performed for areas with rough topography or large topographic contrasts (*Rodgers et al.*, 2010; *Köhler et al.*, 2012). Seismic waves are impacted by topography when their wavelengths are comparable to the length scales of topographic features (*Rodgers et al.*, 2010). In southern California, *Ma et al.* (2007) showed that the San Gabriel mountains can influence some ground motions for nearby sites. *Magnoni et al.* (2014) assessed the fit between synthetic and observed seismograms. Her result showed that synthetic waveforms created with topography (in 1D model) can fit the coda part of observed seismograms.

In this study, we build upon previous work by performing a comprehensive investigation of the effects of topography at a regional scale. We use a large number of 137 sources and 315 stations for a total of 43,155 paths. We carefully calculate the numerical accuracy of our synthetic seismograms; this is characterized by the shortest resolvable period for each path. There has been a lack of documentation in the literature on the subject of numerical accuracy (Table 1.1), even though the accuracy of the synthetic wavefield can affect the quantification of topography on the waveforms. The analysis of the topographic effects has been demonstrated in previous studies by quantification of wavefield differences, either from peak ground values or from direct waveform comparisons using a range of misfit measures such as goodness of fit criteria (*Anderson*, 2004) or time-frequency analysis (*Kristeková et al.*, 2006). The goodness of fit criteria are often used in engineering applications. The time-frequency misfit is conducted to measure the level of disagreement by the envelope and phase misfit. *Bielak et al.* (2009) and *Chaljub et al.* (2010) utilized the two misfit analysis to compare their simulation sets that were conducted with different numerical methods. In this study, waveforms calculated with and without topography will be qualitatively compared in time and frequency domain and quantitatively by using a normalized difference. Table 1.1 provides a review of studies that implement topography in their seismic wavefield simulations; the last row shows this study for comparison.

We will begin by outlining the meshing and simulations for creating synthetic wavefields using SEM. We separate the simulations into two distinct steps: creating a hexahedral mesh and then solving the seismic wave equation (*Peter et al.*, 2011). Mesh generation is a critical part of the modeling process in SEM (*Casarotti et al.*, 2008); for our purposes, we generate meshes with and without topography. We utilize CUBIT software (described at https://cubit.sandia.gov/) within a python-based framework called GEOCUBIT (*Casarotti et al.*, 2008) that allows us to semi-automatically generate large meshes using a parallel computing cluster. We then use the software SPECFEM3D (*Komatitsch et al.*, 2004; *Peter et al.*, 2011) to perform a series of earthquake simulations to generate a large database of synthetic seismograms. We then discuss the quantification of shortest resolvable period (Chapter 2) and topographic effects (Chapter 3) for homogeneous and 1D wave-speed models, with and without topography. A comprehensive analysis of results

is presented in Chapter 3, with the key findings summarized in Chapter 4. A glossary of terms related to this study is provided in Table 1.2.

Table 1.1: Summary of numerical simulations that utilize topography. E corresponds to the number of earthquakes is used for the source, and S denotes the number of simulations. *Numres* identifies whether the shortest resolvable period was identified. *Topo effect* identifies whether the effects of topography were investigated. The last row compares this study with previously conducted work.

Authors	Region	Method	Max size (km^3) L × W × H	Relief ≥ 7 km	Max freq (Hz)	E	S	Numres	Topo effects	Real data	Wave speed model 0D	1D	3D
Komatitsch et al. (2004)	southern California	SEM	516 × 507 × 60	–	0.5	2	2	–	Yes	Yes	–	Yes	–
Ma et al. (2007)	southern California	FEM	209.6 × 120 × 36	–	0.5	1	3	–	Yes	–	Yes	–	Yes
Martin et al. (2008)	Asteroid 433-Eros	SEM	34 × 17	–	22	–	2	–	–	–	Yes	–	–
Lee et al. (2008)	northern Taiwan	SEM	87.5 × 101.9 × 100	–	1	1	3	Yes	Yes	Yes	–	–	Yes
Lee et al. (2009)	northern Taiwan	SEM	87.5 × 101.9 × 100	–	1	1	14	–	–	–	–	–	Yes
Stupazzini et al. (2009)	Grenoble Valley	SEM	40.7 × 50 × 8	–	3	1	18	–	–	Yes	–	Yes	–
Bielak et al. (2009)	southern California	FD, FEM	600 × 300 × 84	–	0.5	1	3	–	–	–	–	–	Yes
Rodgers et al. (2010)	North Korea	FD	40 × 40 × 30	–	8	–	22		Yes	–	Yes	–	–
Chaljub et al. (2010)	Grenoble Valley	DGM, FDM, SEM	35 × 35 × 10	–	2	2	8	–	Yes	–	–	–	Yes
Guidotti et al. (2011)	New Zealand	SEM	60 × 60 × 20	–	2	1	3	–	–	Yes	–	Yes	–
Köhler et al. (2012)	northern Norway	SEM	250 × 250 × 40	–	4	–	3	–	Yes	–	Yes	–	–
Lee et al. (2014)	Taiwan	SEM	280 × 428 × 114	Yes	1	1	4	–	–	Yes	–	–	Yes
Magnoni et al. (2014)	central Italy	SEM	200 × 200 × 60	–	5	1	3	–	Yes	Yes	–	Yes	Yes
this study	southern California	SEM	672 × 504 × 400	Yes	1	137	822	Yes	Yes	–	Yes	Yes	–

Table 1.2: Glossary of some terms related to this study.

Term	Definition
GLL	Gauss-Lobatto-Legendre: a quadrature to approximate the integration of a function which is used in the spectral element method (*Komatitsch and Tromp*, 1999). *GLL points* are used interpolate the wavefield in solving the wave equation with the spectral element method.
NGLL	number of GLL points used for an element within a finite-element mesh.
grid point	a discrete point within a numerical grid used to represent 3D models and to solve equations using those models. For us, *grid point* is synonymous with *GLL point*.
element	the base entity of a mesh. For us, all elements are hexahedral and are discretized with GLL grid points.
mesh	a collection of hexahedral elements that define the topological surface containing a seismic wave speed model
coarse mesh	a mesh that uses 5 GLL points for each element; this can be thought of as a coarser-resolution mesh
fine mesh	a mesh that uses 7 GLL points for each element; this can be thought of as a finer-resolution mesh
wave speed model	a representation of the seismic wave speed (V_P and V_S) as a function of space
misfit	a quantification of how different a paired waveform is, either in the shortest resolvable period or in the topographic effect analysis.
shortest resolvable period	the shortest period in a low-pass filter for which a particular synthetic waveform is defined to be accurate (based on some choice of misfit value).
topographic effect	the effect of topography on seismic waveforms. This is quantified by measuring the misfit between waveforms generated in a model with topography and waveforms generated in a model without topography.
core	a single computing unit of a cluster
partition	a portion of the volumetric mesh that is assigned to one core of a multi-core simulation on a cluster. At each time-step in the simulation, information at the boundary of the partitions is exchanged with neighboring partitions.

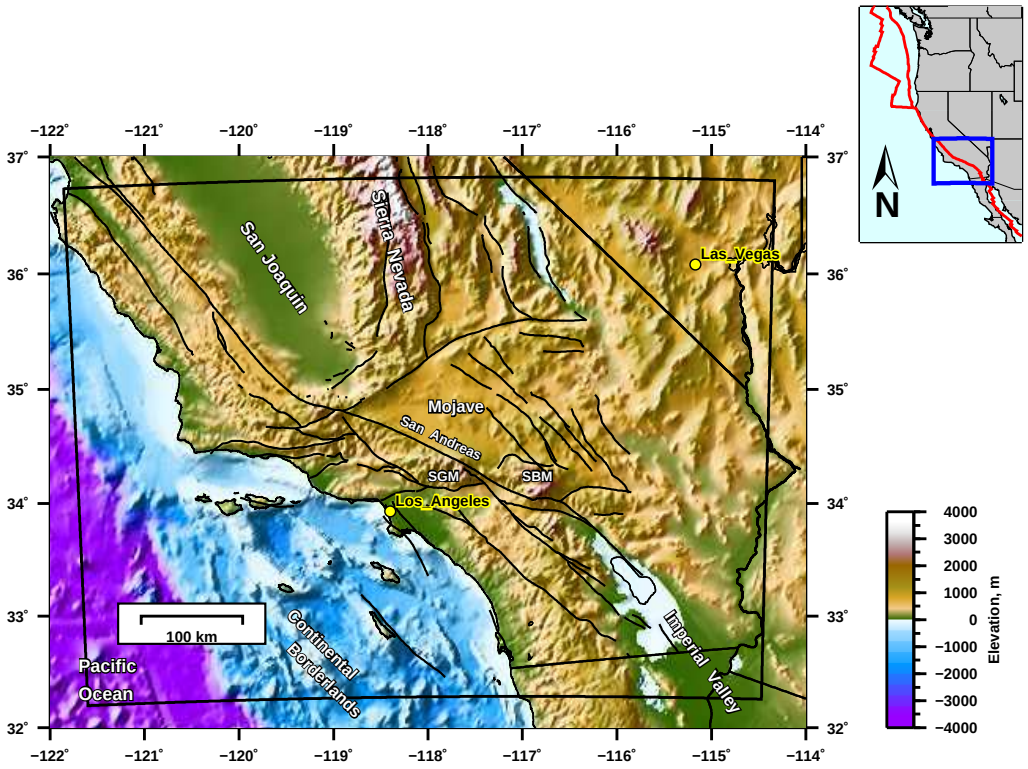

Figure 1.1: Topography in southern California.
The topographic digital elevation model is based on ETOPO-1 and has a resolution of 1 arc-minute, which is about 1.8 km (*Amante and Eakins*, 2009). It ranges from -4.2 km below sea level in the southwest to 3.9 km in the Sierra Nevada. Active faults from *Jennings* (1994) are plotted for reference; the San Andreas fault runs from northwest to southeast. SBM = San Bernardino mountains, SGM = San Gabriel mountains. Our simulation region is shown as the black outline, which is a uniform rectangle in UTM coordinates. The slope of topography is shown in Figure 1.2.

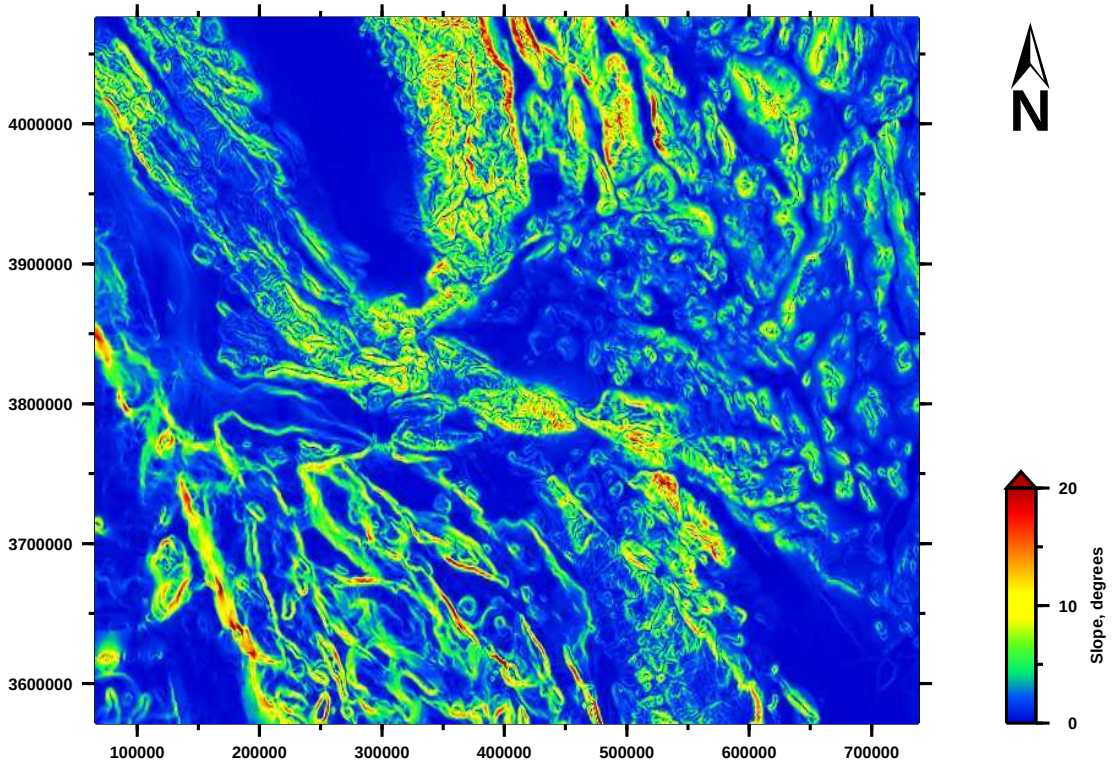

Figure 1.2: The slope of topography in southern California.
The slope angle highlights the strongest changes in the topography of southern California (Figure 1.1). The calculation (and plot) use the UTM projection (zone 11S).

Chapter 2

Meshing, wavefield simulations, and shortest resolvable period

In order to quantify the effects of topography on the seismic wavefield, we choose two different wave-speed models, create hexahedral meshes for these models, and then perform wavefield simulations.

2.1 Choice of wave-speed models

Two different wave-speed models are investigated: a homogeneous model and a 1D (layered) model. The homogeneous model has a shear wave speed (V_S) of 3870 m/s and V_P 6700 m/s (Table 2.1). This test case is performed to analyze the effects of topography independent of any geological discontinuities of the Earth with the exception of the topographic surface. For the 1D model, a flat Moho layer is fixed at 32 km depth. This model has a shear wave speed of 3180 m/s near the surface and 4500 m/s on the upper mantle as similarly used in *Tape et al.* (2009b). This model is examined to observe the effects of topography with structural variation within the crust. We applied the 1D wave-speed model for a flat surface by demolishing or "bulldozing" all features above zero elevation. Compared to another approach : pushing or pulling the wave-speed model from above and below zero elevation respectfully towards flat surface (*Aagaard et al.*, 2008), the bulldozing method preserves the wave-speed structure under the lowest surface elevation.

Table 2.1 compiled the framework of the homogeneous and 1D models.

2.2 Hexahedral meshing

Meshing is the most critical part of waveform modeling in the spectral element method. Several constraints need to be considered to produce a high quality mesh. These constraints include the number of grid points per shortest desired wavelength, the numerical stability, an acceptable distortion of the elements and the comparison between numerical cost and available computing resources. When these are not evaluated correctly, numerical problems may occur and lead to an increase in computational cost, lack of convergence of the simulation, or inaccurate results. These constraints are calculated as follows :

$$\Delta h = v_{\min}\, T_0 \tag{2.1}$$

$$\Delta t < C_{\max}\, \frac{v_{\min}}{v_{\max}}\, T_0 \tag{2.2}$$

$$s < 0.8 \tag{2.3}$$

Table 2.1: Density and velocities used for the homogeneous and 1D models.

Model	Density (kg/m^3)	V_P (m/s)	V_S (m/s)	Top (km)	Bottom (km)	Thickness (km)	Layer
Homogeneous	2800	6700	3870	0	400	400	1
1D	2400	5500	3180	0	3.5	3.5	1
	2670	6300	3640	3.5	14	10.5	2
	2800	6700	3870	14	32	18	3
	3000	7800	4500	32	400	368	4

where Δh is the grid spacing, v_{max} and v_{min} are the maximum and minimum seismic wave speeds in the element, T_0 is the shortest period that we seek to resolve, Δt is the time step, C_{max} is the maximum Courant number, which determines the stability of the simulations (the calculations are unstable above this value), and s is the equiangle skewness, which is related to the acceptable distortion of the elements for SEM (*Casarotti et al.*, 2008).

Our meshes for southern California are 672 km east-west, 504 km north-south, and extend to a depth of 400 km (Figure 2.1). Two types of meshes are considered, one with flat surface and another with topography. The topography data is obtained from ETOPO1 global relief published by the National Geophysical Data Center (NOAA) with a resolution of 1.8 km. ETOPO1 is a 1 arc-minute global relief model of Earth's surface that integrates land topography and ocean bathymetry (*Amante and Eakins*, 2009). We divide the mesh volume into a set of non-overlapping hexahedral elements (*Peter et al.*, 2011).

In creating the mesh, we subdivide the model volume into a set of non-overlapping hexahedral elements (*Peter et al.*, 2011). The size of the smallest element near the surface is 2.8 by 2.8 km with depth 3.5 km, and the largest element in the deeper part of the mesh is 8.4 by 8.4 km with 8.3 km depth. The larger element is created by increasing the size of the smaller element at 32 km depth. Densification of the mesh is needed near the free surface, in areas of slow wave speed or of steep topography (*Komatitsch and Tromp*, 1999). The total computation time for mesh creation is 38 minutes with a total of 657,600 elements. The mesh is designed to honor geological boundaries, such as free surface and Moho layer.

2.3 Seismic wavefield simulations

SEM solves the wave equation using piece wise Lagrange polynomials function that is calculated on the interpolation points or Gaus-Lobatto-Legendre number (NGLL). The choice of NGLL is related to the grid spacing (Eq. 2.1). Few number of grid points on each element exhibits the same inaccuracy as FEM. To satisfy the accuracy of SEM, we select NGLL5 (*Komatitsch and Tromp*, 1999;

Table 2.2: Summary of meshing and simulation parameters for one source.
The mesh is divided into 96 partitions so that the simulations can run on a cluster of parallel cores.
The mesh comprises 657,600 elements and a total of 43 million grid points.

Model	Homogeneous		1D	
Surface	Flat	Topography	Flat	Topography
mesh size	672 km × 504 km × 400 km			
time step	0.02 s			
unstable time step	0.03 s			
simulation time (hh:mm:ss)	00:41:26	00:41:33	00:42:21	00:42:29
seismogram time	200 s			
number of partitions	96			
total number of grid points	43,843,729			
total number of elements	657,600			
base number of elements	4800			
surface number of elements	14,400			
base element size	8.4 km × 8.4 km × 8.3 km			
surface element size	2.8 km × 2.8 km × 3.5 km			

Casarotti et al., 2008). When calculated with NGLL5, each element consists of 125 grid points.

We use the software SPECFEM3D (*Komatitsch et al.*, 2004; *Peter et al.*, 2011) to perform a series of earthquake simulations to generate a large database of synthetic seismograms. We assume a perfectly elastic Earth with no ocean water layer, free stress on the surface and absorbing boundary condition on the other edge boundaries. We use parallel implementations on large clusters by dividing the volume mesh into 96 partitions (Figure 2.1). This parallelization reduces computing time by distributing the memory over several computer cores. High resolution meshes and wavefield simulations are executed on the high-performance computing clusters at the Arctic Region Supercomputing Center, University of Alaska Fairbanks using 16-cores node. Each node that consists of 16 cores evaluates a simulation in one partition mesh. For each simulation, the whole volume has a total of 43.8 million grid points when calculated at NGLL5. The wave propagates for 200 s with the longest simulation time 42 minutes and 21 seconds. A summary of mesh generation and wave propagation simulation is shown in Table 2.2.

The numerical simulation source is described by origin time, 3 elements of hypocenter and 6 elements of moment tensor with a delta function. We select 137 real earthquakes (*Tape et al.*, 2009b) with magnitude ranging from M_w 3.4 to 5.4 (Figure 2.2). These real earthquakes produce synthetic waveform outputs that are closer to real data compared to a synthetic source. Explosion type of source is not selected because it does not produce Love waves, which may be of interest in the seismology world. The wave propagations are then recorded by 315 synthetic stations that are approximately 30 km apart from each other (Figure 2.3). These sets of source and stations produce

abundant synthetic seismogram outputs over the whole region of southern California. From these datasets, we can comprehensively analyze the effects of topography.

2.4 Shortest resolvable period quantification

The accuracy of a simulation output is confined to the frequency it is able to resolve. However, there has been no documentation from previous work to address this issue. The numerical accuracy tests performed in this study define the shortest resolvable period that needs to be applied to the synthetic waveforms. This test would assure that each synthetic waveform is resolved before continuing to the next step, the quantification of topography on the seismic wavefield.

One approach to improve the numerical accuracy is by utilizing a fine resolution mesh to produce synthetic waveforms. In the spectral element method, the wavefield is represented in terms of high degree Lagrange polynomials on Gauss-Lobatto-Legendre (GLL) interpolation points (*Komatitsch et al.*, 2004). Smaller NGLL corresponds to a coarser resolution mesh, which creates a wavefield with less accuracy. On the other hand, producing an accurate simulation using too many interpolation points extends computation time. In this study, we perform the shortest resolvable period test on the synthetic waveforms to ensure the waveforms' numerical accuracy. The resolved waveforms from this test are the ones used for the analysis of the effects of topography.

The test procedure progresses as follows : GLL interpolation points are utilized to produce a finer (NGLL7) and a coarser (NGLL5) resolution mesh (Figure 2.4). The simulation output pairs from a coarser and a finer resolution mesh are compared and filtered together with several period ranges (Figure 2.5). The misfit between each synthetic pair is calculated for a range of low-pass filters using two different equations

$$F(T) = \int [w_L(t,T) - w_H(t,T)]^2 \, dt \tag{2.4}$$

$$F(T) = \frac{\int [w_L(t,T) - w_H(t,T)]^2 \, dt}{\int [w_H(t,T)]^2 \, dt} \tag{2.5}$$

where $w_L(t,T)$ and $w_H(t,T)$ corresponds to displacement seismograms from the coarser and finer resolution meshes, respectively, filtered at periods $\geq$T s. Normalizing the waveform difference removes the magnitude effects so that higher magnitudes do not imply higher misfit. The period where the misfit difference is close to zero is the one which gives the most resolved output. We choose threshold values of

$$F_{\text{homo}} = 10^{-2.5} \tag{2.6}$$

$$F_{\text{1D}} = 10^{-1.5} \tag{2.7}$$

Table 2.3: Number of simulations performed in this study.
We produced one mesh for the flat homogeneous and 1D model (A), and similarly for topographic case (B). The number of grid points in flat homogenous model is the same with flat 1D model (also similarly with topographic case for both models). In order to estimate the shortest resolvable period of the coarser mesh simulations, we perform a set of simulations on a finer (NGLL7) mesh (Figure 2.4). We apply the shortest resolvable period estimated with-topography simulations to those without-topography simulations; this allows us to avoid calculating the fine mesh simulations for the no topography case.

Model	Mesh	Coarser mesh	Finer mesh
homogeneous	A	137	0
homogeneous with topography	B	137	137
1D	A	137	0
1D with topography	B	137	137

Table 2.4: Comparison between simulations using the finer and coarser meshes. In each case the finite element mesh is the same, but the discretization of grid points on the mesh changes (Figure 2.4).

Mesh	Coarser mesh		Finer mesh	
Model	Homogeneous	1D	Homogeneous	1D
Time step (s)	0.02		0.01	
Unstable time step (s)	0.03		0.02	
Simulation time (hh:mm:ss)	00:41:33	00:42:29	4:17:47	5:00:55
Total number of grid points	43,843,729		145,978,213	

for the homogeneous and 1D models, respectively (Figure 2.6). A summary of simulations with the coarser and finer resolution meshes is shown in Table 2.4.

We apply the shortest resolvable period that is estimated from the simulations with topography to those simulations with flat surface; this allows us to avoid calculating the fine mesh simulations for the flat surface case (Table 2.3). The shortest resolvable period test is conducted on simulations with topographic surface considering that the topography creates complex wave propagations (*Lee et al.*, 2008). This results in longer resolvable periods for the with-topography synthetic waveforms compared to the without-topography synthetic waveforms.

Calculating this misfit (Eq. 2.5) on the displacement traces will give a shorter resolvable period compared with velocity or acceleration traces. This is desirable because topographic effects can then be analyzed in the highest frequency possible. One drawback is that for very short source-station paths, there can be a (real) static offset in the seismograms that will result in a very large waveform difference. In this study our emphasis is on the shapes of the waveforms rather than

differences in the static offsets.

The shortest resolvable period quantification is computed for each component, source and station. For each path, the shortest resolvable period of the waveforms is compared between the three components: vertical (Z), radial (R), and transverse (T). We select the maximum shortest resolvable period over the three components and assign it as the shortest resolvable period for each component in the path. The result in Figure 2.7 suggests that, in general, the transverse components have the maximum shortest resolvable period for each path in a homogeneous model. This component consists of an S wave which travels at a slower wave speed. In the 1D model, this comparison is well distributed between the components, although the maximum of shortest resolvable period is the vertical component.

Simulations with the 1D model generally produce waveforms that need to be numerically resolved with longer resolvable periods compared to the homogeneous one. The waveforms that propagate in the 1D model experience complexities due to the surface topography and the slow wave-speed layer near the surface. The shortest resolvable period generally increases with distance for both homogenous and 1D models if one considers the minimum of all shortest resolvable periods for each distance (Figure 2.8).

Figure 2.9 is an example of shortest resolvable period that is calculated for one source (9734033) and 315 stations. For this strike slip source, the stations located in two (for the vertical and radial components) and in four (for the transverse component) nodal directions need to be resolved in a longer resolvable period. This figure demonstrates that the influence of source mechanism cannot be completely eliminated through the normalization in the equation. The variation on the shortest resolvable period for each station in a source demonstrates the importance of calculating the misfit for each path.

Figure 2.10 is an example of a path from source 9734033 to station NW008 in the homogenous model. It demonstrates the significance of applying the path specific shortest resolvable period as opposed to applying one minimum or maximum value over all stations in one source. Determining one shortest resolvable period for all stations in one source may lead to numerical dispersion or loss of high frequency detail in the waveforms depending on the choice of shortest resolvable period. We do not apply the maximum shortest resolvable period for all stations in a source because this value can vary up to 3 seconds in the homogeneous model and 10 seconds for the 1D model. In this long period range, the topography information is not present in the waveforms anymore.

The disadvantage of computing the shortest resolvable period in a normalized misfit is the tendency to be over conservative. Some problematic areas, such as some paths in the nodal directions, may end up resolved with a longer period. These paths could be resolved in a shorter period when

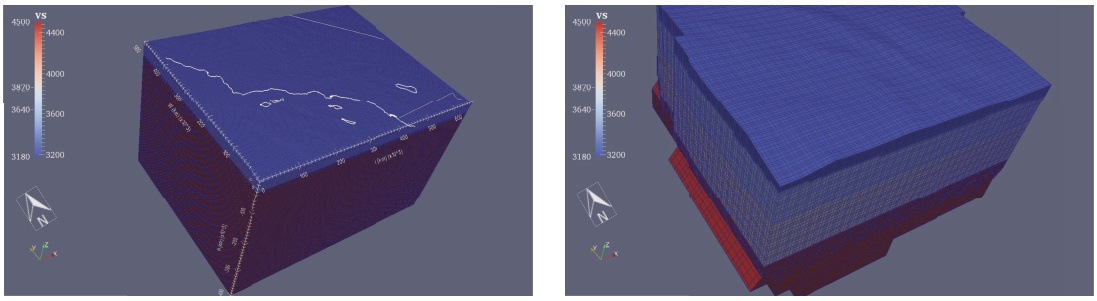

(a) southern California mesh (b) single partition of mesh

Figure 2.1: Southern California mesh for the 1D model.
(a) The complete southern California mesh. On the surface, the coast is plotted separately to display the region of southern California. The limits and boundaries of the 1D wave speed in the elements can be seen in figure (b). (b) One partition of the southern California mesh. Each partition is assigned to a set of cores in the cluster; this allows the memory for solving the wave equation to be distributed over many different cores. In this figure, the color scale represents the shear wave speed, and the lines corresponds to the mesh grid points.

we use the non-normalized misfit (Eq. 2.4). However, calculating the non-normalized misfit for this study is time-consuming because the threshold varies with source and model and therefore was not done.

Figure 2.11 illustrates the median of the shortest resolvable period for each source when plotted against increasing source depth. From left to right, the figure shows the median of the shortest resolvable period for the homogeneous and the 1D models. Shallow sources excite the wave propagation on the surface which is shown by the variation of the shortest resolvable period. These values change with wave-speed models, paths, or source mechanisms.

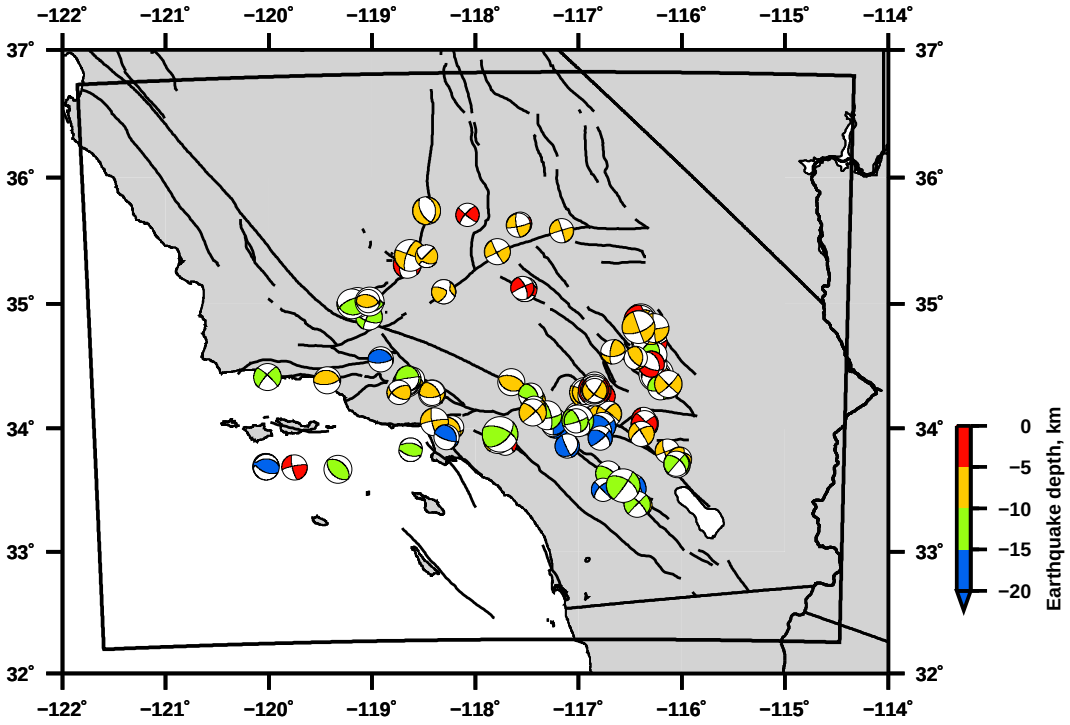

Figure 2.2: 137 earthquake sources used in this study.
The moment tensors are a subset of earthquakes used within the study of *Tape et al.* (2009a, 2010).

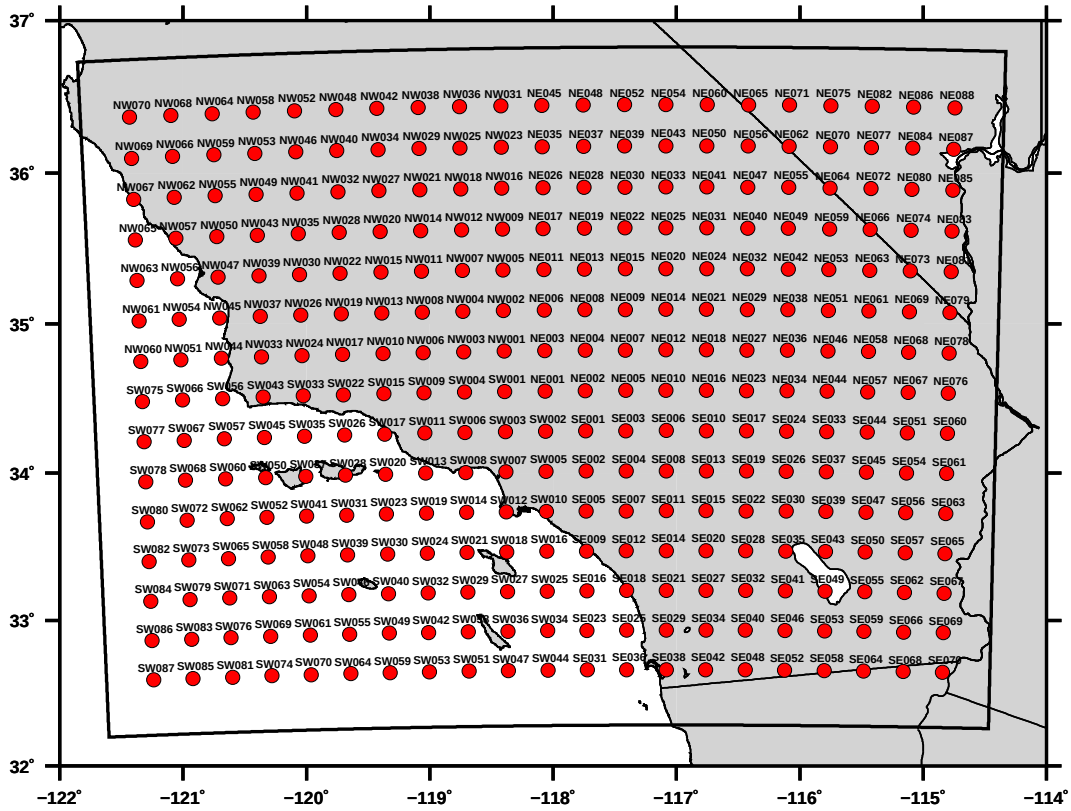

Figure 2.3: 315 synthetic stations used in this study.
We use a uniform grid of stations (on a UTM grid) in order to uniformly sample the seismic wavefield for each earthquake. The spacing between the stations is 30 km.

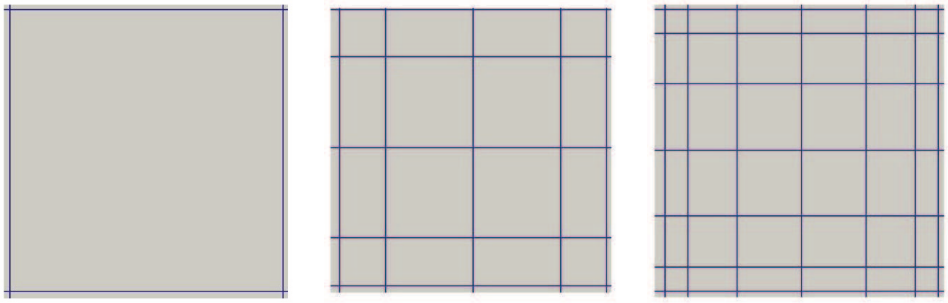

(a) Element (b) NGLL 5 (c) NGLL 7

Figure 2.4: Grid point discretizations for a single element.
(a) A single element within a finite-element mesh. (b) NGLL5 discretization for the coarser resolution mesh. There are 5×5 grid points on the surface of this element. (c) NGLL7 discretization for the finer resolution mesh. There are 7×7 grid points on the surface of this element.

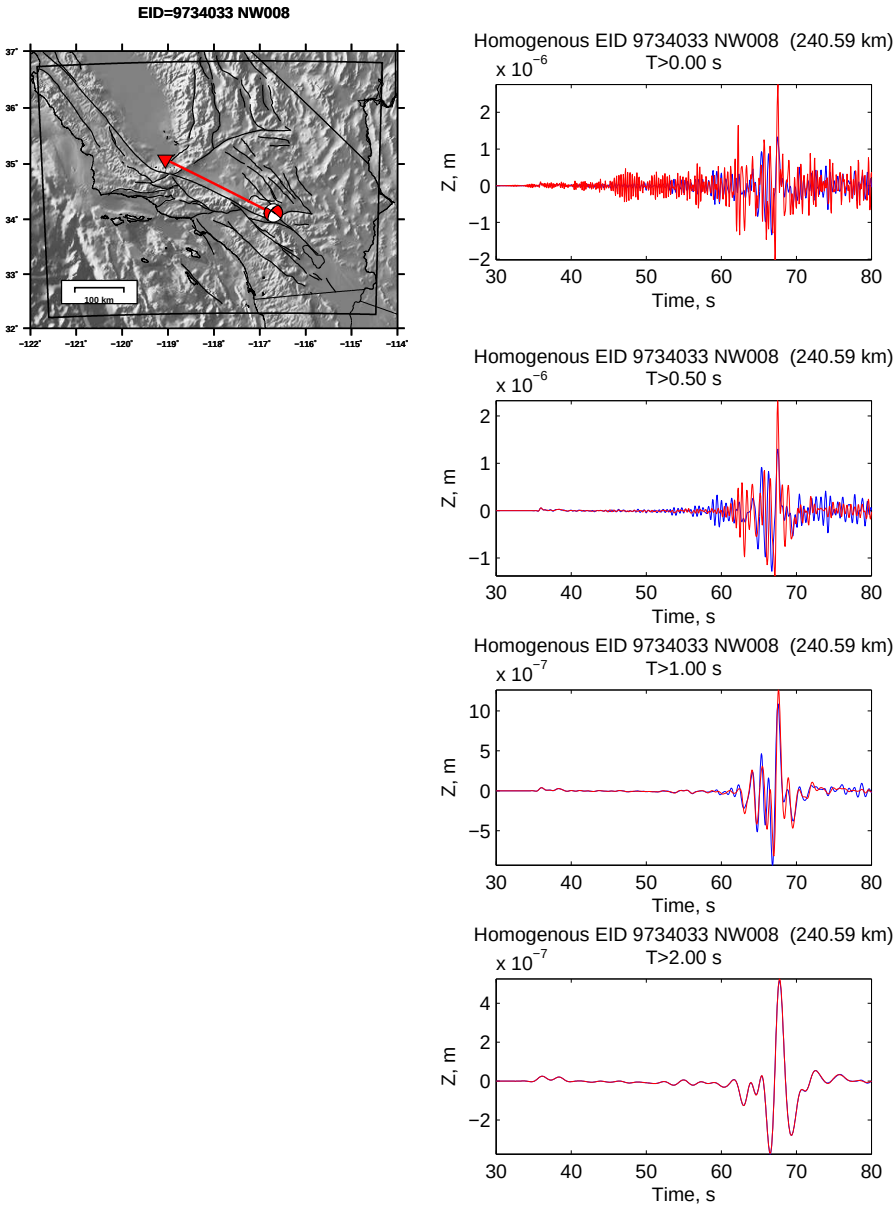

Figure 2.5: Synthetic seismograms filtered over different period ranges.
This is an example for a single time series that is unfiltered (top), and low-pass filtered with cut off periods of 0.5 s , 1.0 s, and 2.0 s. The red waveform is from the finer (NGLL7) resolution mesh; the blue waveform is from the coarser resolution mesh. The waveform pair from the same structural model and surface is filtered with increasing period until they are identical. Waveform from this particular path (source 9734033 to station NW008) in the homogeneous model is resolved when low-pass filtered with a corner of 2.00 s, as described in Figure 2.6.

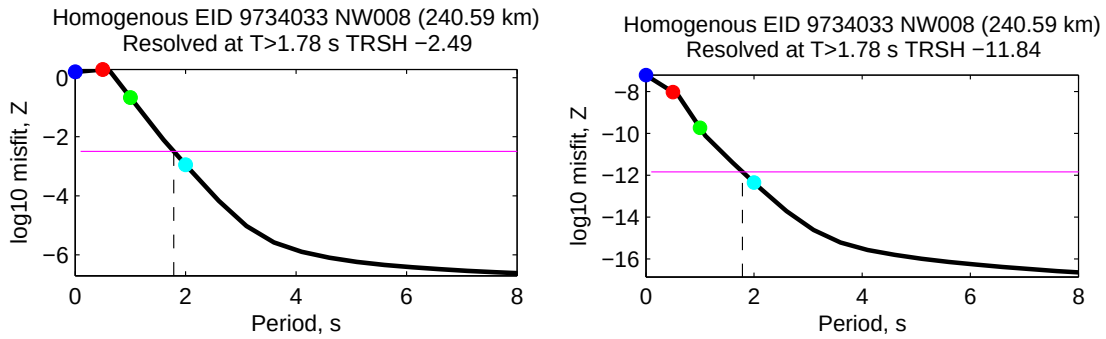

(a) Normalized (Eq. 2.5) (b) Unnormalized (Eq. 2.4)

Figure 2.6: Misfit as a function of period.
The misfit curve is calculated for a single seismogram from source 9734033 to station NW008; the misfit is the difference between the seismogram calculated using the coarser and finer meshes. The points refer to the different periods that were produced for unfiltered (blue), and low-pass filtered in Fig. 2.5: 0.5 s (red), 1 s (green), and 2 s (cyan). The magenta line shows the threshold where the shortest resolvable period is achieved using the misfit functions. The misfit decreases with increasing period. (a) Curve based on the normalized misfit function (Eq. 2.5). The threshold is fixed at $10^{-2.5}$ for all paths. (b) Curve based on the unnormalized misfit function (Eq. 2.4). The threshold must be changed depending on the particular seismogram (i.e., path); here it is set as 10^{-12}.

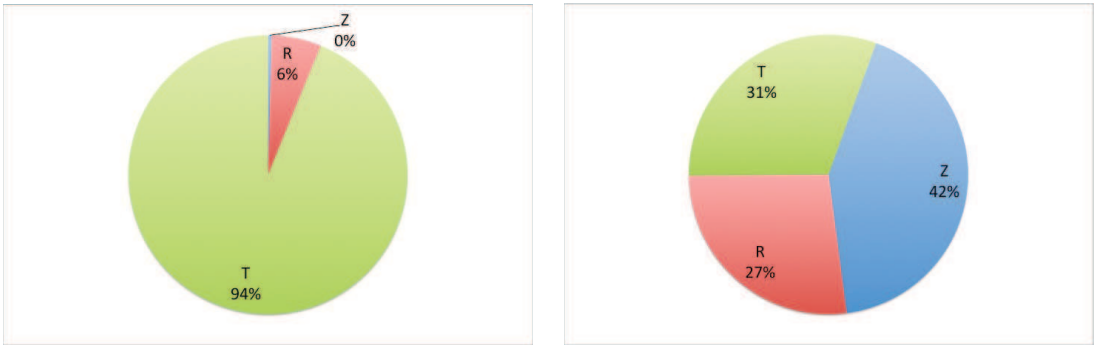

(a) Homogeneous (b) 1D

Figure 2.7: Component with maximum shortest resolvable period calculated for each path.
For each path we calculate the shortest resolvable period for each component (Z, R, T) for two models with topography (homogeneous, 1D). For the homogeneous model, the maximum shortest resolvable period is dominantly on the transverse component, implying that it is more difficult to resolve S waves than Rayleigh waves; however, this could be related to the normalization used in our misfit (Eq. 2.5). (Note that the S waves travel faster than Rayleigh waves and do not interact as much with the surface topography.) For the 1D model, the maximum shortest resolvable period is shared similarly among all components.

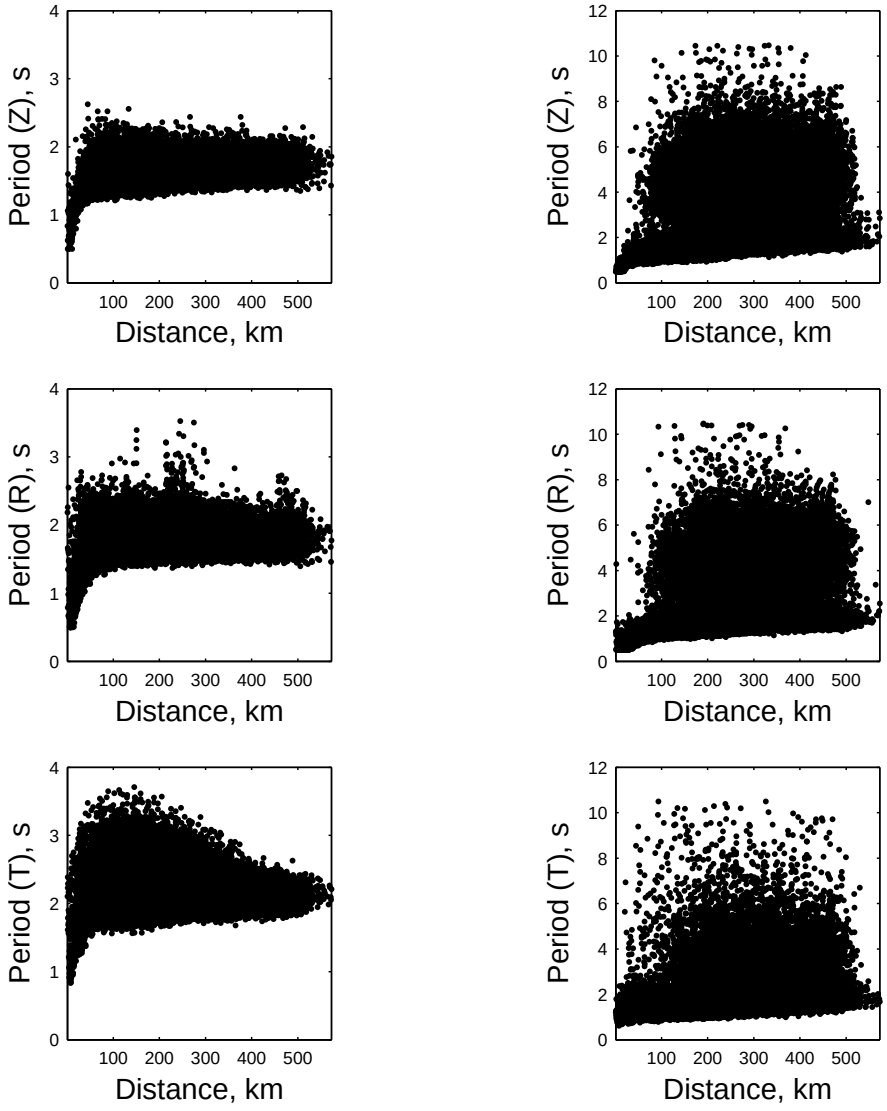

(a) Homogeneous (b) 1D

Figure 2.8: Shortest resolvable period as a function of distance.
The comparison is made for all 43,155 paths (each with a source-station distance) for the vertical (top), radial (middle), and transverse (bottom) components. In general, the shortest resolvable period increases with distance, if one considers the minimum of all shortest resolvable periods for each distance. Note the difference in y-axis limits for the homogeneous (a) and 1D (b) results.

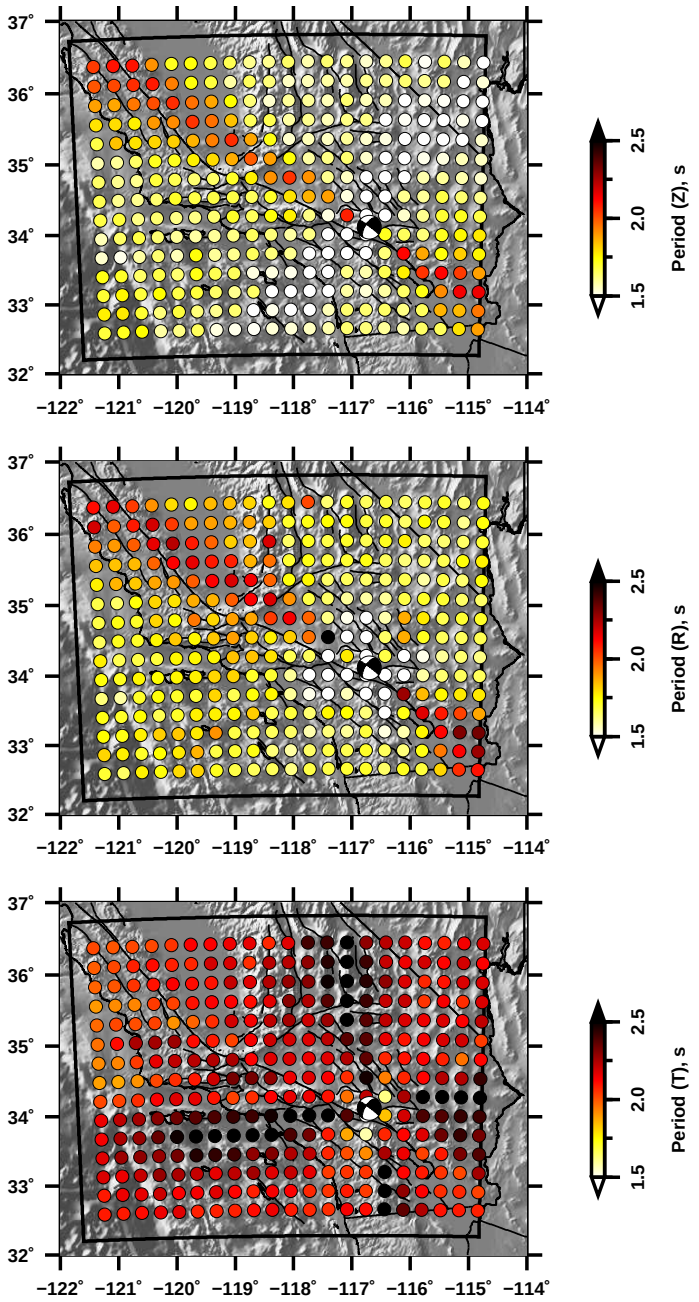

Figure 2.9: Shortest resolvable period for source 9734033.
Spatial variation in the shortest resolvable period for each station for the vertical (top), radial (middle), and transverse (bottom) components. A longer period is needed to resolve stations that are in some nodal directions for this strike-slip mechanism. Additional analyses on a path with this source are shown in Figures 2.5, 2.6, and 2.10.

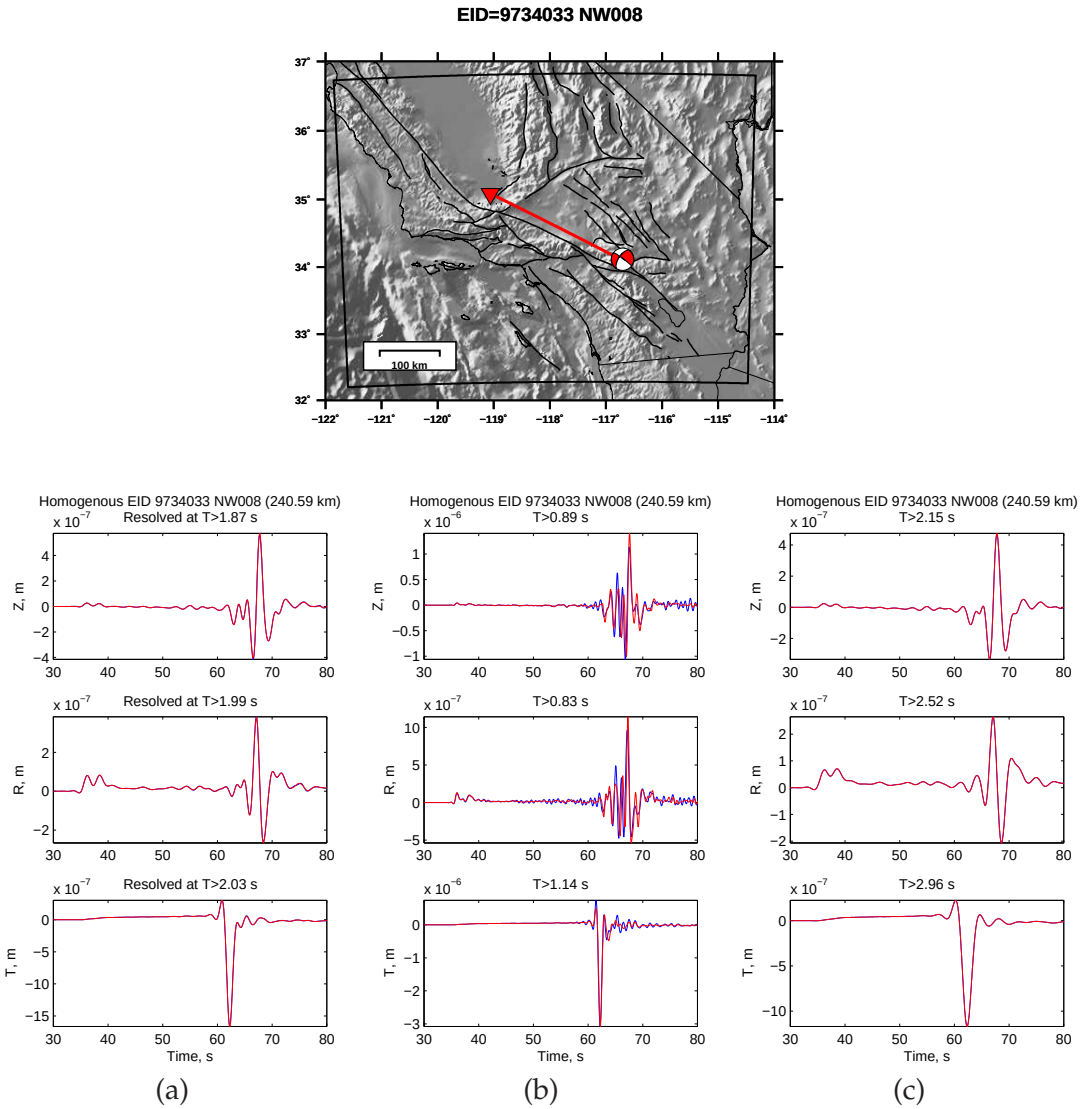

Figure 2.10: Choice of period to use in quantifying the topographic effects.
Here we show a single path—event 9734033 to station NW008—for the vertical (top), radial (middle), and transverse (bottom) components. (a) Seismograms filtered using the shortest resolvable period for this path (Z = 1.87 s, R = 1.99 s, T = 2.03 s). (b) Seismograms filtered using the minimum of the shortest resolvable period for all stations for this source (Z = 0.89 s, R = 0.83 s, T = 1.14 s). As expected, the waveforms are unresolved, since the period is below the path-specific shortest resolvable period. (c) Seismograms filtered using the maximum of the shortest resolvable period for all stations for this source (Z = 2.15 s, R = 2.52 s, T = 2.96 s). As expected, the waveform is resolved but lacks some of the details that are visible at shorter periods (a).

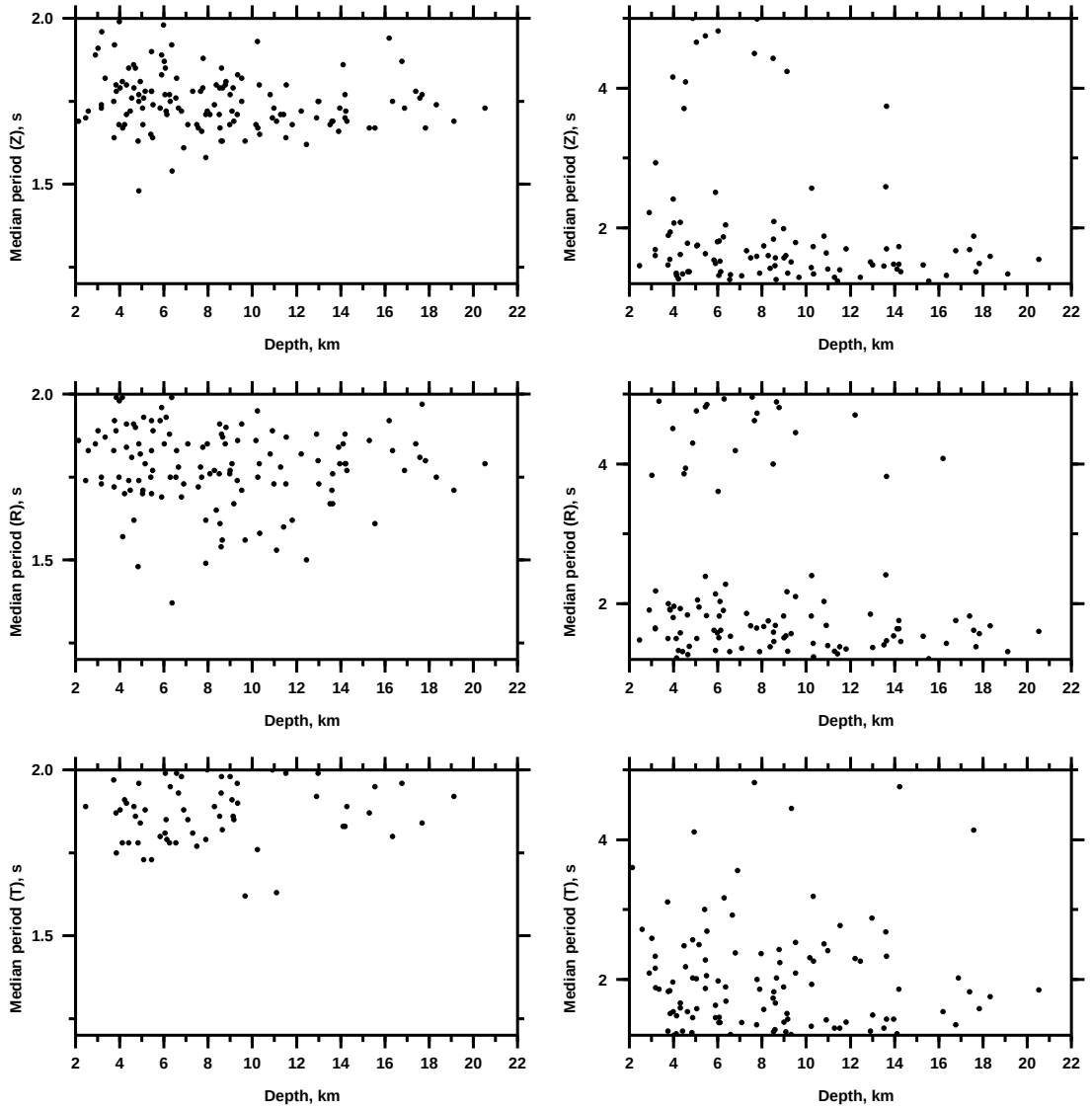

(a) Homogeneous (b) 1D

Figure 2.11: Shortest resolvable period as a function of source depth.
The median of the shortest resolvable period for all stations for each source is plotted for the vertical (top), radial (middle), and transverse (bottom) components. No clear trend is visible between source depth and shortest resolvable period .

Chapter 3

Quantification of the effects of topography

We perform 822 simulations (137×6; Table 2.3), which provides a large set of synthetic seismograms. For each of the 137 sources (Figure 2.2), we save synthetic seismograms at 315 stations (Figure 2.3) on three components (vertical, radial, and transverse). Taken together, there are 43,155 paths and 129,465 seismograms. We have six sets of these seismograms for each case listed in Table 2.3. In this chapter we will describe and analyze this large volume of synthetic seismograms—and corresponding topographic effects—in a variety of different ways. A summary of our analysis is provided in Chapter 4.

We quantify the effects of topography using the same function as used for establishing the shortest resolvable period (Eq. 2.5). The only difference is that instead of comparing seismograms computed using the same model with two different meshes (finer resolution and coarser resolution), here we compare seismograms computed using a model with topography and a model without topography. The denominator in Equation (2.5) is the time series from the topographic model, rather than from the finer resolution mesh ($w_H(t)$). One modification is that for the topographic effects we calculate the waveform difference only up to the point of the time series that represents 90% of the cumulative energy. This is done to avoid incorporating some of the waveforms late in the seismograms that result from spurious reflections off of boundaries.

We start with a comprehensive example for one source–station pair: event 14118096 to station NW029 in the San Joaquin valley. The process begins with six simulations for this event (Table 2.3), two of which are shown in Figure 3.1. The simulation has the advantage of dense spatial and temporal sampling of the wavefield, and the snapshots provide details that are not always easy to identify from seismogram comparisons. In Figure 3.1 we see the influence of topographic scattering, especially on the nodal direction for Rayleigh waves, where there are minimal amplitudes in the flat model but visible amplitudes in the topography model.

Wavefield snapshots and seismograms are two subsets of the seismic wavefield. The snapshot is fixed time and complete coverage of space, whereas the seismogram is fixed space and complete coverage of time. Most of our analyses are based on synthetic seismograms, in part because we want to mimic a study with real seismograms, which are only available at discrete points in space.

Figure 3.2 shows the synthetic seismograms for source 14118096 at station NW029 in the San Joaquin valley. Clearly there are significant differences between the flat-surface and topographic-surface cases for both the homogeneous model and the 1D model.

This waveform comparison highlights the change of the waveform due to the effects of topography. The topographic effects are relatively small. It includes changes in amplitude, such as amplification or scattering, post surface wave coda, and changes in phase due to the structure in

the 1D model. The topography has more dramatic effects on the propagation of surface waves than that of body waves as stated by previous work (*Ma et al.*, 2007). The amplitude spectra for this path can be observed in Figure 3.3.

3.1 The topographic effects as generalized from the complete dataset

The topographic effects as a function of period depend on the choice of misfit function and are only meaningful for periods for which the waveforms are accurate. Using Equation (2.5), we calculated the quantification of topography for all paths for all components. For each component and for each period, we take the median value; these are used to make the three curves in Figure 3.4. The topographic effect decays with increasing period. This is as expected because the wavefield at longer periods is less sensitive to topographic variations.

The topographic effects increase with distance, except for the transverse components in the homogeneous case (Figure 3.5). This shows that, in general, surface wave complexity increases with distance, likely because more topographic effects are accumulated along a longer path. The transverse component of the homogeneous model does not produce Love waves. Hence there are no topographic effects on the surface waves. The S waves that are generated are not sensitive to the topographic effects because they do not interact much with the surface.

To compare the quantification of topography among the three components (Z, R, T), the maximum shortest resolvable period among the three components for each path is chosen. This value is then used to compute the topographic effects to assure the one-to-one comparison between each component. The result (Figure 3.6) shows that the vertical and radial components experience somewhat stronger topographic effects compared to the transverse component. In the 1D model, the Rayleigh waves are more sensitive to the topography than are Love waves; this supports initial studies by *Geli et al.* (1988) and *Bard* (1982). *Bard* (1982) stated that large and complex amplitudes are produced for Rayleigh waves.

3.2 The topographic effects between the homogeneous and 1D models

The direct waveform difference that we use (Eq. 2.5) encapsulates differences in amplitudes and in phase. Phase differences between waveforms (topo vs flat) are almost negligible in the homogenous model compared to the 1D model. As shown in Figure 3.2, the topographic effects, notably the phase differences, are much more pronounced in the 1D model, whose uppermost wave-speed layer has variable thickness due to the topography. The waves propagating from a high elevation region arrive late (compared to the flat case) due to the added slow wave-speed layer in the crustal structure, which results in a longer travel time (and also a slightly longer path). The reverse happens for waves traveling from a low-elevation region to a high-elevation region.

It may be helpful to consider an extreme comparison between our flat surface model and a "topography model" that is a high, flat plateau. In that case, we would see a phase difference between the "flat" waveforms and the "topo" waveforms, with the topo waveforms arriving later on account of the thicker slow layer. There would be essentially zero difference for the homogeneous case. (The great-circle path would be slightly longer.) And in neither case would there be any scattering due to topography.

3.3 Source-specific analysis of the topographic effects

As a general assessment, we compare the strongest topographic effects among all sources. For each source, we approach the analysis by selecting one value over all stations to represent the largest misfit value. This one value is derived from calculating 90% of the cumulative sum of the quantification of topography misfit over all 315 stations. We do not select the maximum value in order to dispose of any anomalies due to outliers. We also do not utilize a standard deviation or an outlier test because our distribution of topographic effects over 315 stations does not follow a Gaussian distribution (Figure 3.7).

For this calculation, we remove the paths that are less than 50 km from the data set. This prevents large differences due to the static offsets between the two sets of synthetics. Figure 3.8 shows that there are some patterns that are visible on a $\sim$50-km length scale. However, there are also adjacent sources with strong differences of topographic effects, implying that source depth or source mechanism are also responsible.

More detailed information can be obtained by source maps. A source map represents the quantification of topography from all stations and one source. Several source maps are here presented to demonstrate the quantification of topography on different sources (Figures 3.9–3.19). These maps reveal systematic patterns. Some prominent areas where the topographic effects are noticeable are oceanward of the continental shelf and the Sierra Nevada for the 1D model. In this model, different phases occur more significantly between the paired waveforms due to the different path lengths between the flat and topographic surfaces through a slow layer. This demonstrates how the topographic effects are accumulated in the two features. However, the source maps are also dominated by the source effect.

The strongest topographic effects are due to nodal paths for strike-slip mechanisms (e.g Figure 3.12). When we quantify the effects of topography by calculating the quantification of topography using the maximum of the shortest resolvable period for all stations for this source, the strongest topography effects remain present in the nodal paths for the homogenous model. The maximum of the shortest resolvable period for all stations for this source in the homogenous model is 2.17 s (Z), 2.93 s (R), 2.82 s (T). However, the topographic effects in the 1D model are less

visible in the nodal directions (Figure 3.13). This is due to the value of the maximum of the shortest resolvable period in the 1D model (Z: 10.45 s, R: 8.05 s, T: 5.46 s). Note that the topography information in the waveforms is generally present in the higher frequency range. Therefore, when we consider the maximum of the shortest resolvable period for the 1D model, the topography information in the waveforms is not present anymore.

Some interesting results from these station maps are described as follows.

1. Figure 3.9 is an example where this particular source results in weak topographic effects in all components of the homogeneous model.

2. Figure 3.10 is an example that demonstrates the topographic effects in the nodal directions for a reverse fault mechanism.

3. Figure 3.18 is a strike slip mechanism source that produces topographic effects in the nodal directions, and also other areas, such as the San Joaquin valley and the east of the Sierra Nevada for both models.

These examples show that even though the topographic effects are typically observed in the nodal directions, they are not always equally distributed in all directions. This implies that aside from the source mechanism, the surface topography also influences the wave propagation (More examples are shown in : Figures 3.11, 3.16, 3.19).

3.4 Station-specific analysis of the topographic effects

For each station, 90% of the cumulative sum of the quantification of topography misfit over all 137 sources is calculated by removing paths that are less than 50 km due to static offset differences, similarly defined in the previous subchapter. This produces a map with individual stations representing the topographic effects from all sources (Figure 3.20). This map shows large systematic differences due to topography on the oceanward side of the continental shelf and weak topographic effects in the Mojave for the 1D model. Note that this is likely due to phase difference. For the homogeneous model, there are moderate topographic effects in the San Joaquin valley, which can also be described in station maps. The features that produce strong topographic effects are in the area where there is a large vertical contrast in the topography (Figure 1.2) confirming previous studies by *Rodgers et al.* (2010) and *Köhler et al.* (2012).

However, this map also demonstrates some non systematic differences for the topographic effects. For example, SE030 exhibits anomalous amplitude in this map in all components and models. This is caused by one path from source 9734033 to the station without a systematic trend (Figure 3.21). This illustrates that source effects can still be imprinted in the station maps.

The station maps (all sources for one station) reveal large-scale systematic differences indicating that effects due to sources are averaged out. This would be this study's best attempt to eliminate the source effect. These maps help isolate where in southern California the topographic effects are accrued. Several examples are presented here to observe the topographic effects for station specific cases. Some of the results are as follows:

1. The effects of topography in the San Joaquin valley and the area surrounding it are strongest from the path propagating from the eastern part of the Sierra Nevada and from the San Bernardino mountains (Figures 3.22–3.25, 3.30). This can be observed in both the homogeneous and 1D models. These maps show a possible accumulation of topographic effects along the path from the station towards the mountainous areas.

2. In the homogeneous model of Figure 3.26, a certain topographic effect to the east of the Sierra Nevada can produce a large misfit difference at short distances. Unlike the general relationship between distance and topographic effects, this station shows that with increasing distance, the topography does not necessarily produce a stronger influence (Figure 3.27). The vertical component of SE046 in the homogeneous model (Figure 3.28) also illustrates that there is a strong topographic effect along the San Andreas fault starting at a short distance. This effect decreases as the path reaches the Mojave desert, which is a longer distance.

3. Significant strong topographic effects in the 1D model due to the phase differences can be identified from Figure 3.29. These effects are strongest on the waveform paths propagating from the sources located on the eastern area of the San Bernardino mountains to station SW062. The effects decay shortly afterwards.

4. In the transverse component of the homogeneous model (Figure 3.29), a hot spot indicating strong topographic effects on the S wave propagation is noticeable. The Rayleigh waves that propagate to the nearby topography might have been scattered and experience changes in direction. This is captured in this component.

3.5 Path-specific analysis of the topographic effects

In Figure 3.2 we showed an example of the topographic effects for a single path. This provides the most direct evidence of the topographic effects, since any differences in the seismograms can be attributed to topography. We provide a series of additional time series examples in Figures 3.35–3.40. For all example paths in the homogeneous and 1D models, the post surface wave coda can be detected.

Some paths are investigated to observe accumulations of the topographic effects.

1. Paths for 14118096 directing northwest and southwest. Towards the northwest direction, Figure 3.31 shows accrued topographic effects as the path distance increases towards the San Joaquin valley. The figure refers to waveform comparison of a homogeneous model in the vertical (Z), radial (R), and transverse (T) components. Topography reduces the amplitude of the surface waves and creates the post surface wave coda. The effects in the transverse component are not noticeable because the S wave does not interact significantly with the surface. Figure 3.32 shows accrued topographic effects with the same path in the 1D model. Topography affects the waveforms by creating amplitude complexity and phase difference, especially in the vertical and radial components.

   In the southwest direction, Figure 3.33 shows accrued topographic effects as the path distance increases towards the oceanward side of the continental shelf in the homogeneous model. Topography creates an insignificant impact on the waveform. Figure 3.34 shows accrued topographic effects with the same path in the 1D model. The topographic effects are more noticeable in the 1D model compared to the homogeneous model. This demonstrates that the addition of a slow layer affects the propagation of waveforms in this path.

2. Paths for 9700049 directing northwest. Towards the northwest direction, Figure 3.38 shows accrued topographic effect as the path distance increases towards the Sierra Nevada. Topography effects are seen in the transverse component. The Rayleigh waves encounter changes of direction as they propagate through a topographic surface. This effect is captured in the transverse component of the homogenous model, increasing with distance. Figure 3.39 shows accrued topographic effects with the same path in the 1D model. Topography effects are seen in the transverse component as well.

3.6 Topographic effects with increasing source depth

Shallower sources have a larger maximum single-station effect and a larger spread for both 1D and homogeneous models for all components (Figure 3.41). These sources can excite the surface wave more than the deeper ones. According to these figures (Figures 3.41 and 3.42), the general relationship between the source depth and the topographic effects is inconclusive. Further simulations are required to test how topographic effects change when source depth from a source is perturbed.

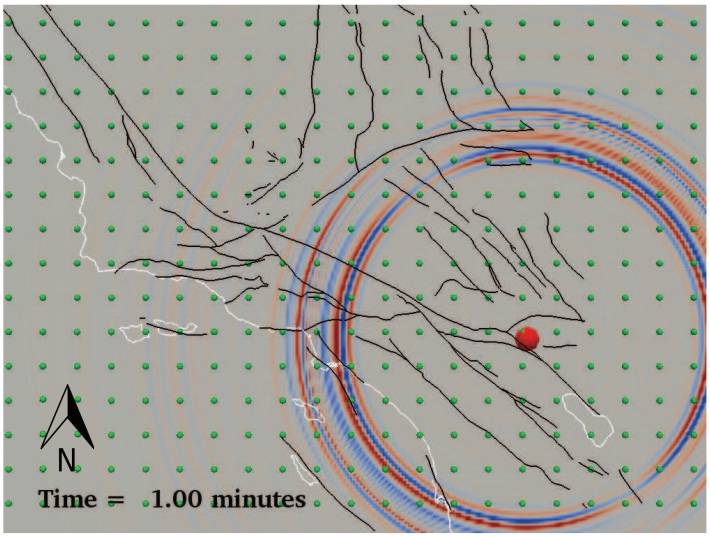

(a) flat (without topography)

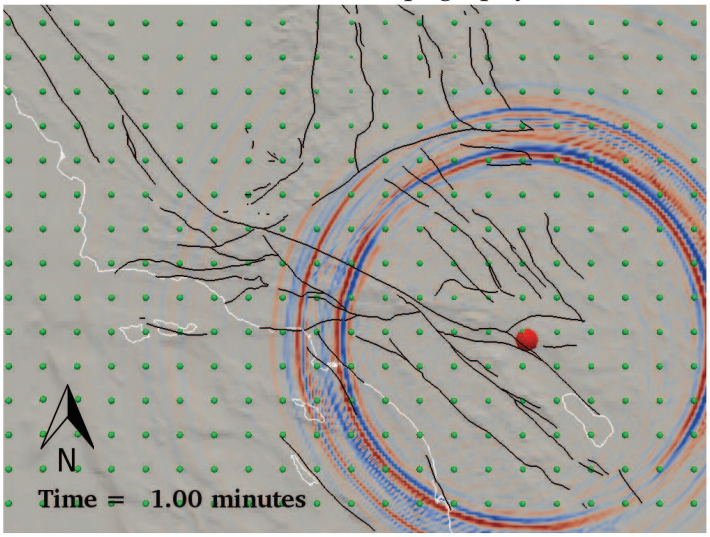

(b) with topography

Figure 3.1: Snapshots of the seismic wavefield with and without topography.
A 1D model is used in this simulation. Here the snapshot is the vertical component of the velocity field at time 1.00 minutes after the earthquake (event 14118096, see focal mechanism in Figure 3.2). The simulation is conducted with the periods longer than 2 s, which we know to be resolved throughout the model. The topography produces some scattering and increase in amplitude, especially in the northwest nodal direction.

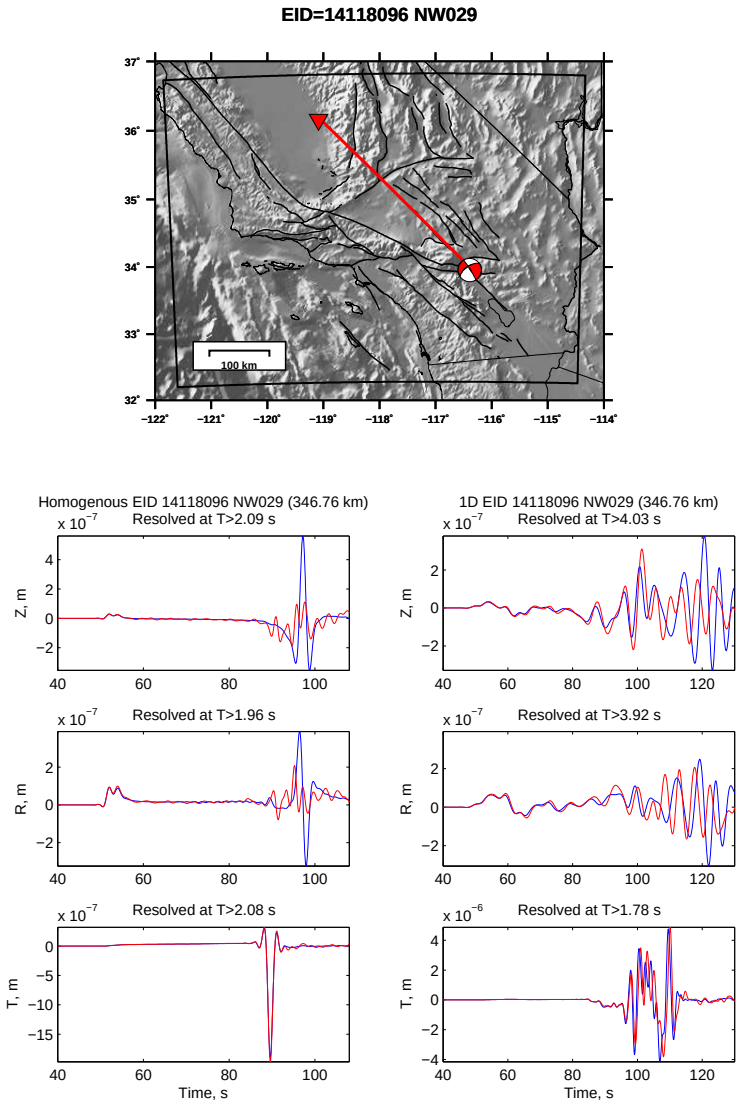

(a) Homogeneous (b) 1D

Figure 3.2: Topographic effects for path 14118096 to NW029.
The effect is shown for the vertical (top), radial (middle), and transverse (bottom) components. The blue and red waveforms are produced by meshes whose surface is flat or with topography, respectively. This figure shows a relatively long path propagating from event 14118096 towards the San Joaquin valley. (a) In the homogeneous model, the (nodal) Rayleigh wave on the vertical and radial components is strongly affected by the topography. (b) In the 1D model, the (non-nodal) Love wave (transverse component) in the model with topography arrives arrives later on account of the thicker slow wave-speed layer. The effects on the (nodal) Rayleigh wave (vertical and radial components) probably arise from multi-pathing, i.e., the Rayleigh wave finds a shorter travel-time path "through" the topography and arrives before the Rayleigh wave in the flat model.

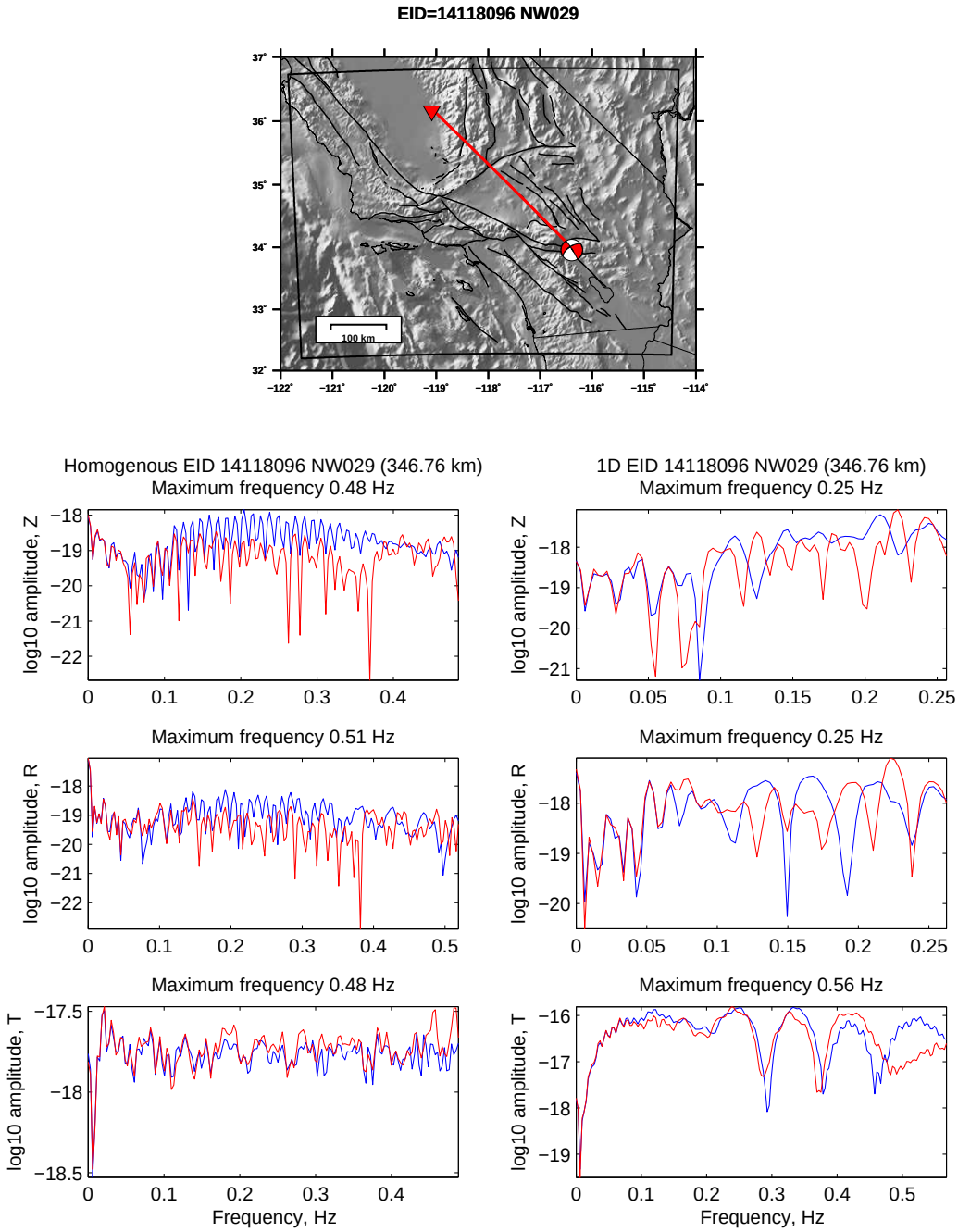

(a) Homogeneous (b) 1D

Figure 3.3: Amplitude spectra for path 14118096 to NW029.
Same as Figure 3.2, but shown here for the amplitude spectra in the frequency domain. In this representation, it is possible to isolate the amplitude differences to narrow frequency bands. However, phase differences between the seismograms are not represented here.

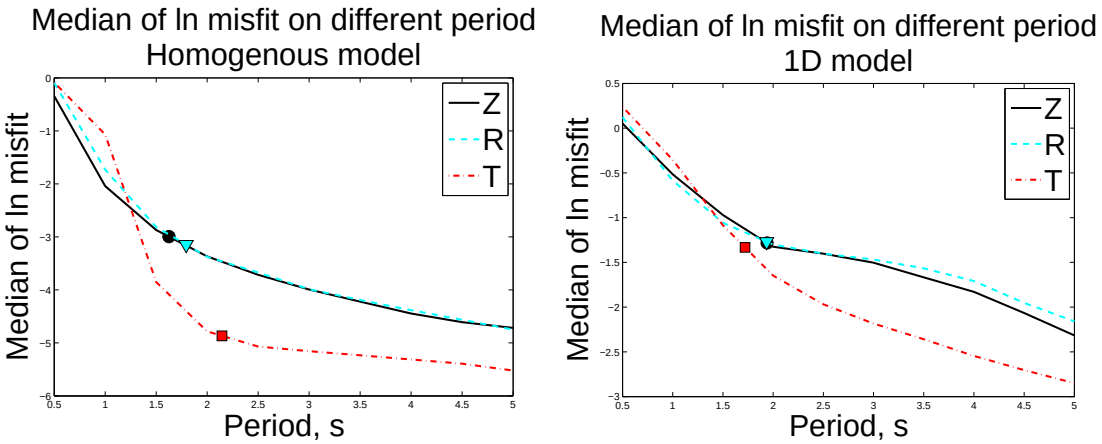

(a) Homogeneous (b) 1D

Figure 3.4: Topographic effects as a function of period.
The period represents the low-pass filter that is applied to the seismograms. The topographic effects are plotted as the median value of all 43,155 paths; it decreases with increasing period. Each symbol is the median of shortest resolvable periods for all paths for one component.

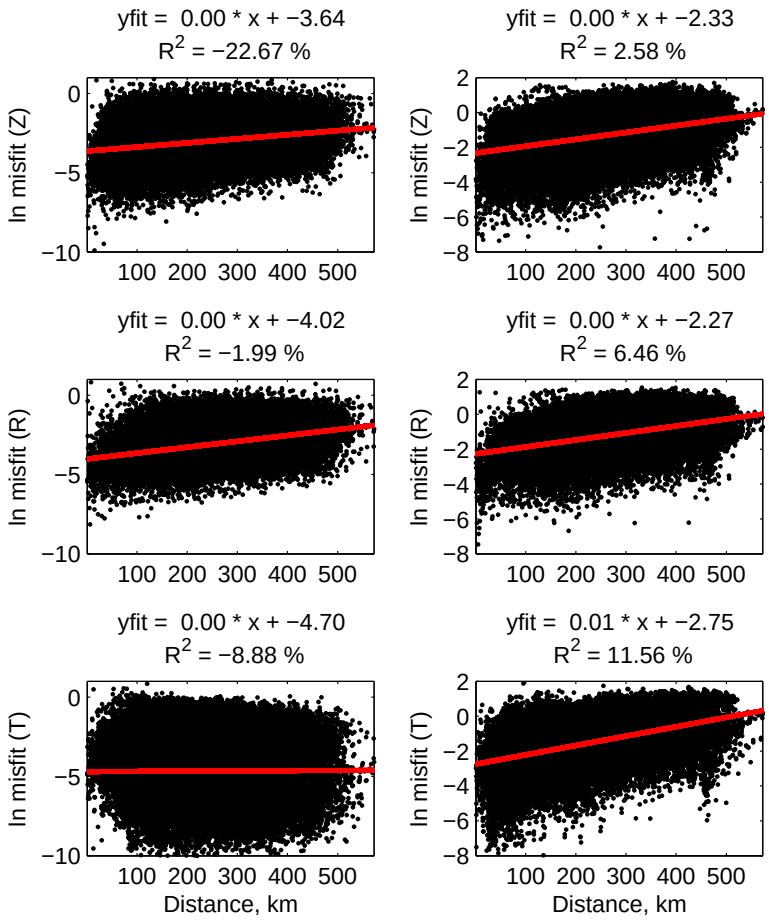

(a) Homogeneous (b) 1D

Figure 3.5: Topographic effects with increasing distance.
The topographic effects increase with distance for all components and for both models, with the exception of the transverse component in the homogeneous model. The homogeneous model does not produce any Love waves for the transverse component; the S waves recorded on this component do not interact much with the surface.

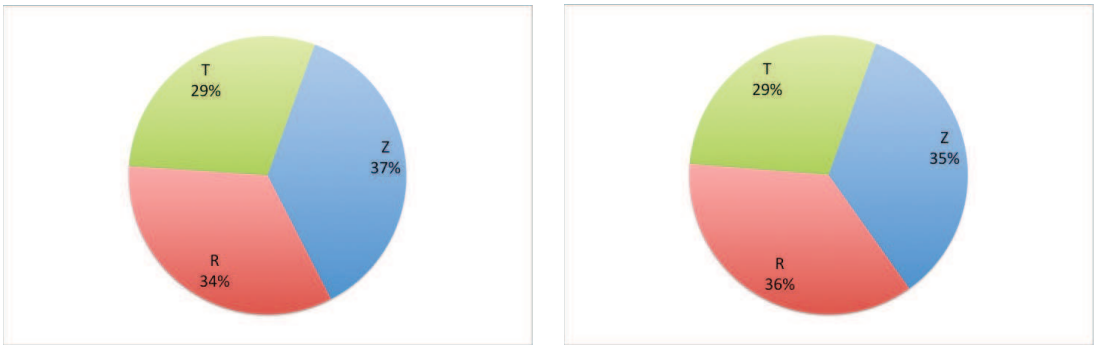

(a) Homogeneous (b) 1D

Figure 3.6: Component with highest topographic effects calculated for each path.
The quantification of topography is calculated on the maximum of the shortest resolvable period among the three components for each path. Results from the homogneous and 1D models suggest that the topographic effects are slightly stronger on the vertical and radial components.

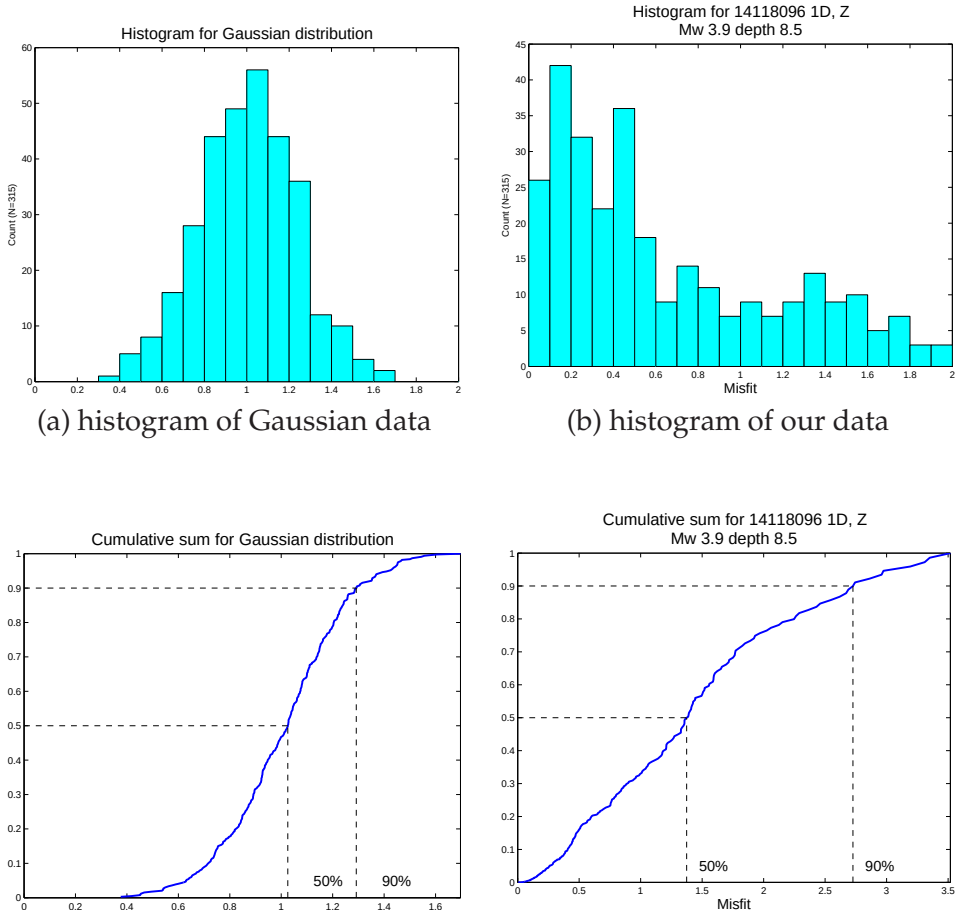

(a) histogram of Gaussian data (b) histogram of our data

(c) cumulative sum of Gaussian data (d) cumulative sum of our data

Figure 3.7: Example of extracting a single number to characterize a distribution.
(a) Gaussian random distribution generated using 315 data points, with 0.25 as the standard deviation value and 1.0 as the mean value. (b) Distribution of topographic effects for all stations from source 14118096 M_w 3.9 depth 8.5 km. Our distributions are generally not Gaussian. (c) Illustration of the cumulative sum based on the same points in (a). The dashed lines correspond to the points where 50% and 90% cumulative sums are achieved. (d) Cumulative sum for the distribution in (b). In order to quantify the topographic effects from some particular distribution (like in (b)), we must choose a value between 0 and 1.0 (100%). We want to pick a value that captures many of the extreme values but that excludes the most extreme values, which could be artifacts. Therefore we pick the 90% cumulative sum of the misfit over all stations for each source.

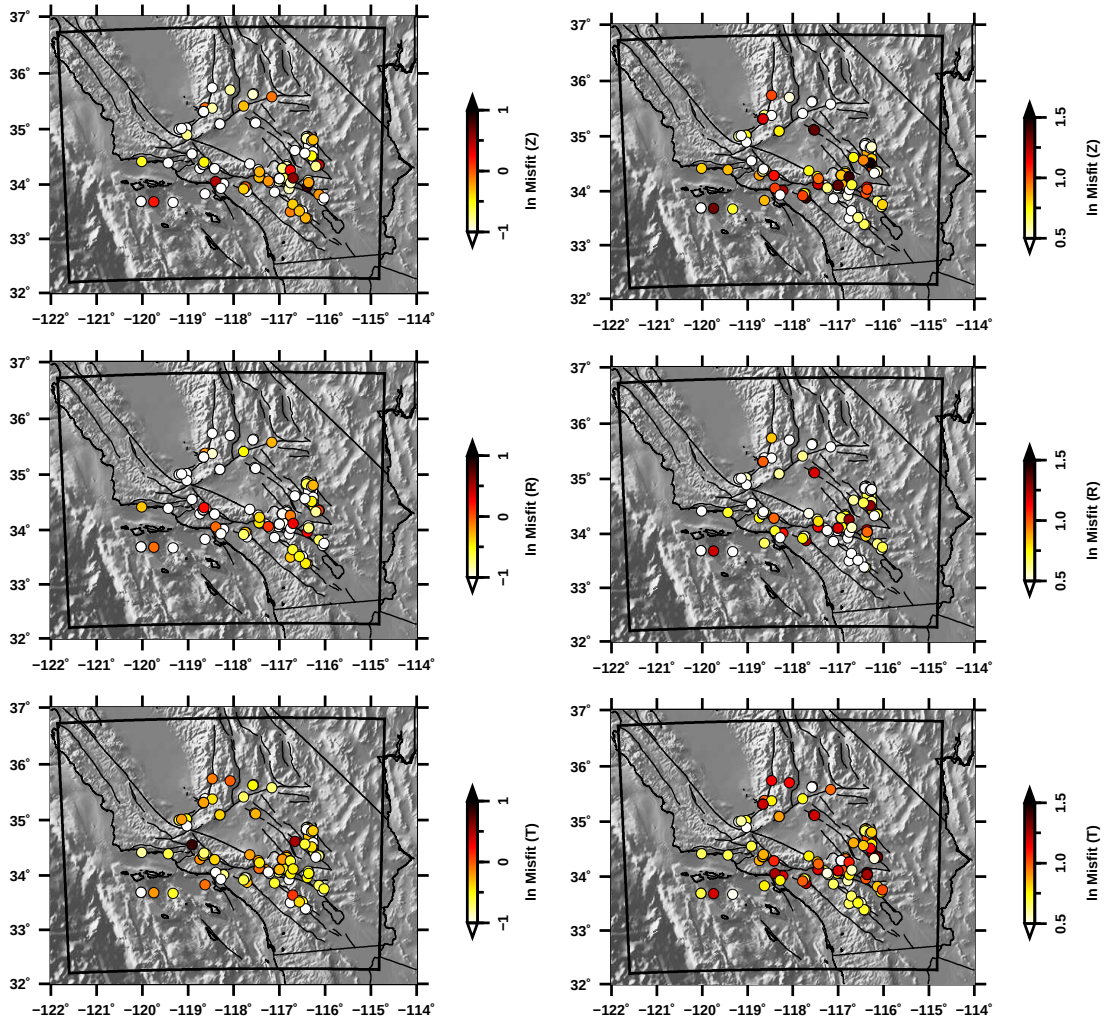

(a) Homogeneous (b) 1D

Figure 3.8: Cumulative topographic effects for each source.
For each source, the color represents 90% of the cumulative sum (e.g., Figure 3.7) of the quantification of the topography misfit over all 315 stations. There are some patterns that are visible on length scales of ∼50 km. There are also adjacent sources with strong differences, implying that effects besides the source epicenter are responsible for the topographic effects.

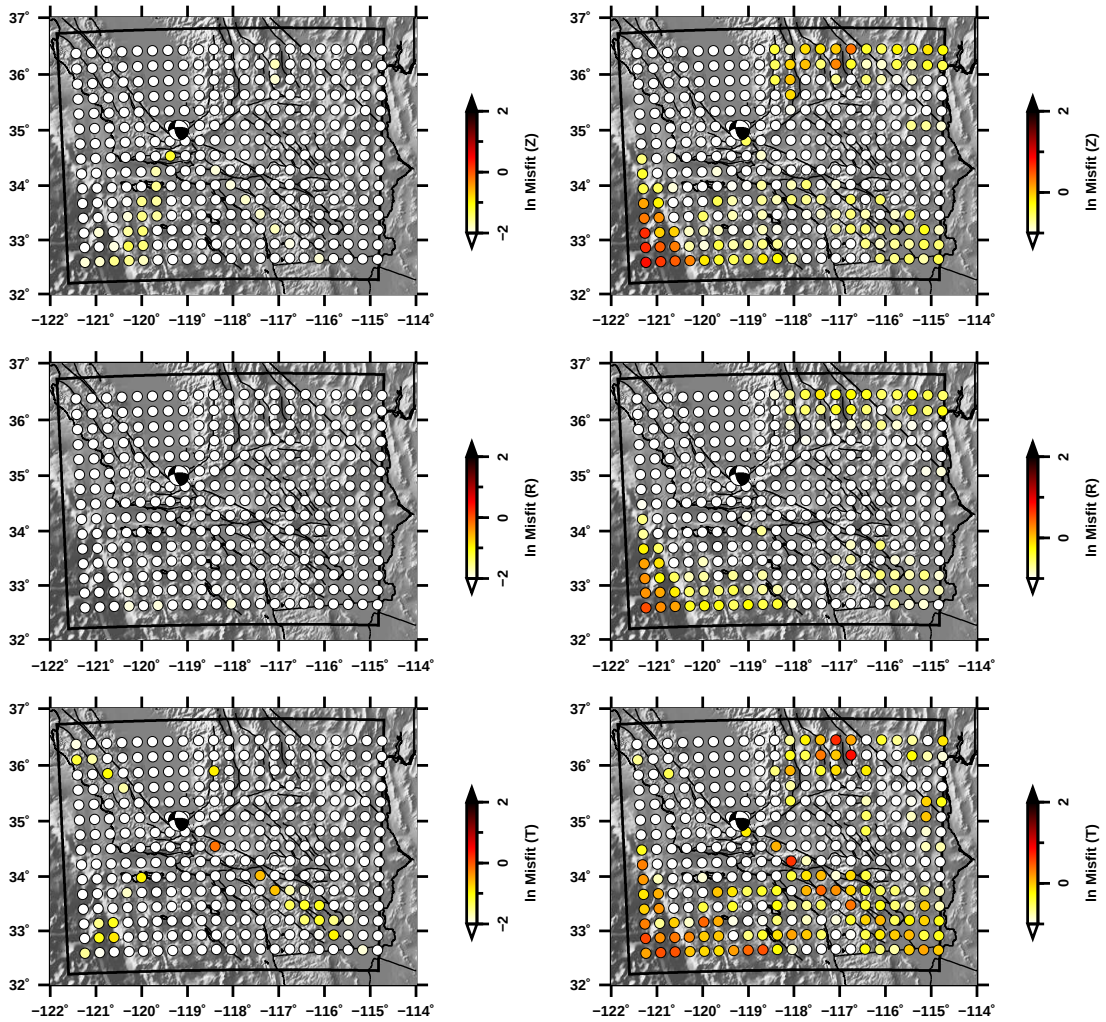

(a) Homogeneous (b) 1D

Figure 3.9: Topographic effects for source 10097009.
Topographic effects for source 10097009 (M_{w} 4, depth 13 km) for the vertical (top), radial (middle), and transverse (bottom) components. (a) In the homogeneous model, for this source there are weak topographic effects throughout southern California. (b) In the 1D model, there are topographic effects oceanward of the continental shelf, but overall there are relatively weak topographic effects for this source.

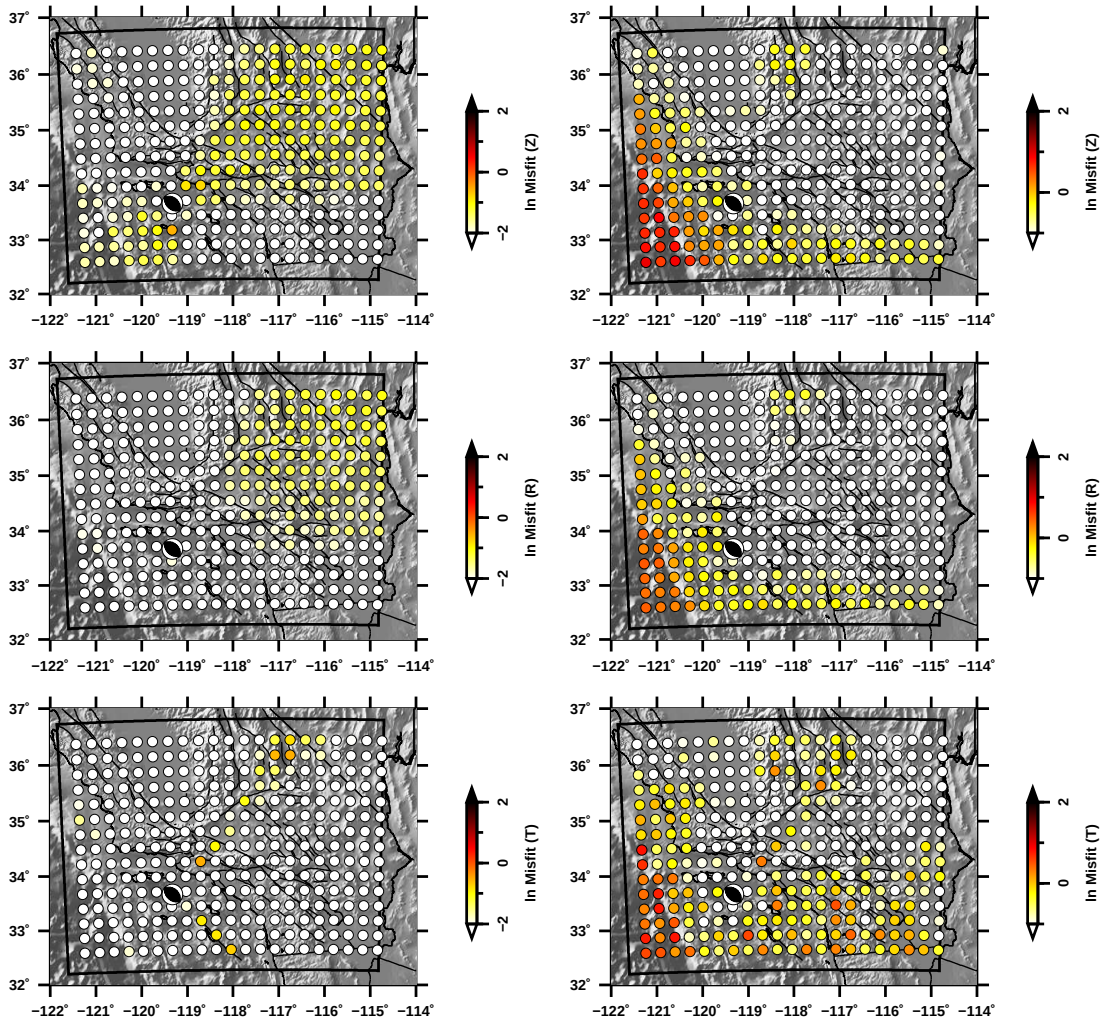

(a) Homogeneous (b) 1D

Figure 3.10: Topographic effects for source 12659440.
Topographic effects for source 12659440 (M_w 4.2, depth 14.1 km) for the vertical (top), radial (middle), and transverse (bottom) components. This is a deep reverse fault from offshore California. (a) The homogeneous model shows some topographic effects in the northeast direction of maximum Rayleigh waves on the vertical and radial components. (b) In the 1D model, there are topographic effects in the Sierra Nevada and oceanward of the continental shelf.

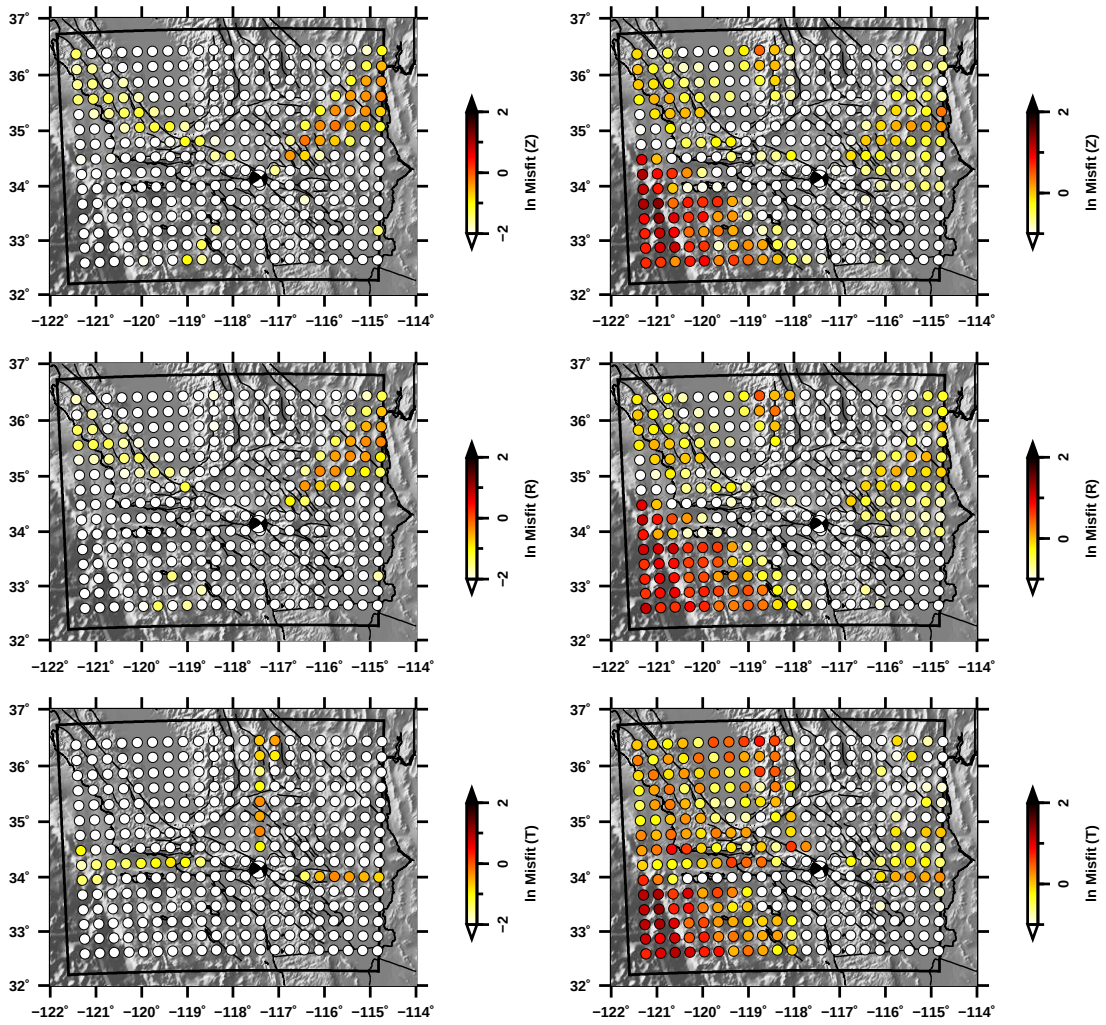

(a) Homogeneous (b) 1D

Figure 3.11: Topographic effects for source 14079184.
Topographic effects for source 14079184 (M_w 3.5, depth 6.3 km) for the vertical (top), radial (middle), and transverse (bottom) components. For both models, there are topographic effects in the nodal directions. The nodal directions are northeast-southeast-southwest-northwest for the Rayleigh waves on the vertical and radial components; they are north-east-south-west for the Love waves on the transverse component. (a) In the homogeneous model, the topographic effect is stronger in the northeast direction for the vertical and radial components. (b) In the 1D model, the topographic effects that are oceanward of the continental shelf and near the San Joaquin valley are also prominent.

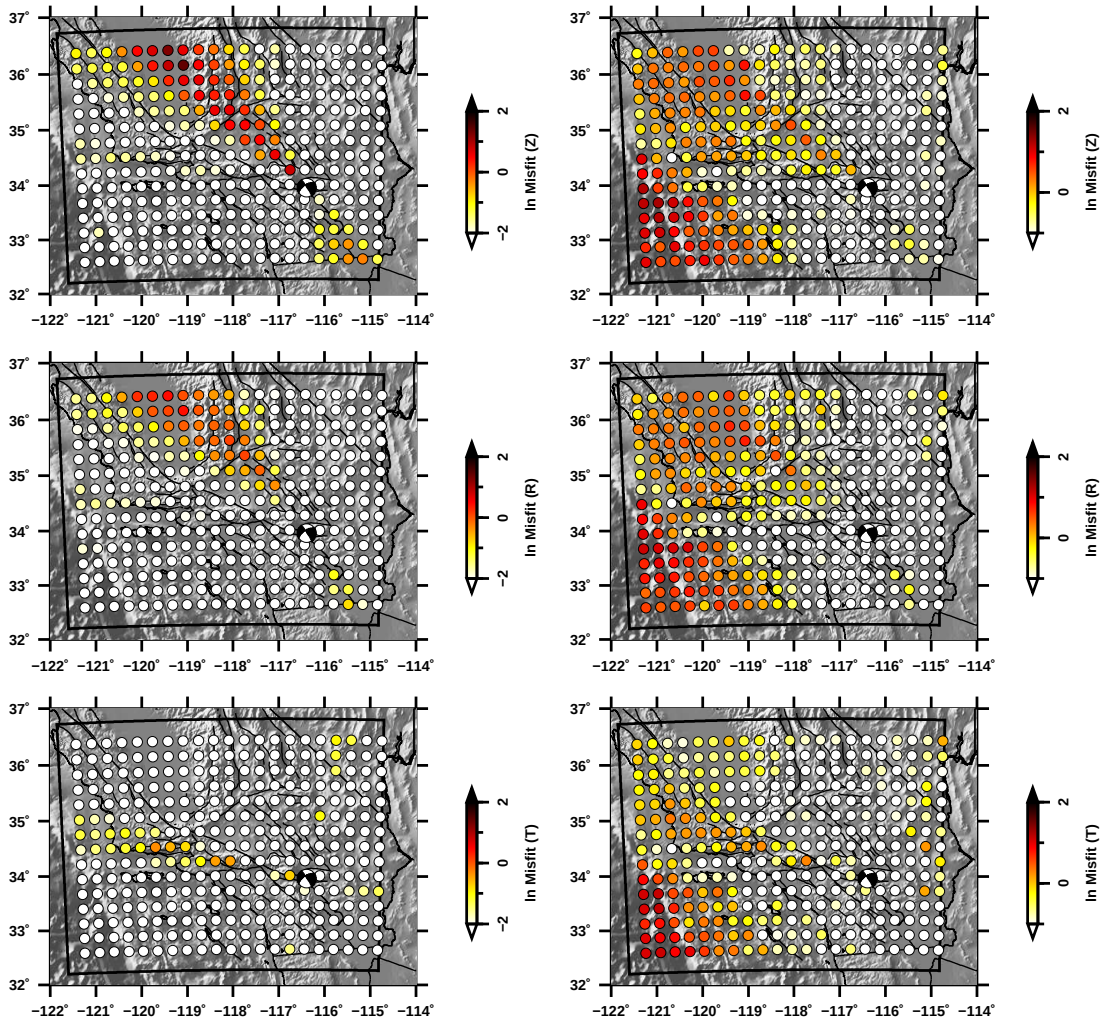

(a) Homogeneous (b) 1D

Figure 3.12: Topographic effects for source 14118096.
Topographic effects for source 14118096 (M_w 3.9, depth 8.5 km) for the vertical (top), radial (middle), and transverse (bottom) components. In the homogeneous case, strong topographic effects occur in the vertical and radial nodal directions toward the San Joaquin valley but small effects occur in other nodal directions. These effects occur in all components of the 1D model but the effect oceanward of the continental shelf is stronger.

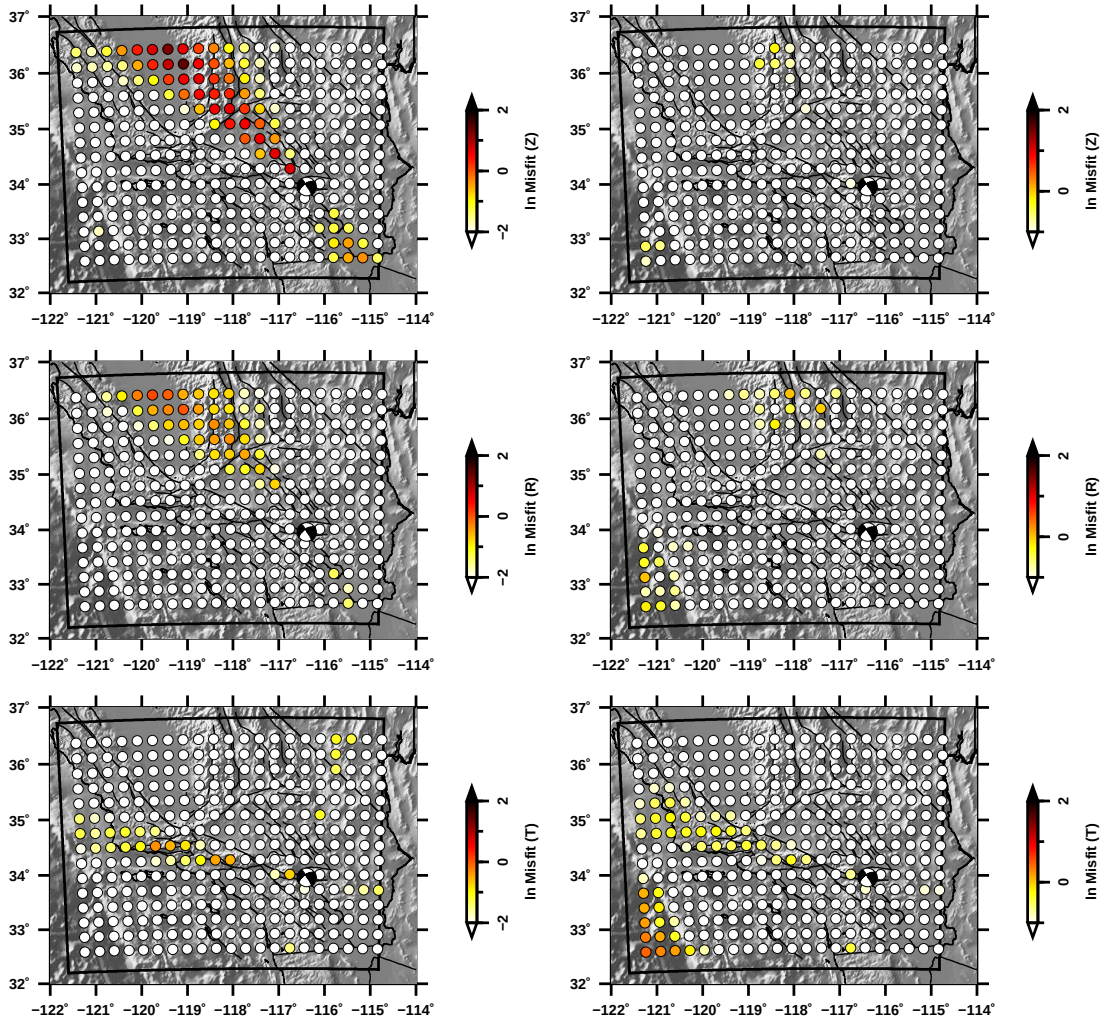

(a) Homogeneous (b) 1D

Figure 3.13: Topographic effects for source 14118096 at the maximum shortest resolvable period. Topographic effects for source 14118096 (M_w 3.9, depth 8.5 km) quantified with the maximum shortest resolvable period over all stations for the vertical (top), radial (middle), and transverse (bottom) components. The maximum shortest resolvable period for the quantification of topography misfit for the homogenous model is :2.17 s (Z), 2.93 s (R), 2.82 s (T), and for the 1D model is :10.45 s (Z), 8.05 s (R), 5.46 s (T). In the homogeneous model, topographic effects are visible in some nodal directions for all the components (compare with Figure 3.12). These effects are less noticeable in the 1D model.

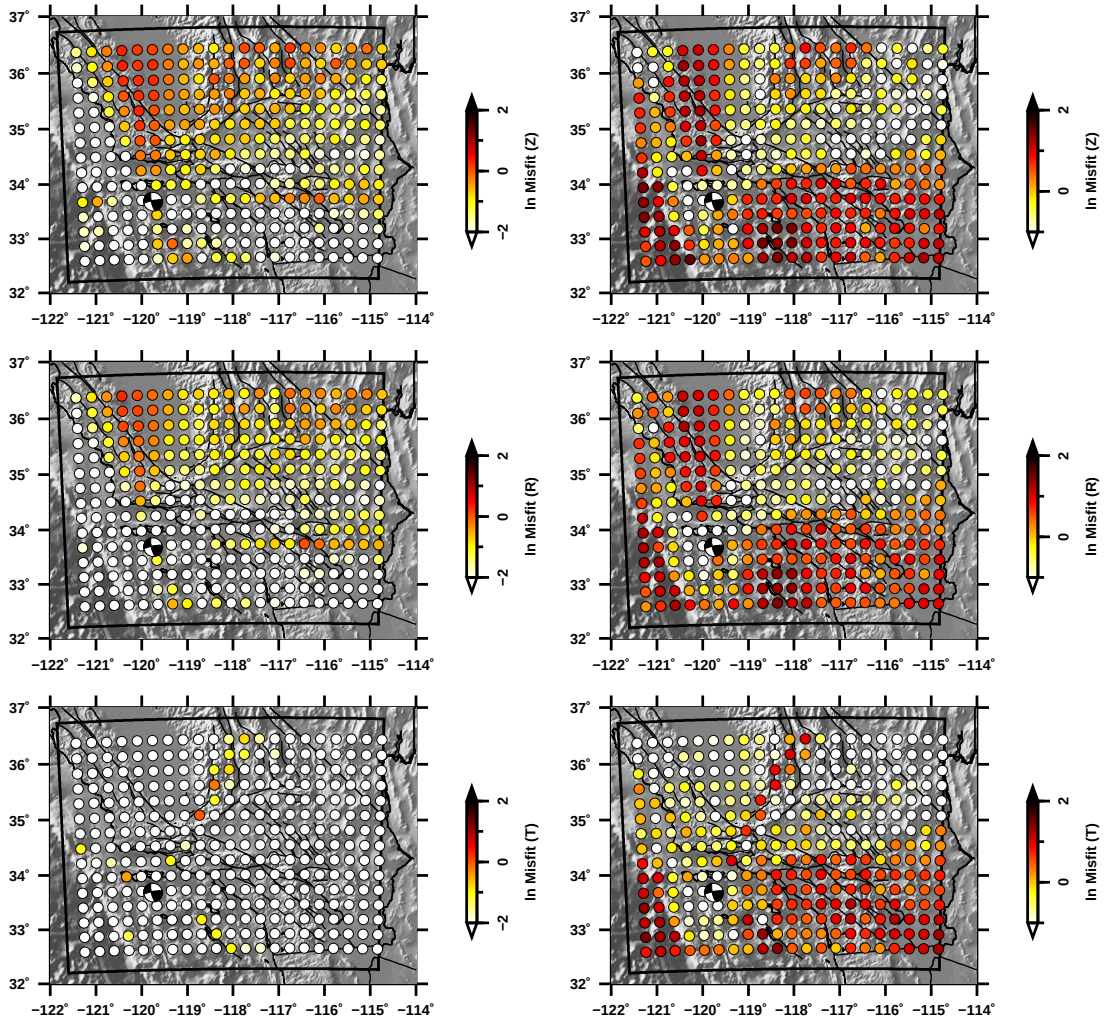

(a) Homogeneous (b) 1D

Figure 3.14: Topographic effects for source 14165408.
Topographic effects for source 14165408 (M_w 3.8, depth 3.9 km) for the vertical (top), radial (middle), and transverse (bottom) components. Strong topographic effects occur in the direction towards the San Joaquin valley and the Sierra Nevada. In the 1D model, the area on the southeast also has strong topographic effects.

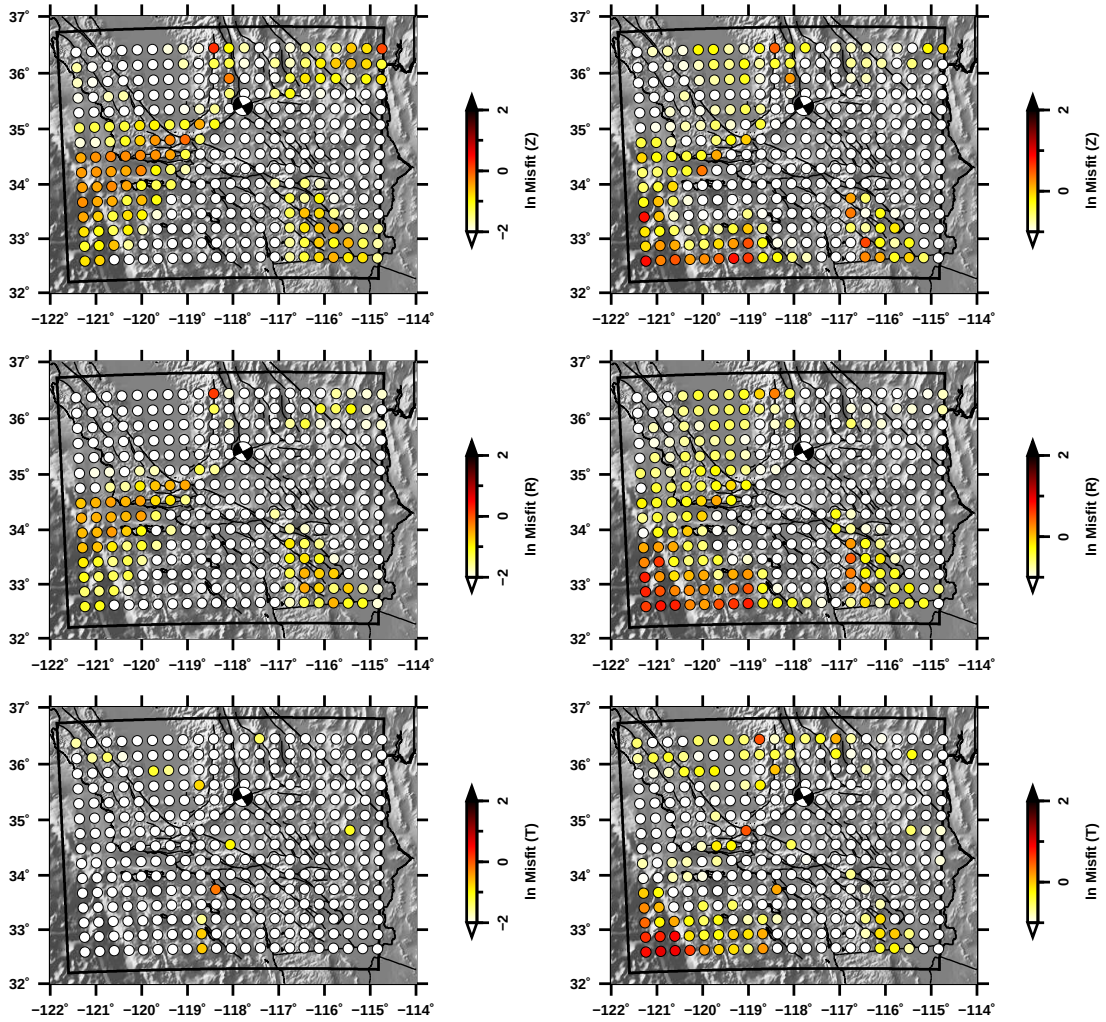

(a) Homogeneous (b) 1D

Figure 3.15: Topographic effects for source 14418600.
Topographic effects for source 14418600 (M_w 3.9, depth 8.5 km) for the vertical (top), radial (middle), and transverse (bottom) components. (a) In the homogeneous model, topographic effects occur in the Rayleigh wave nodal directions on the vertical and radial components. These effects, however, are suppressed in the southeast direction before the waves propagate through the San Bernadino mountains. This implies that the topographic effects to the west are accrued early, near the source, whereas to the south they accrue near the San Bernadino mountains.

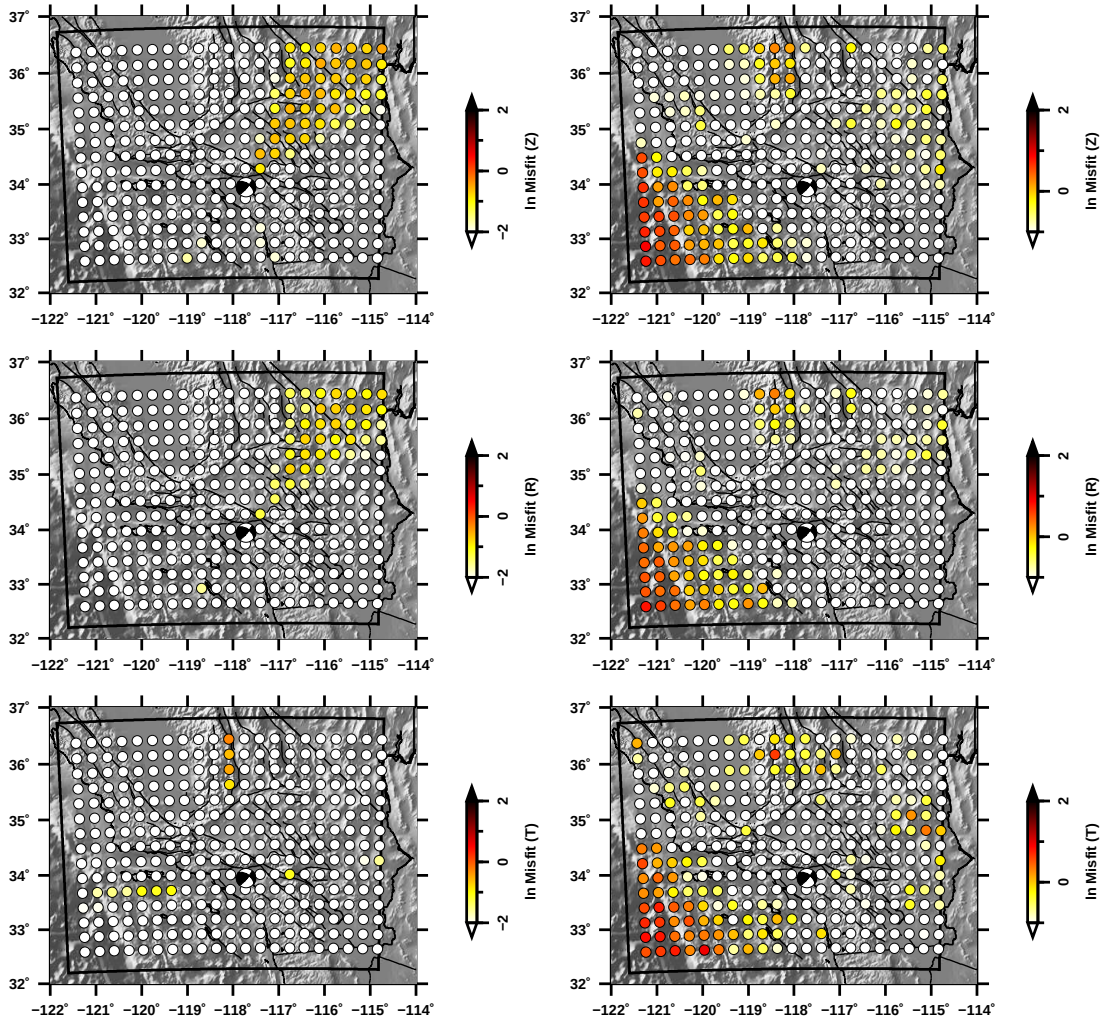

(a) Homogeneous (b) 1D

Figure 3.16: Topographic effects for source 9038699.
Topographic effects for source 9038699 (M_w 3.9, depth 13 km) for the vertical (top), radial (middle), and transverse (bottom) components. Strong topographic effects occur in the direction toward the Mojave desert on the vertical and radial components. Even though the effects of topography are generally weak in this area (Figure 3.20), this example demonstrates that stronger topographic effects in the desert where there are no high contrasts in topography are feasible for a specific source. The effects of topography are stronger in the Sierra Nevada and oceanward of the continental shelf in the 1D model.

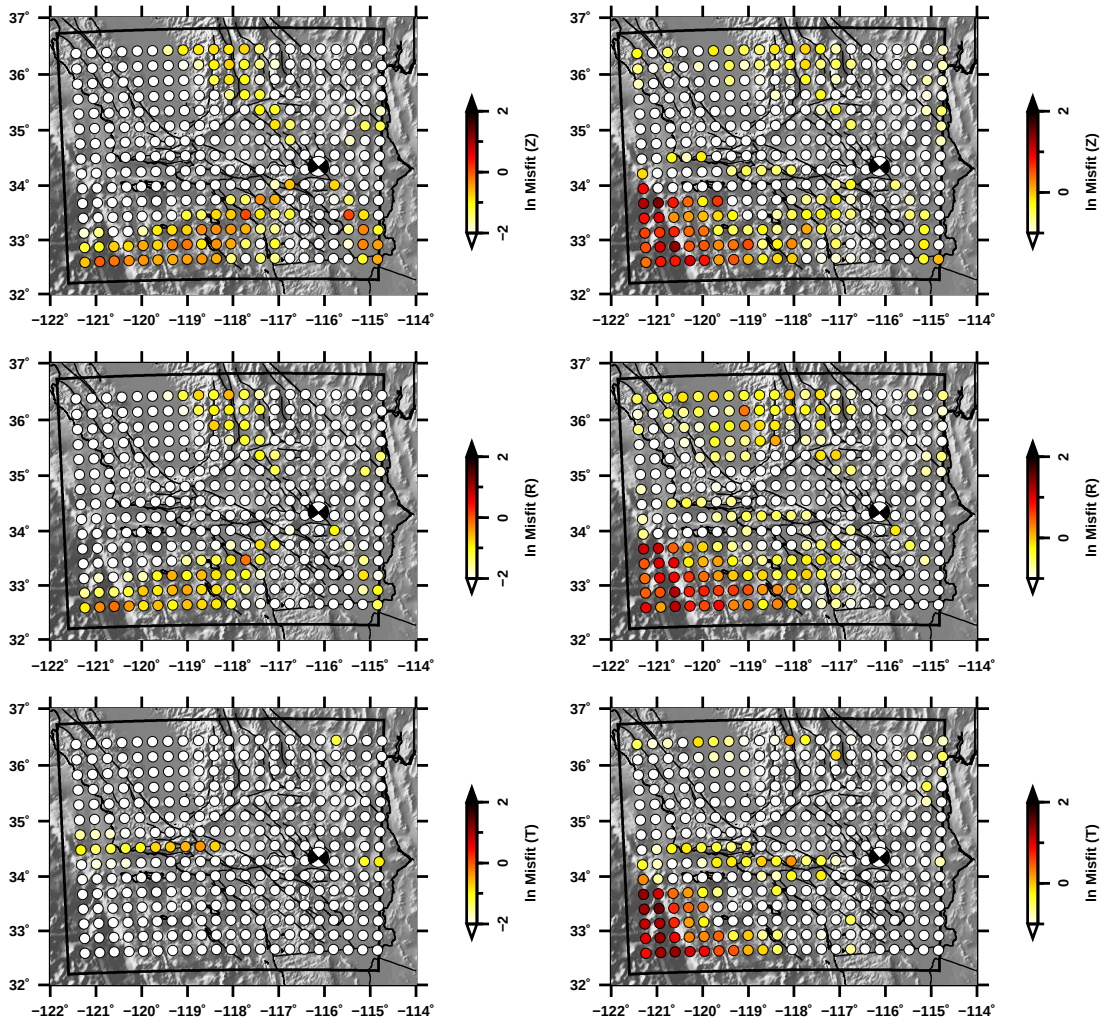

(a) Homogeneous (b) 1D

Figure 3.17: Topographic effects for source 9110685.
Topographic effects for source 9110685 (M_w 4.1, depth 4 km) for the vertical (top), radial (middle), and transverse (bottom) components. In the homogeneous model, there are some topographic effects in the nodal directions, especially toward the southwest and southeast for the vertical and radial components and toward the west for the transverse component. These effects are visible for the 1D model, though they are not as strong as the effect oceanward of the continental shelf.

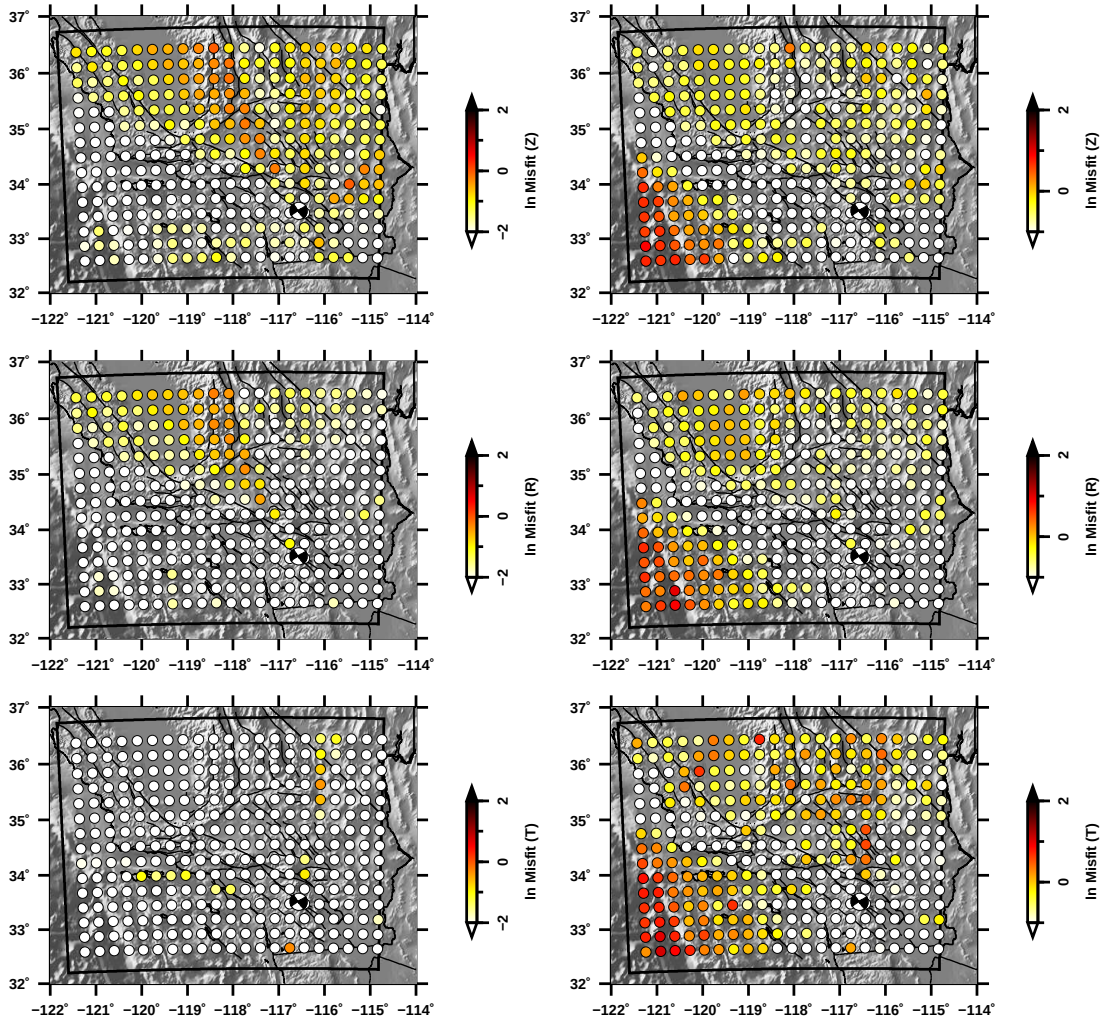

(a) Homogeneous (b) 1D

Figure 3.18: Topographic effects for source 9853417.
Topographic effects for source 9853417 (M_w 3.5, depth 13.5 km) for the vertical (top), radial (middle), and transverse (bottom) components. (a) For the homogeneous model, topographic effects can be seen in the Rayleigh wave nodal direction toward the San Joaquin valley, as well as in the non-nodal directions of the Sierra Nevada and Mojave desert. (b) Topographic effects can be seen oceanward of the continental shelf, as well as in the regions of the San Joaquin valley, the Sierra Nevada, and the Mojave desert.

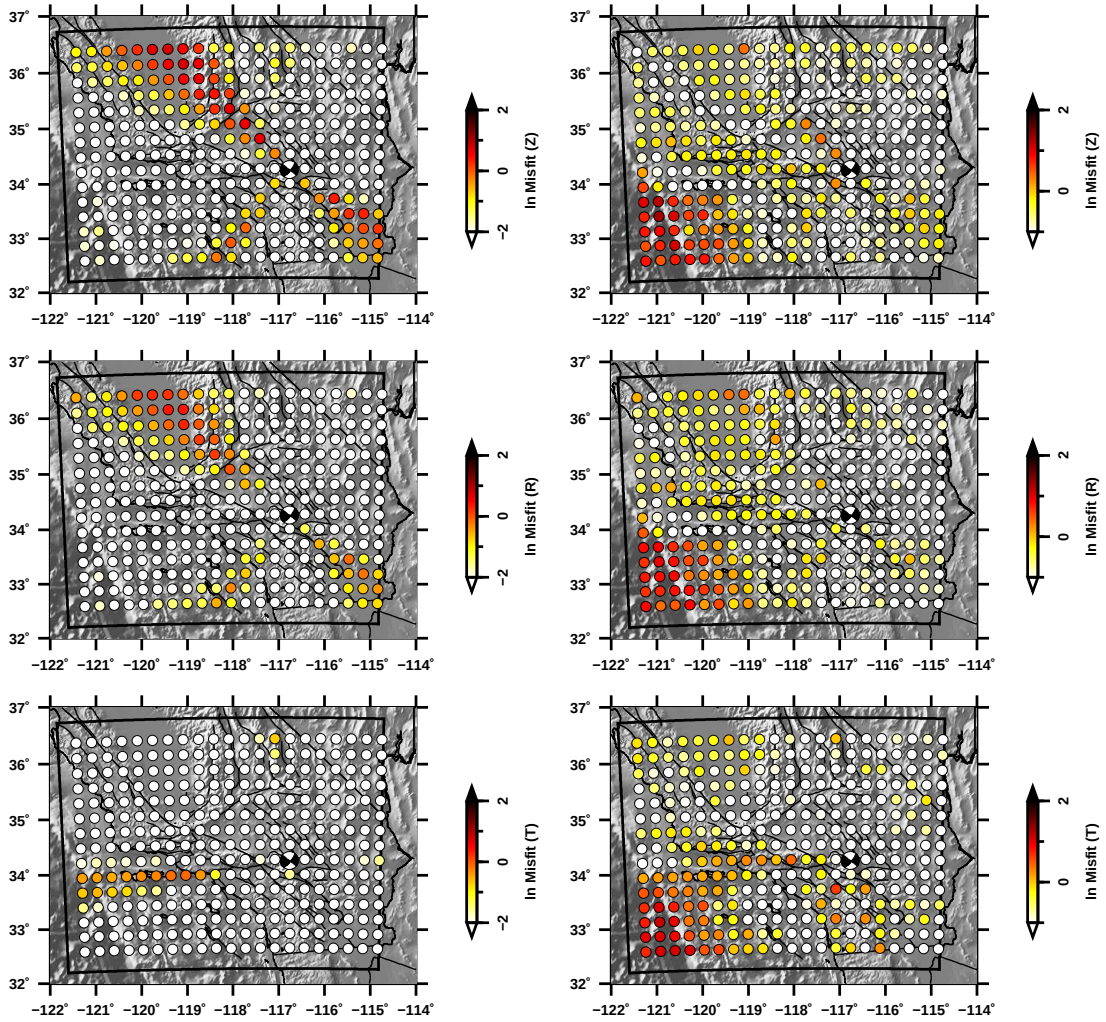

(a) Homogeneous (b) 1D

Figure 3.19: Topographic effects for source 9169867.
Topographic effects for source 9169867 (M_w 3.8, depth 3.7 km) for the vertical (top), radial (middle), and transverse (bottom) components. (a) Strong topographic effects are seen in the Rayleigh wave nodal directions on the vertical and radial components, with the exception of the northeast direction. Only the Love wave nodal direction to the west exhibits topographic effects on the transverse component. (b) In the 1D model, the effect oceanward of the continental shelf is stronger than in the nodal directions.

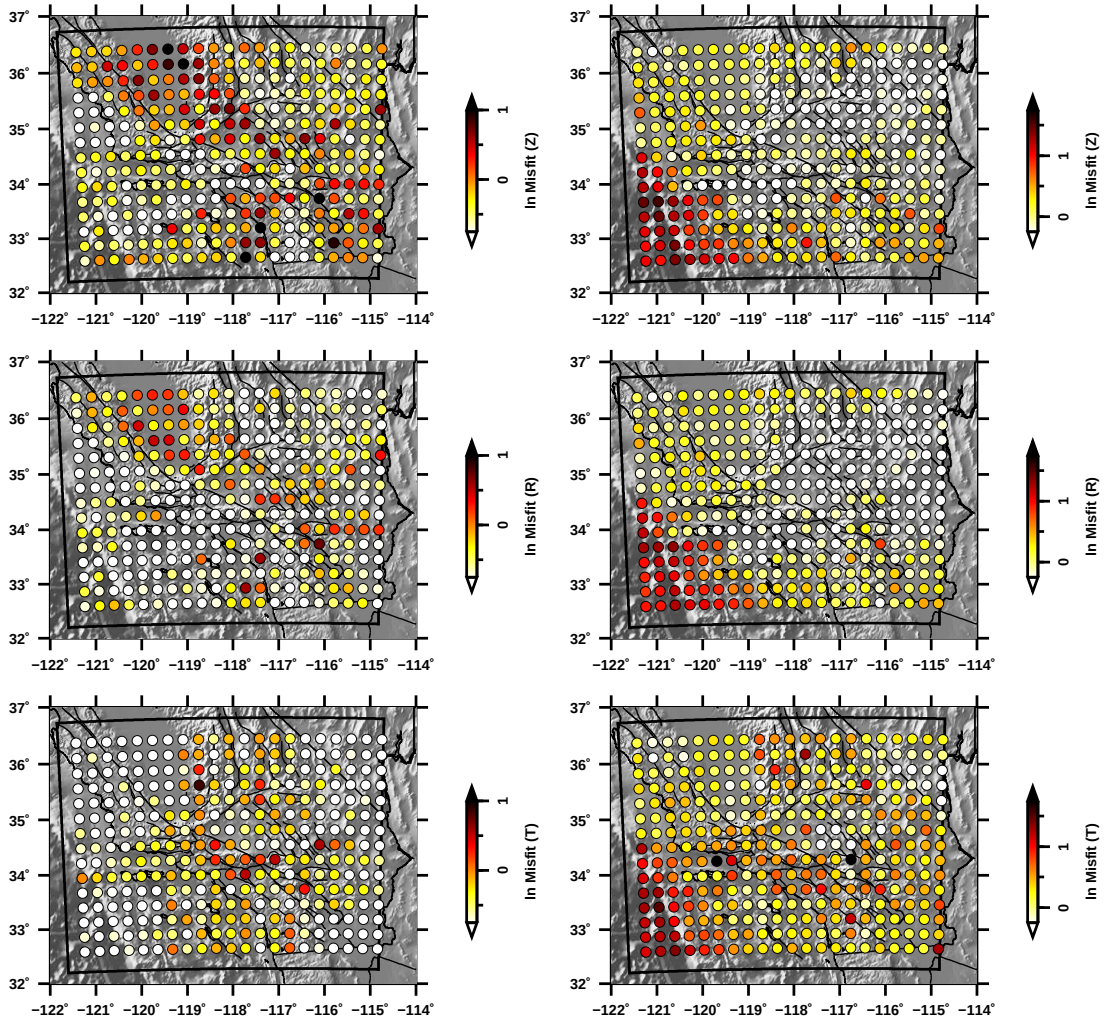

(a) Homogeneous (b) 1D

Figure 3.20: Cumulative topographic effects for each station.
For each station, the color represents 90% of the cumulative sum (e.g., Figure 3.7) of the quantification of topography misfit over all 137 sources. The presence of spatially coherent patterns implies that these effects are not caused by any source effects, since the source effects should be mostly averaged out in this representation. (a) In the homogeneous model, topographic effects are strongest in the San Joaquin valley. (b) In the 1D model, topographic effects are strongest oceanward of the continental shelf and weakest in the Mojave desert.

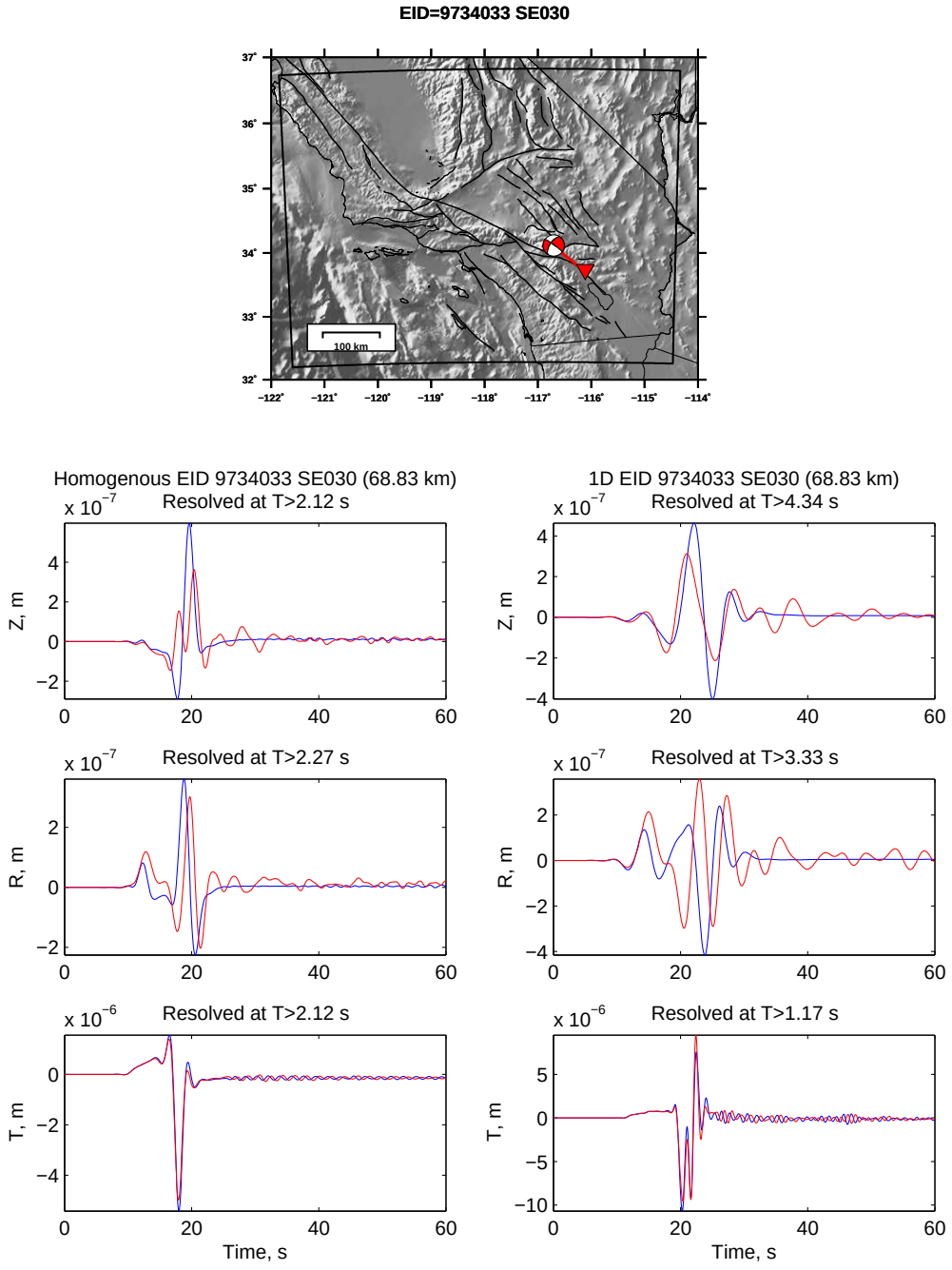

(a) Homogeneous (b) 1D

Figure 3.21: Topographic effects for path 9734033 to SE030.
The effect is shown for the vertical (top), radial (middle), and transverse (bottom) components. The blue and red waveforms are produced by meshes whose surface is flat or with topography, respectively. This is one of the paths that produces strong topographic effects as observed in Figure 3.20.

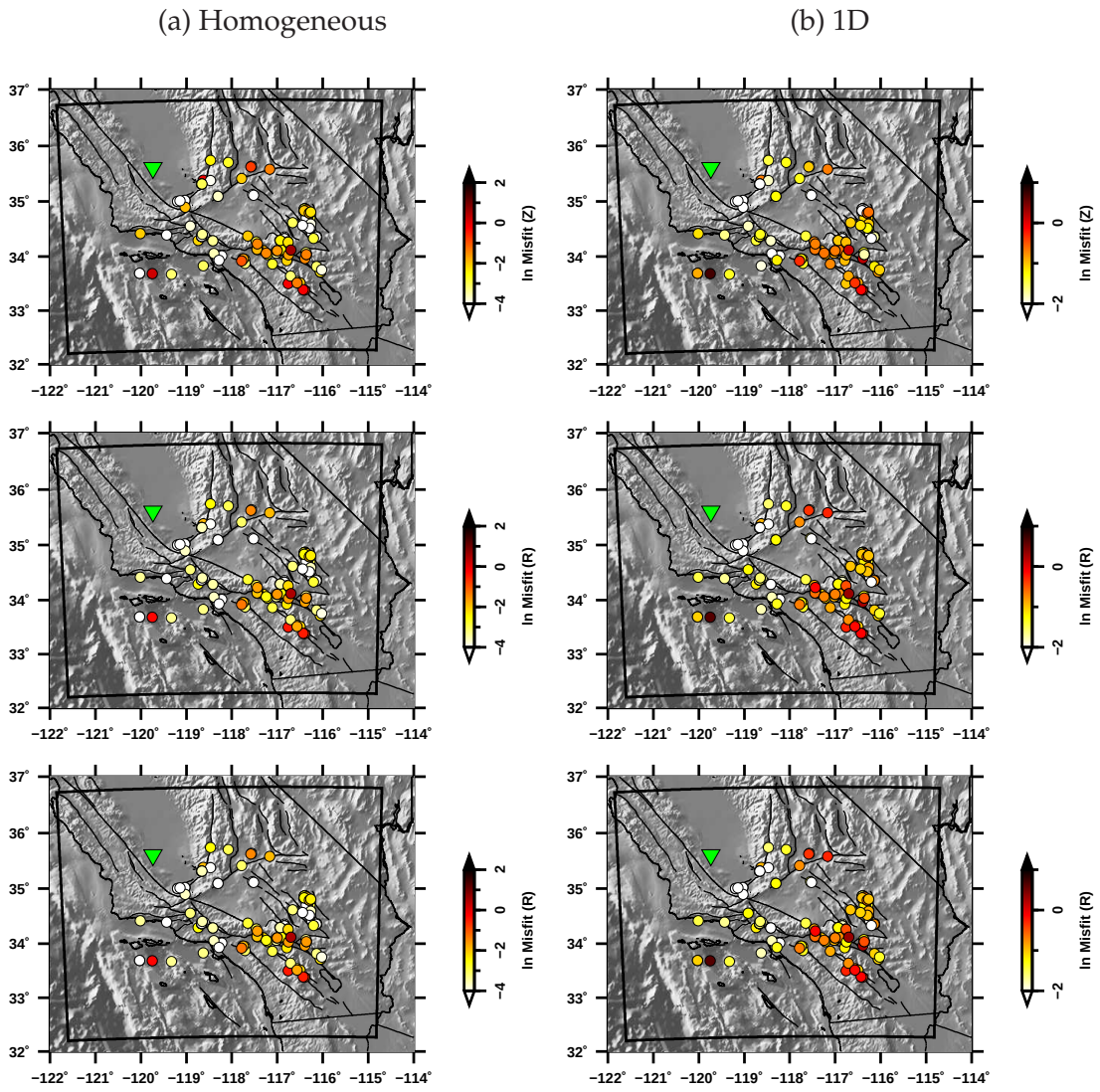

Figure 3.22: Topographic effects for station NW028.
Topographic effects for station NW028 due to each of the 137 sources, for the vertical (top), radial (middle), and transverse (bottom) components. Strong topographic effects are seen from sources east of the Sierra Nevada and from sources near the San Bernardino mountains. This can be observed in both the homogeneous and 1D models.

(a) Homogeneous (b) 1D

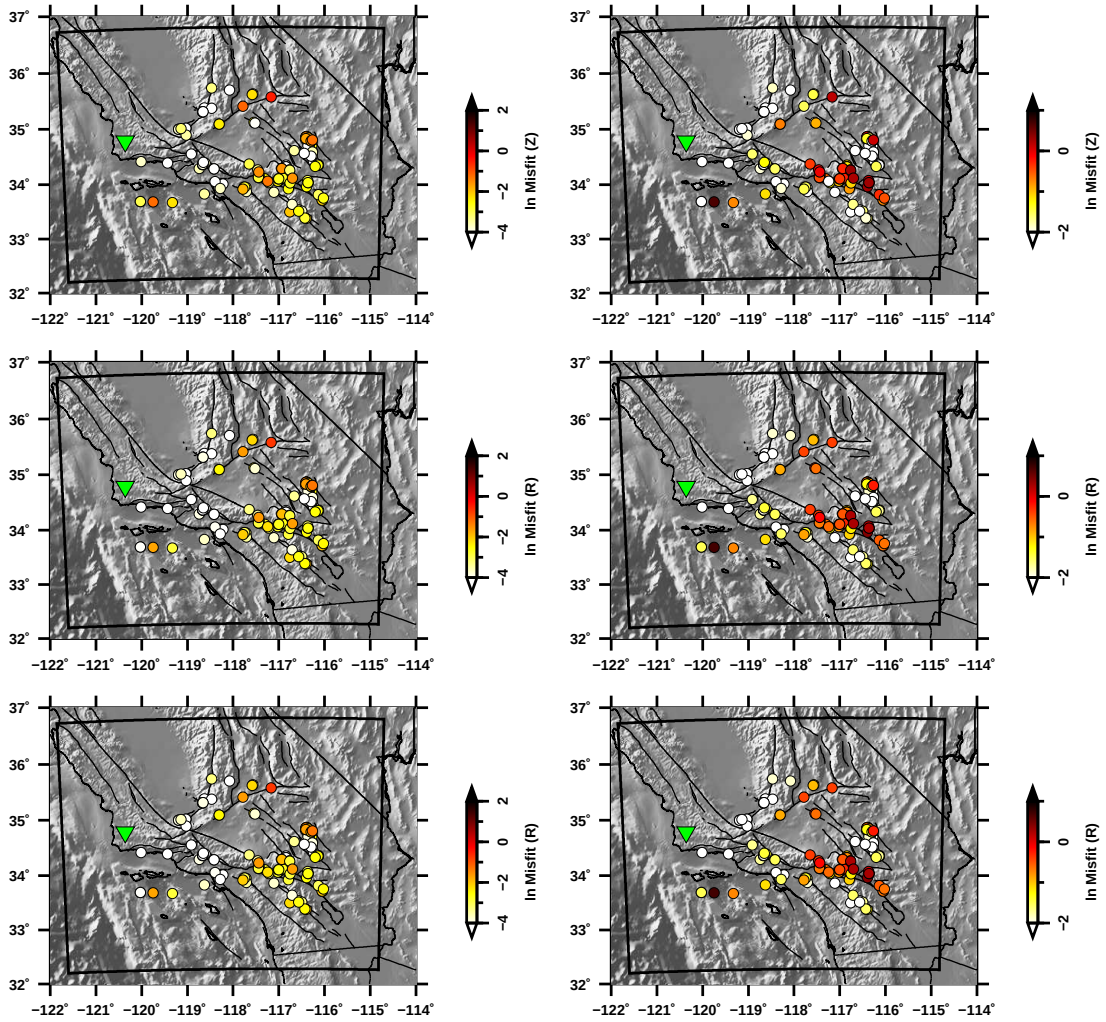

Figure 3.23: Topographic effects for station NW033.
Topographic effects for station NW033 due to each of the 137 sources, for the vertical (top), radial (middle), and transverse (bottom) components. Strong topographic effects are seen from sources east of the Sierra Nevada and from sources near the San Bernardino mountains. This can be observed in both the homogeneous and 1D models. Topographic effects from the San Bernardino mountains are stronger in the 1D model than in the homogeneous model.

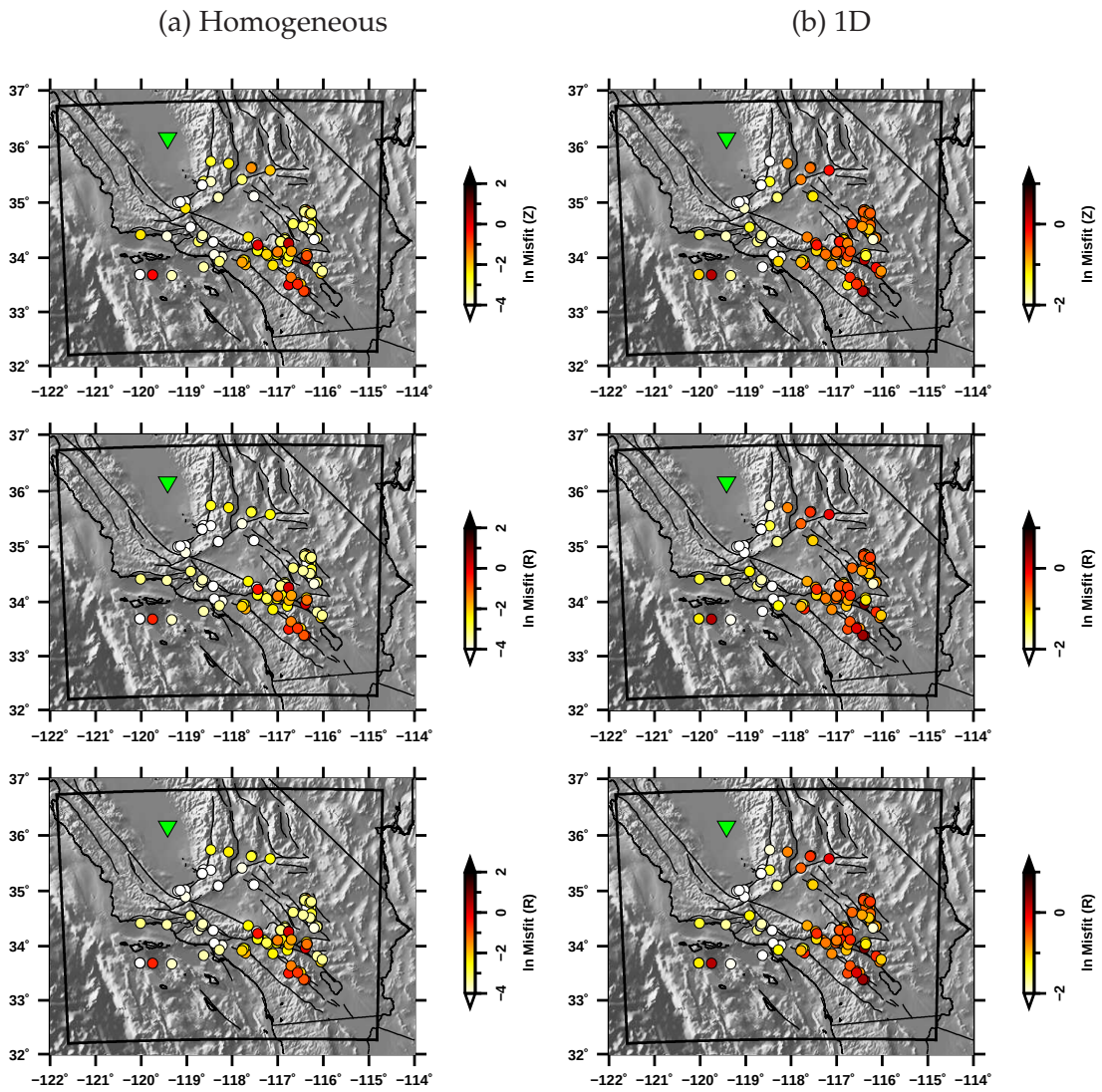

Figure 3.24: Topographic effects for station NW034.
Topographic effects for station NW034 due to each of the 137 sources, for the vertical (top), radial (middle), and transverse (bottom) components. Strong topographic effects are seen from sources east of the Sierra Nevada and from sources near the San Bernardino mountains. This can be observed in both the homogeneous and 1D models, although the 1D model shows stronger effects.

(a) Homogeneous (b) 1D

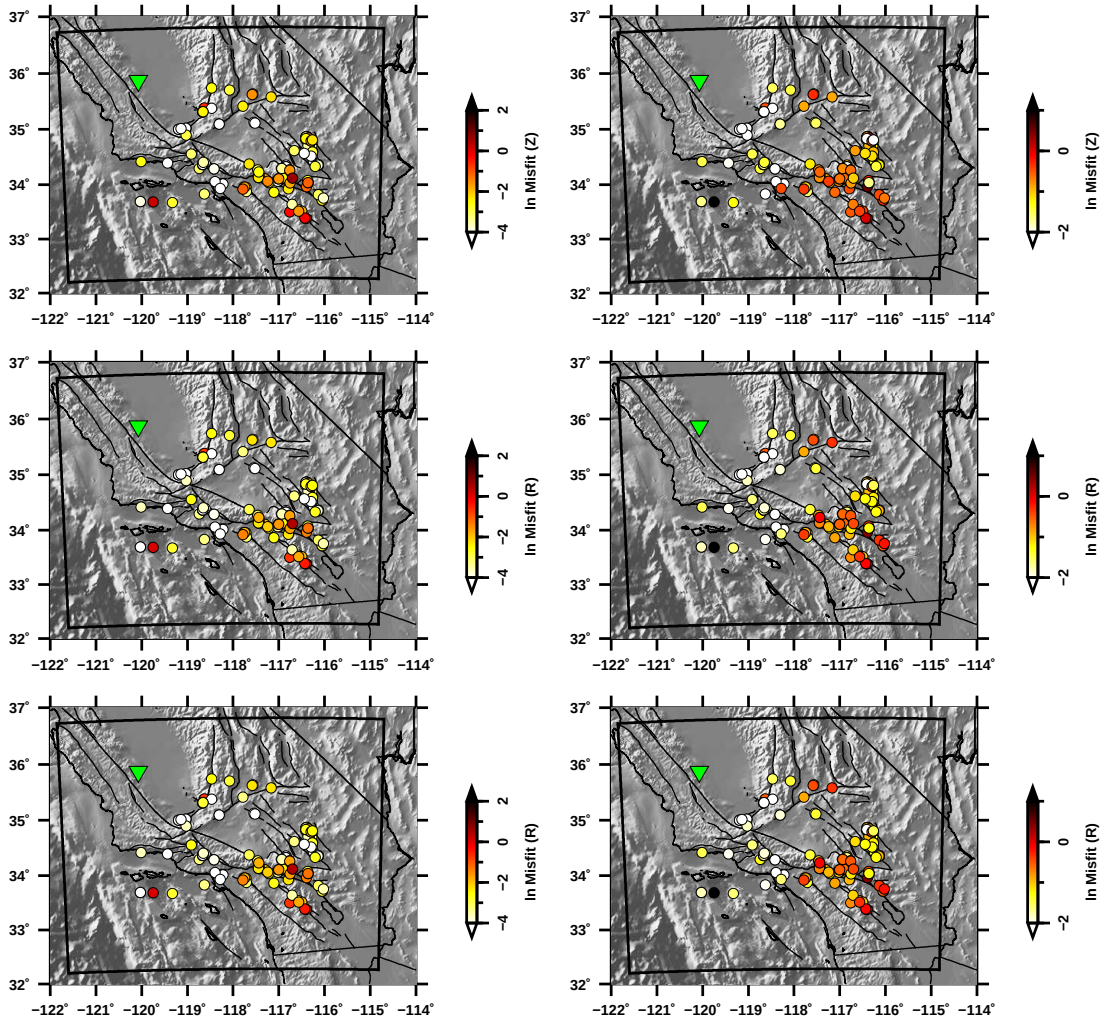

Figure 3.25: Topographic effects for station NW041.
Topographic effects for station NW041 due to each of the 137 sources, for the vertical (top), radial (middle), and transverse (bottom) components. Strong topographic effects are seen from sources on the east part of the Sierra Nevada and from sources near the San Bernardino mountains. This can be observed in both the homogeneous and 1D models, although the 1D model shows stronger effects.

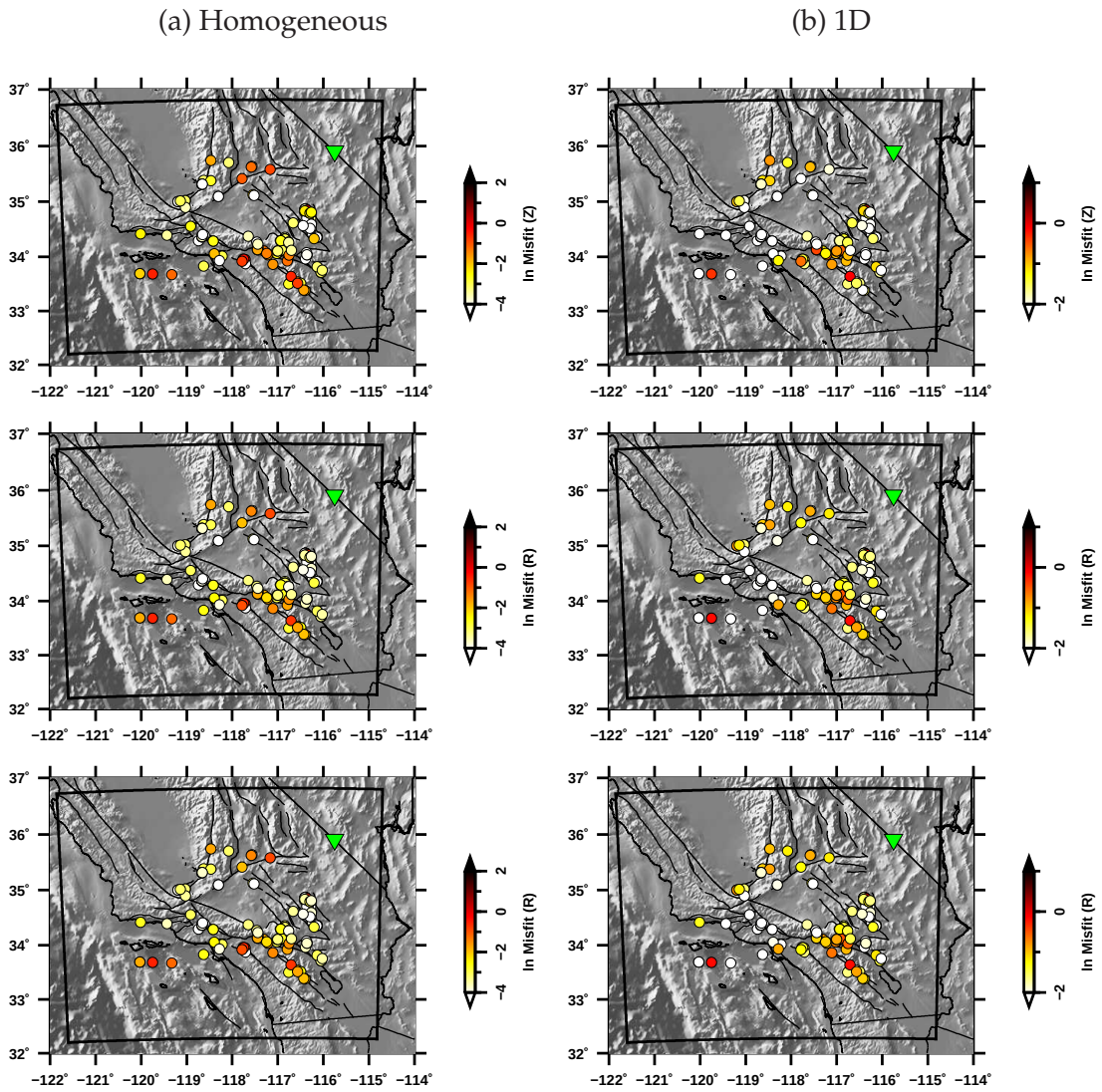

Figure 3.26: Topographic effects for station NE064.
Topographic effects for station NE064 due to each of the 137 sources, for the vertical (top), radial (middle), and transverse (bottom) components. Strong topographic effects are seen from sources on the east part of the Sierra Nevada and from sources near the San Bernardino mountains. This can be observed in both the homogeneous and 1D models, although the 1D model shows stronger effects. The effects of topography with increasing distance for this station can be observed in Figure 3.27.

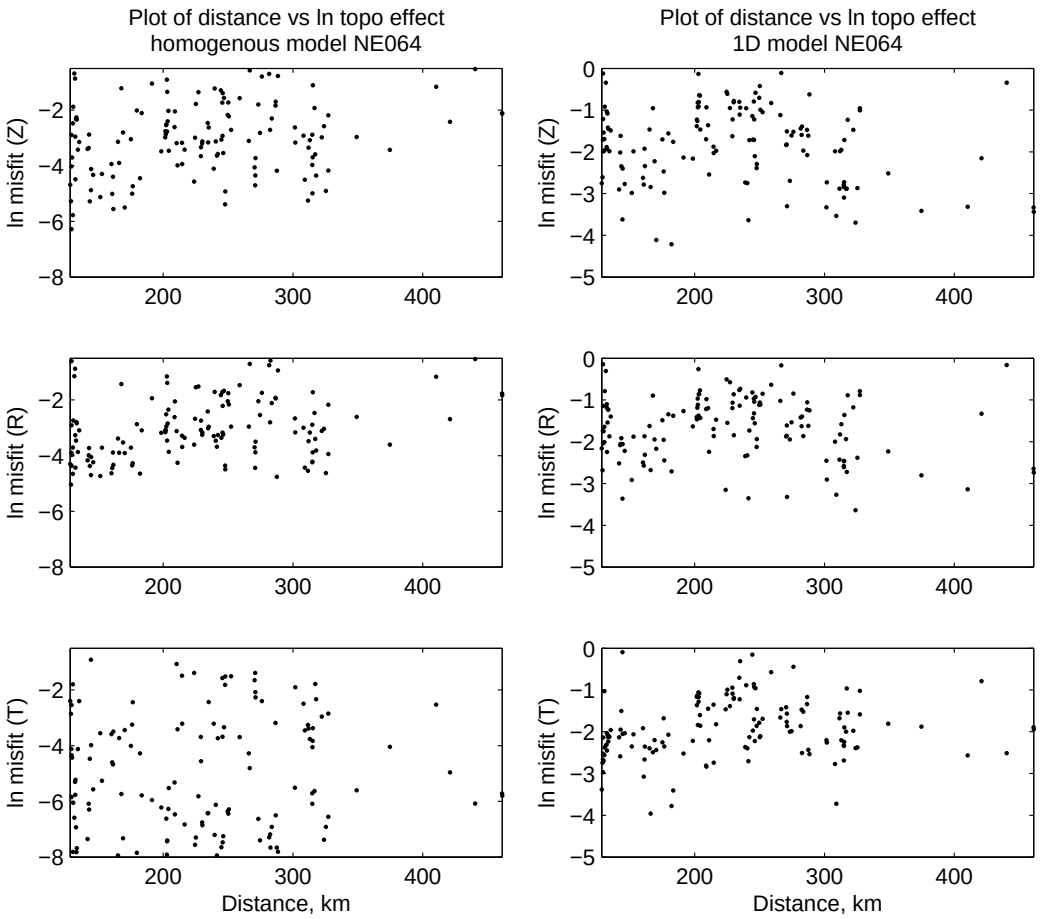

(a) Homogeneous (b) 1D

Figure 3.27: Topographic effects with increasing source distance from station NE064.
Unlike the general relationship of topographic effects with increasing distance as seen in Figure 3.5, the effects of topography are not increasing with distance for this specific station. The station-specific plot for NE064 is in Figure 3.26.

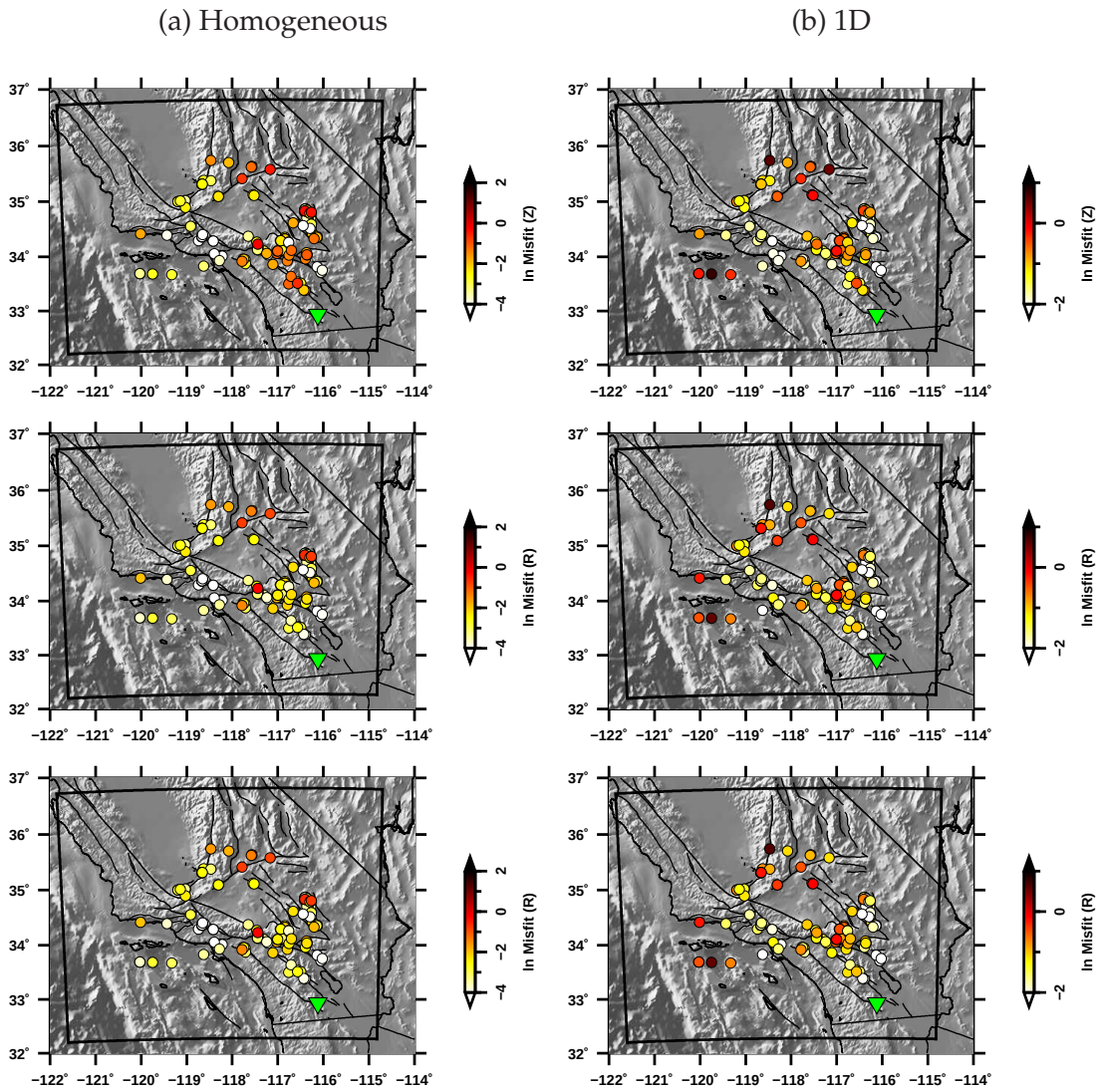

Figure 3.28: Topographic effects for station SE046.
Topographic effects for station SE046 for the vertical (top), radial (middle), and transverse (bottom) components. Topographic effects at a station in the southeast region (SE046) due to each of the 137 sources. Strong topographic effects are seen from sources on the east part of the Sierra Nevada and from sources near the San Bernardino mountains. This can be observed in both the homogeneous and 1D models. The effects are from closer path distance for the vertical component in the homogeneous model.

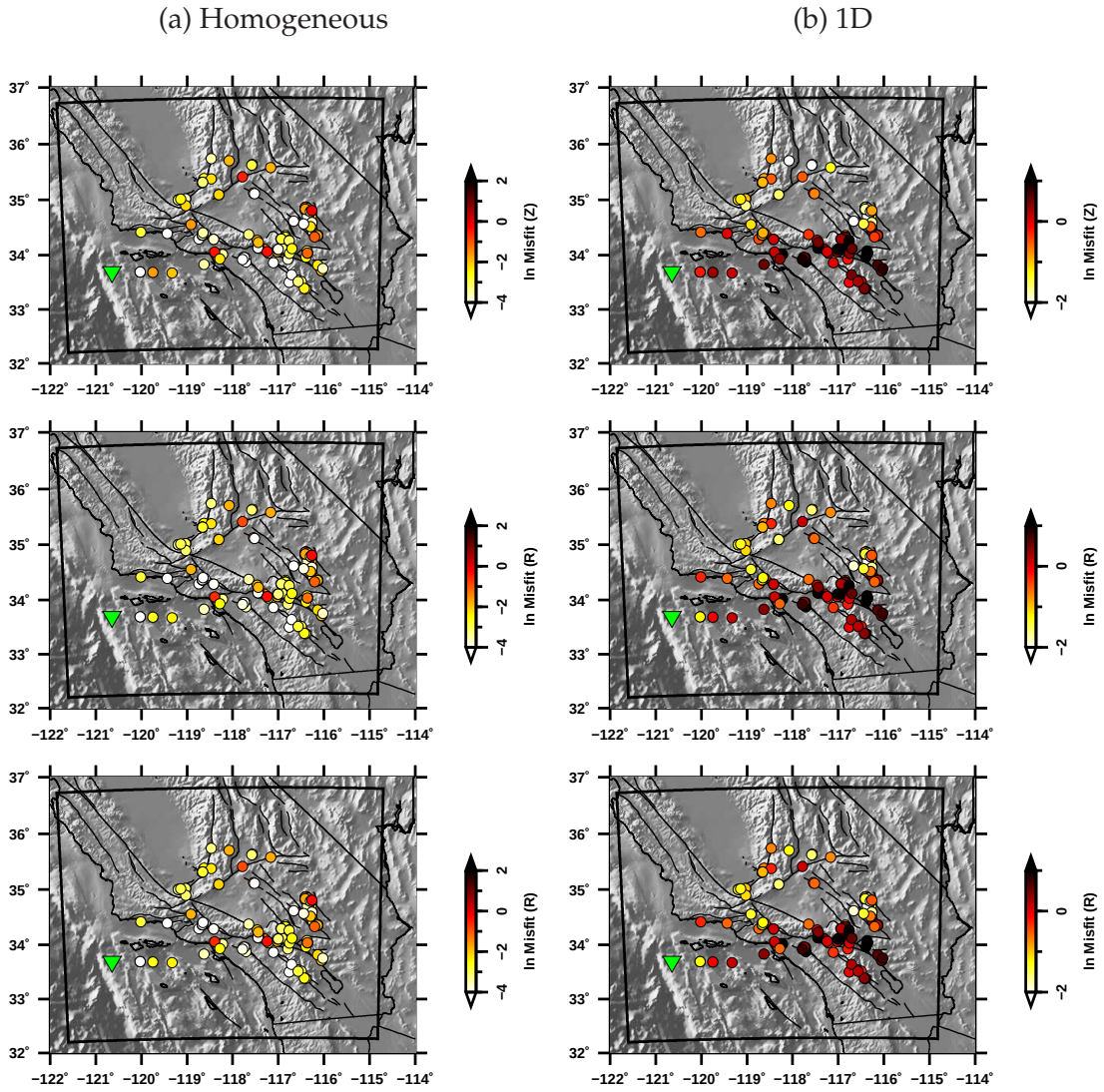

Figure 3.29: Topographic effects for station SW062.
Topographic effects for station SW062 for the vertical (top), radial (middle), and transverse (bottom) components. Topographic effects at a station in the southwest region (SW062) due to each of the 137 sources. These strong effects can also be observed in Figure 3.20. Strong topographic effects are seen in the 1D model especially from the sources to the east of the stations. These effects increase with distance at first but drop down as the path propagates away from near the San Bernardino mountains and towards the Mojave desert. Hot spots are observed in a clustered source in the San Bernardino mountains of the transverse component homogeneous model (Figure 3.36).

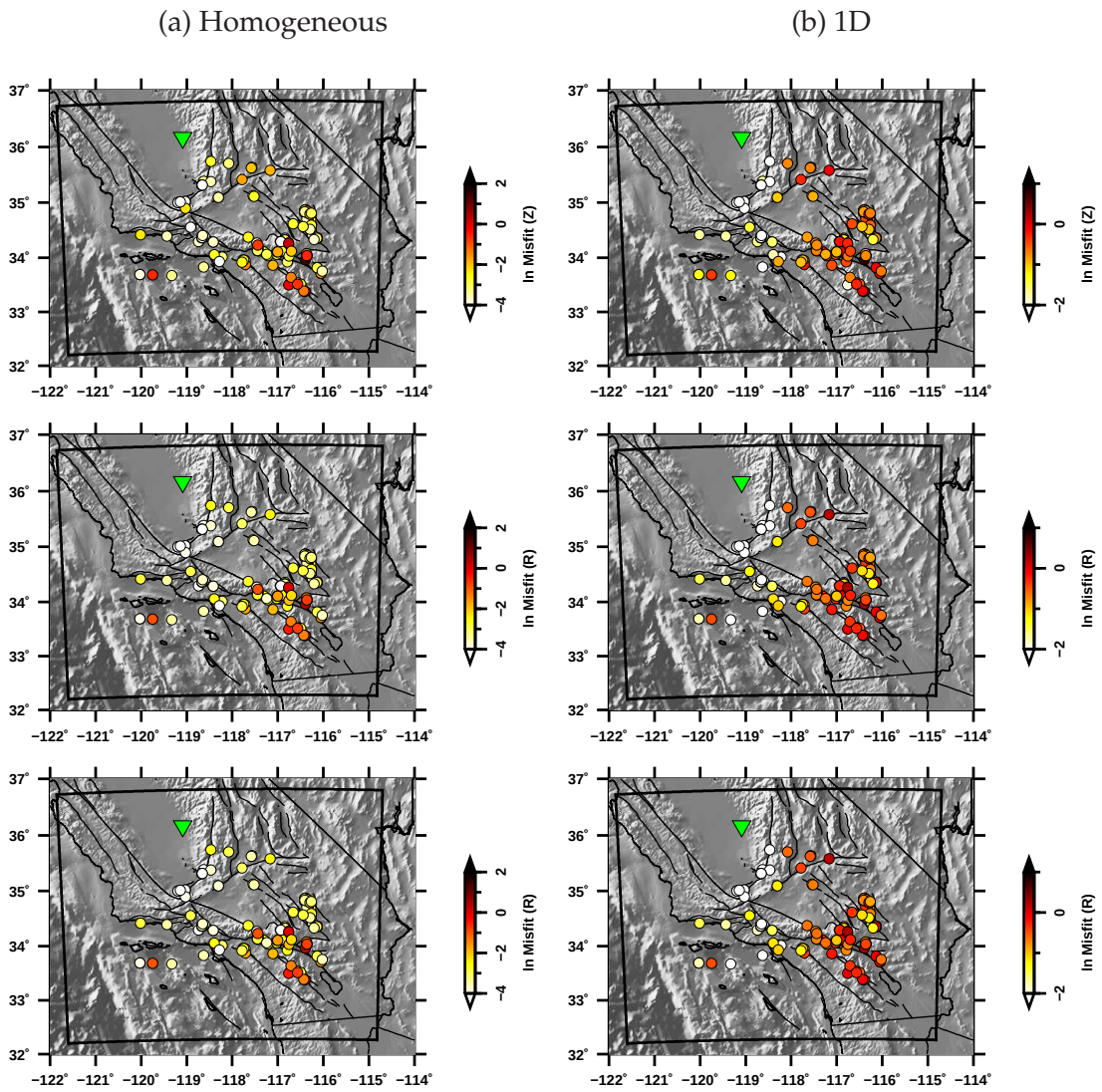

Figure 3.30: Topographic effects for station NW029

Topographic effects for station NW029 for the vertical (top), radial (middle), and transverse (bottom) components. Topographic effects at a station in the northwest region (NW029) due to each of the 137 sources. Strong topographic effects are seen from sources on the eastern part of the Sierra Nevada and from sources near the San Bernardino mountains. This can be observed in both the homogeneous and 1D model.

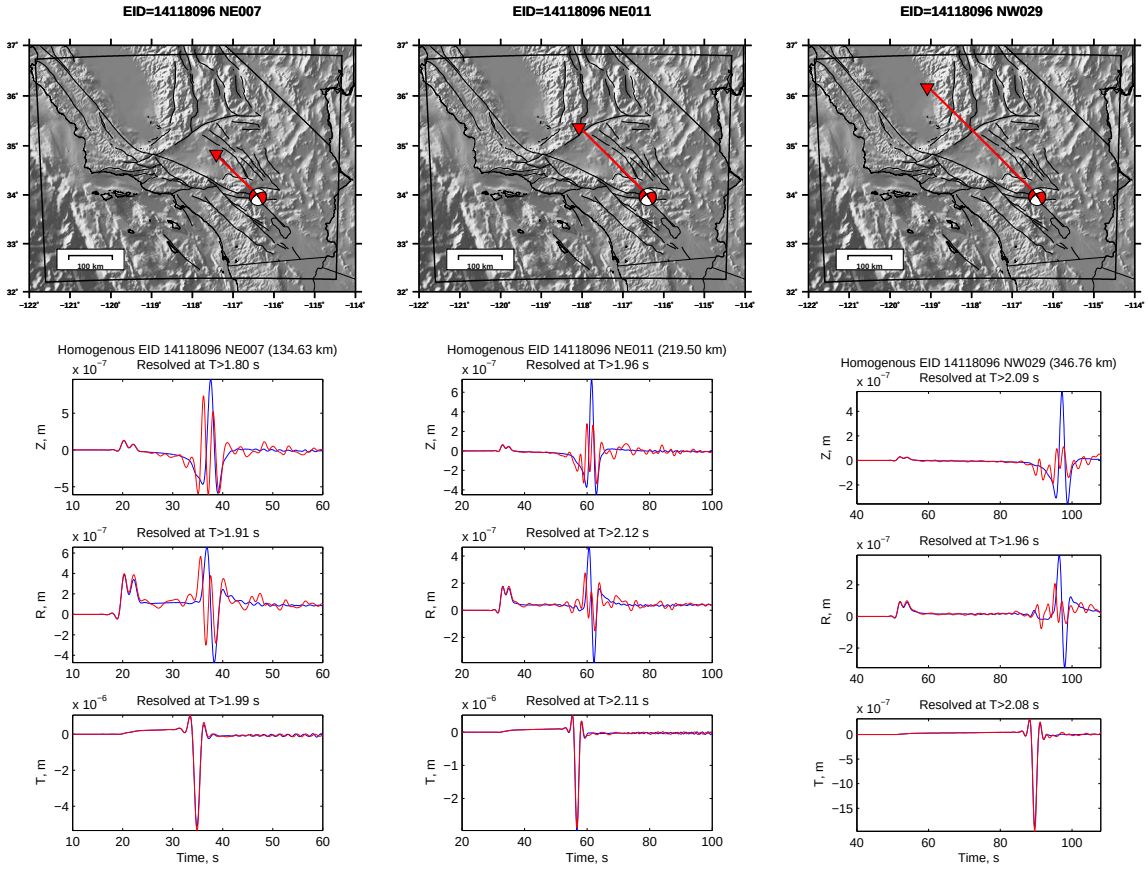

(a) station NE007 (b) station NE011 (c) station NW029

Figure 3.31: Waveforms for path 14118096 propagating northwest in the homogeneous model. Waveform comparison for path 14118096 to three northwest stations in the homogeneous model. The effect is shown for the vertical (top), radial (middle), and transverse (bottom) components. The blue and red waveforms are produced by meshes whose surface is flat or with topography, respectively. Three stations from (a) to (c) are selected to investigate accumulated topographic effects in the homogeneous model with increasing path length toward the San Joaquin valley (Figure 3.12). Amplitude changes and post-surface-wave coda are more noticeable for the topographic waveforms on the vertical and radial components. At NE011 (b), deamplification is more noticeable in the vertical and radial components compared to NE007 (a) implying that the topographic effects are accrued at this location. The furthest station (c), within the San Joaquin valley, exhibits even stronger topographic effects compared to the two stations closer to the source.

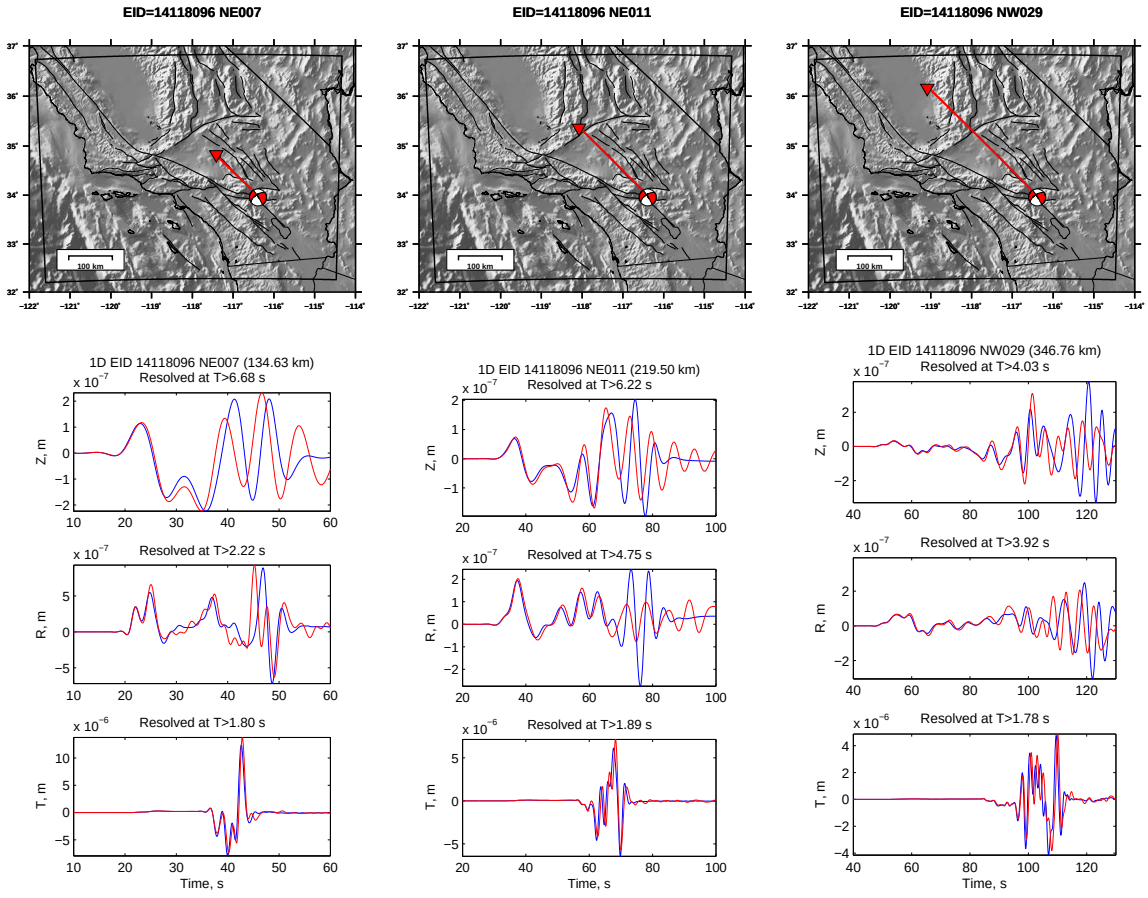

(a) NE007 (b) NE011 (c) NW029

Figure 3.32: Waveforms for path 14118096 propagating northwest for the 1D model.
Same as Figure 3.31, but for the 1D model instead of the homogeneous model. Amplitude and phase differences are more noticeable within the nodal Rayleigh waves on the vertical and radial components. There is a gradual deamplification in the Rayleigh wave for the vertical component, implying that the topographic effect is strengthening with distance.

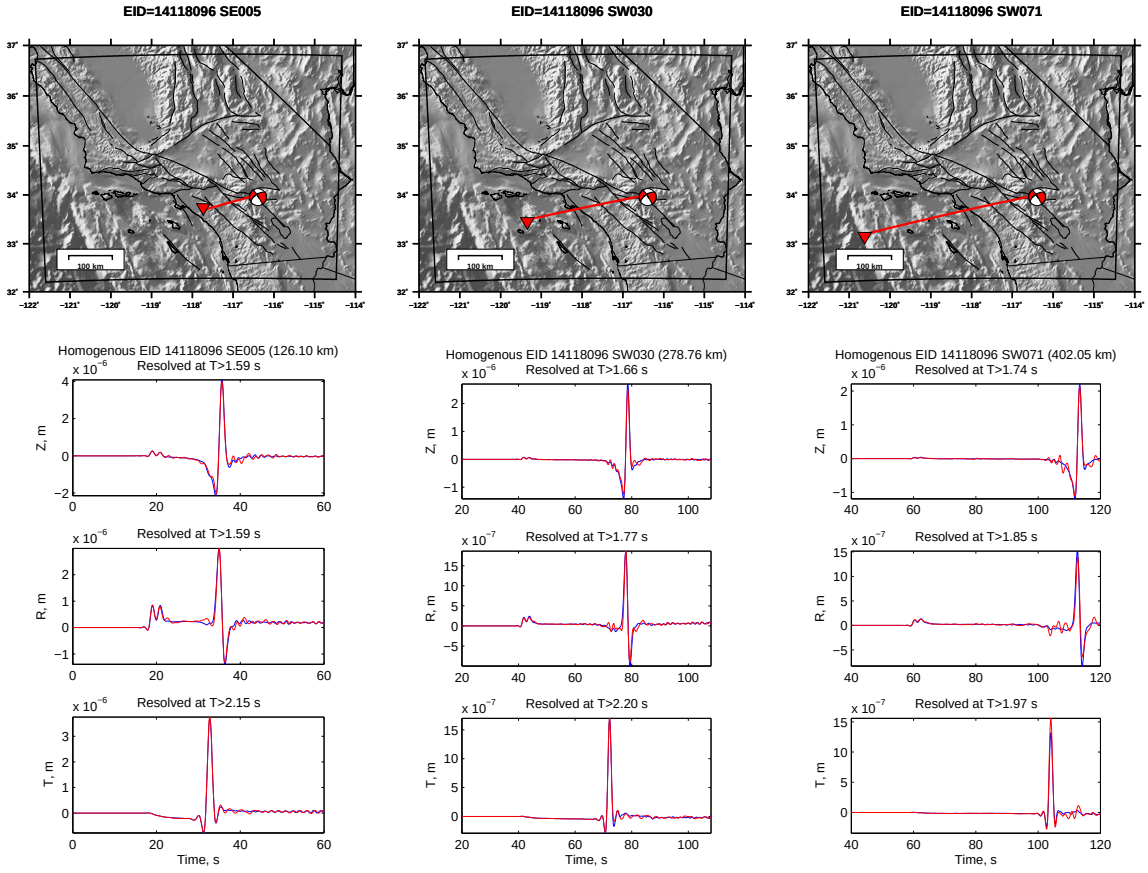

(a) SE005 (b) SW030 (c) SW071

Figure 3.33: Waveforms for source 14118096 propagating southwest in the homogeneous model. Waveform comparison for source 14118096 to three southwest stations in the homogeneous model. The effect is shown for the vertical (top), radial (middle), and transverse (bottom) components. The blue and red waveforms are produced by meshes whose surface is flat or with topography, respectively. Three stations from (a) to (c) show increasing path length toward the continental shelf (Figure 3.12). The difference between the paired waveform is less noticeable in this model compared to the 1D model (Figure 3.34).

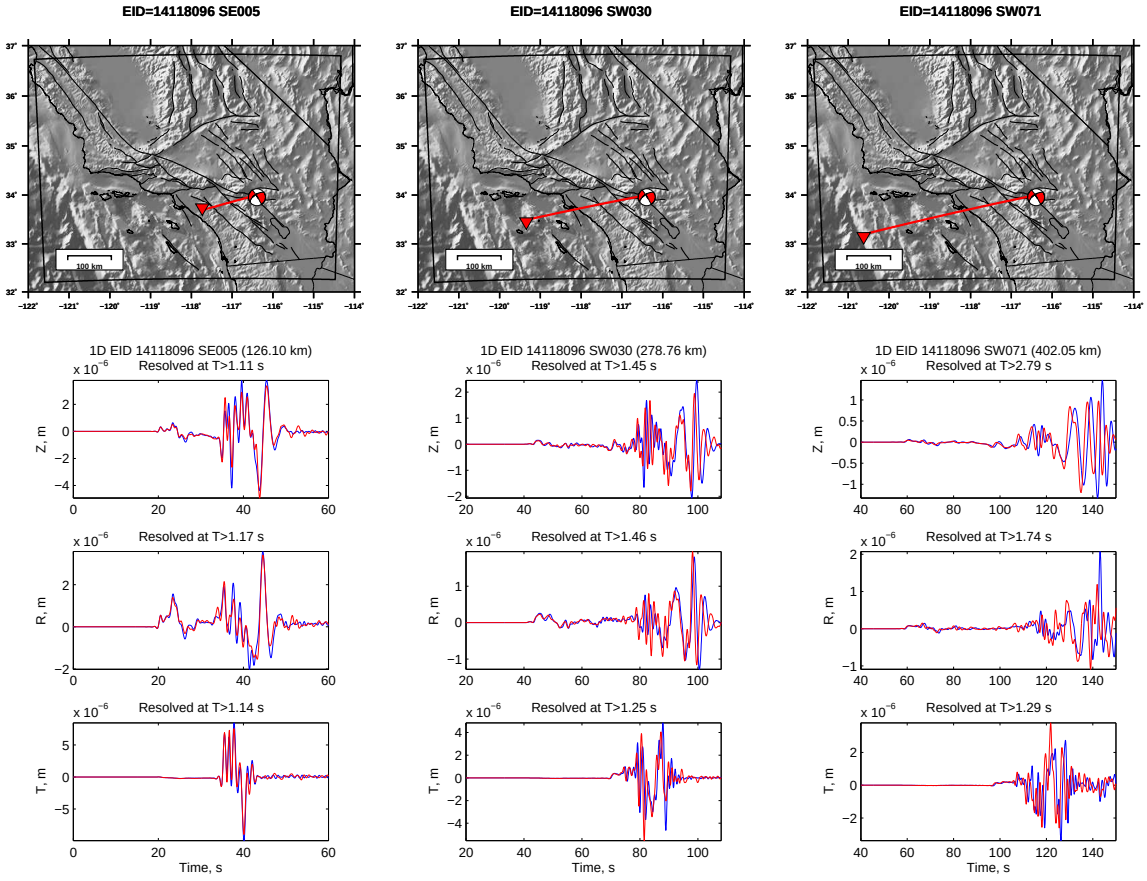

(a) SE005 (b) SW030 (c) SW071

Figure 3.34: Waveforms for path 14118096 propagating southwest in the 1D model.
Same as Figure 3.33, but for the 1D model instead of the homogeneous model. Here the differences are more noticeable.

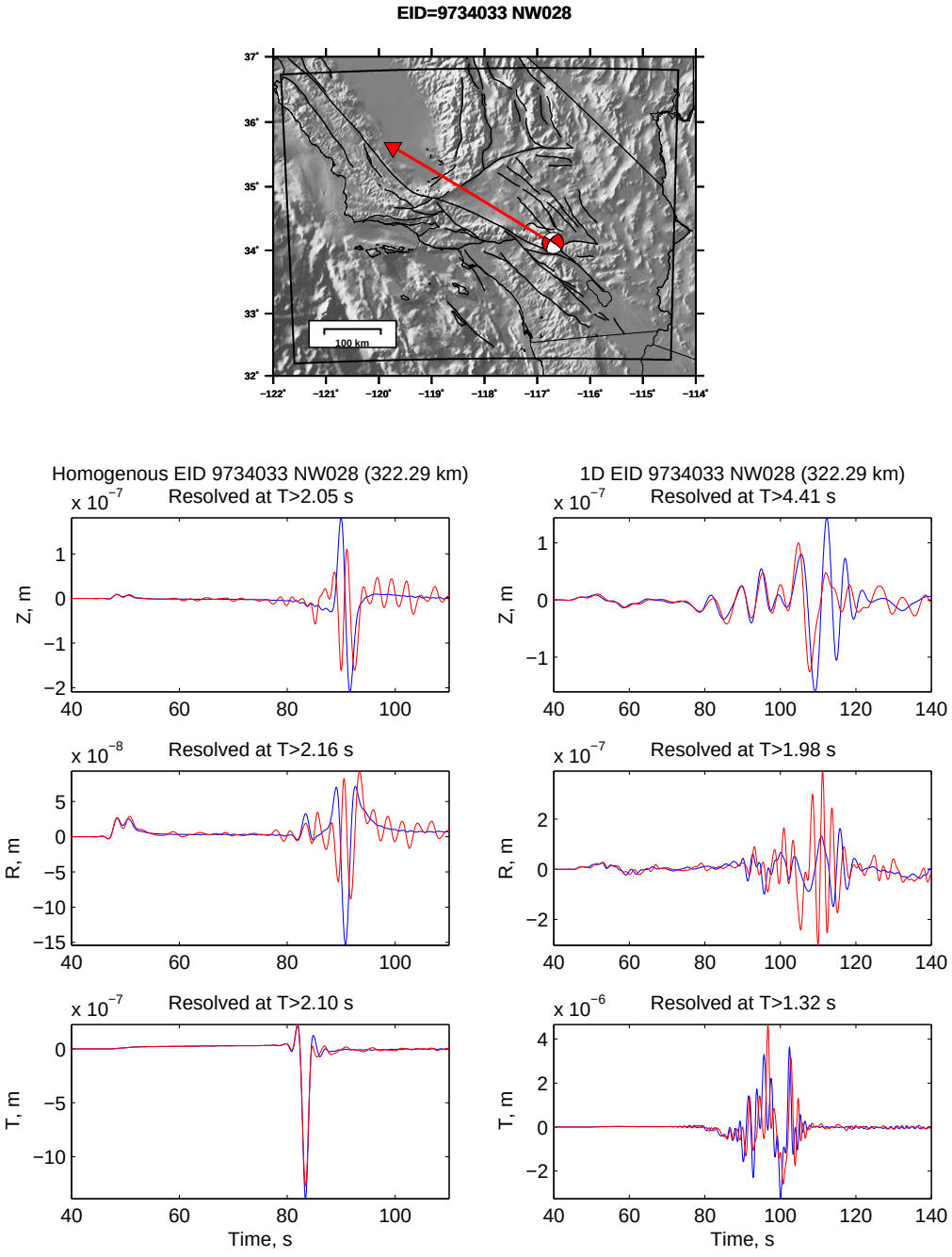

(a) Homogeneous (b) 1D

Figure 3.35: Topographic effects for path 9734033 to NW028.
The effect is shown for the vertical (top), radial (middle), and transverse (bottom) components. The blue and red waveforms are produced by meshes whose surface is flat or with topography, respectively. Strong topographic effects are seen in a path from the San Bernardino mountains to the San Joaquin valley. These are also observed in Figure 3.22 and Figure 3.20.

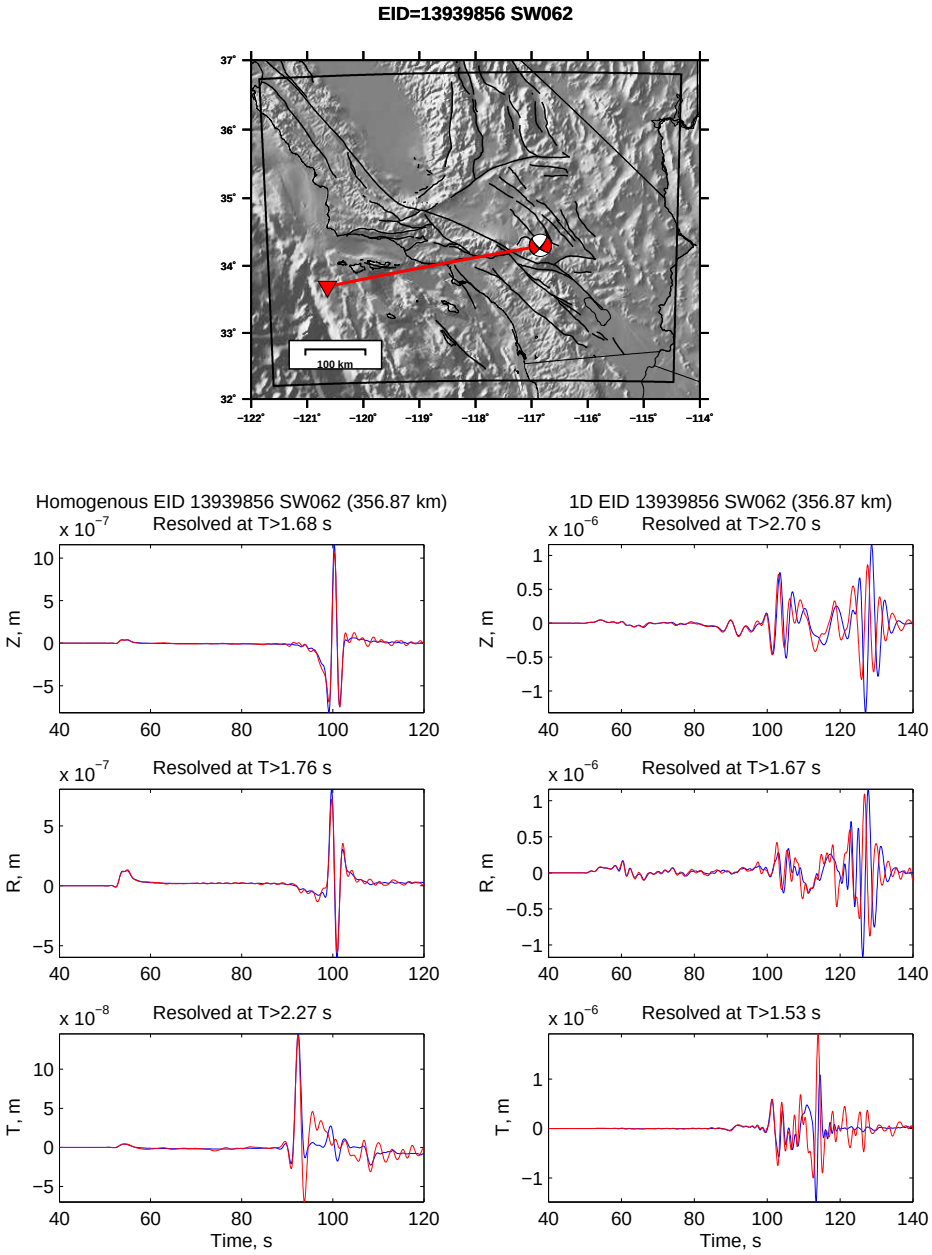

(a) Homogeneous (b) 1D

Figure 3.36: Topographic effects for path 13939856 to SW062.
The effect is shown for the vertical (top), radial (middle), and transverse (bottom) components. The blue and red waveforms are produced by meshes whose surface is flat or with topography, respectively. This path creates a "topographic hot spot" when we quantify the misfit of topographic effects in the transverse component in the homogeneous model (Figure 3.29). This is because the Rayleigh waves propagating to nearby topography may deviate from the direct source-station path.

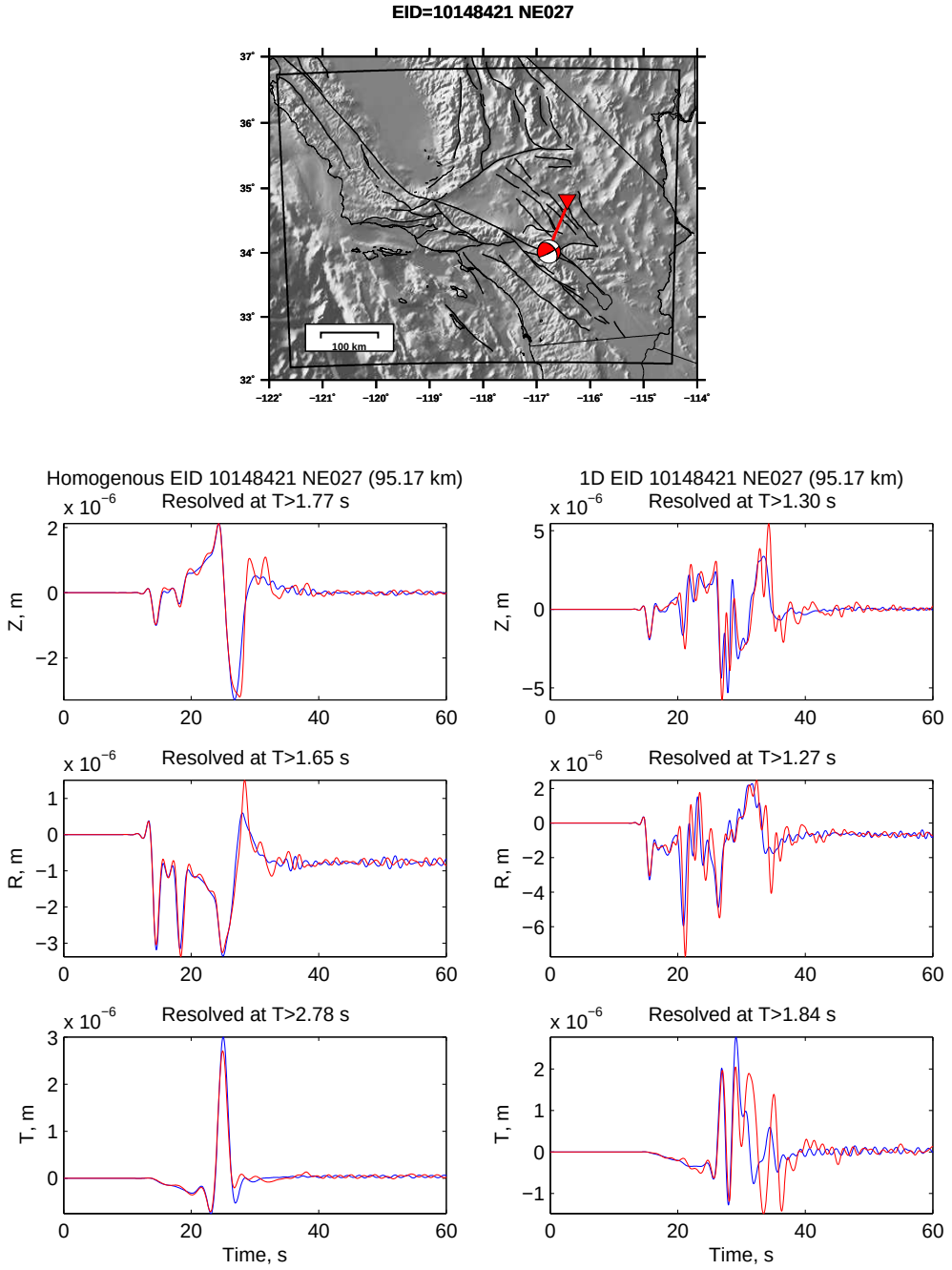

(a) Homogeneous (b) 1D

Figure 3.37: Topographic effects for path 10148421 to NE027.
The effect is shown for the vertical (top), radial (middle), and transverse (bottom) components. The blue and red waveforms are produced by meshes whose surface is flat or with topography, respectively. This path produces strong topographic effects in the 1D model of Figure 3.20. This path shows topographic effects in amplitude and in post-surface-wave coda in the homogeneous model.

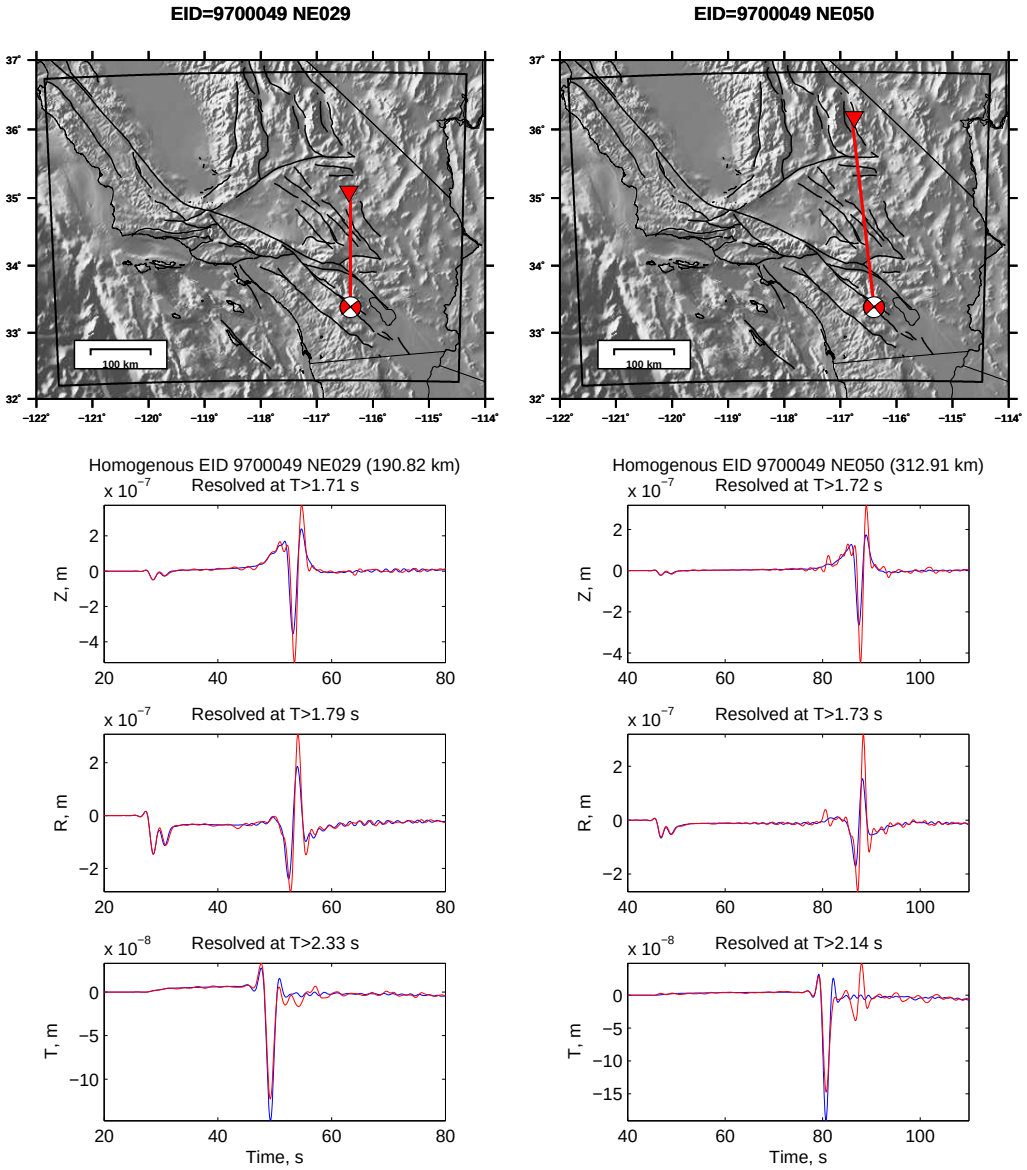

(a) station NE029 (b) station NE050

Figure 3.38: Waveforms for source 9700049 propagating northwest in the homogeneous model. Waveform comparison for source 9700049 to two northwest stations in the homogeneous model. The effect is shown for the vertical (top), radial (middle), and transverse (bottom) components. The blue and red waveforms are produced by meshes whose surface is flat or with topography, respectively. Two stations, (a) and (b), are selected to investigate the accumulated topographic effects in the homogeneous model along a path to the north. We see a Rayleigh wave in the transverse component (b), indicating that the Rayleigh wave has deviated from the direct source-station path, due to the topography. The Rayleigh wave on the vertical and radial components is amplified with increasing distance, due to topography. The comparison in the 1D model is shown in Figure 3.39.

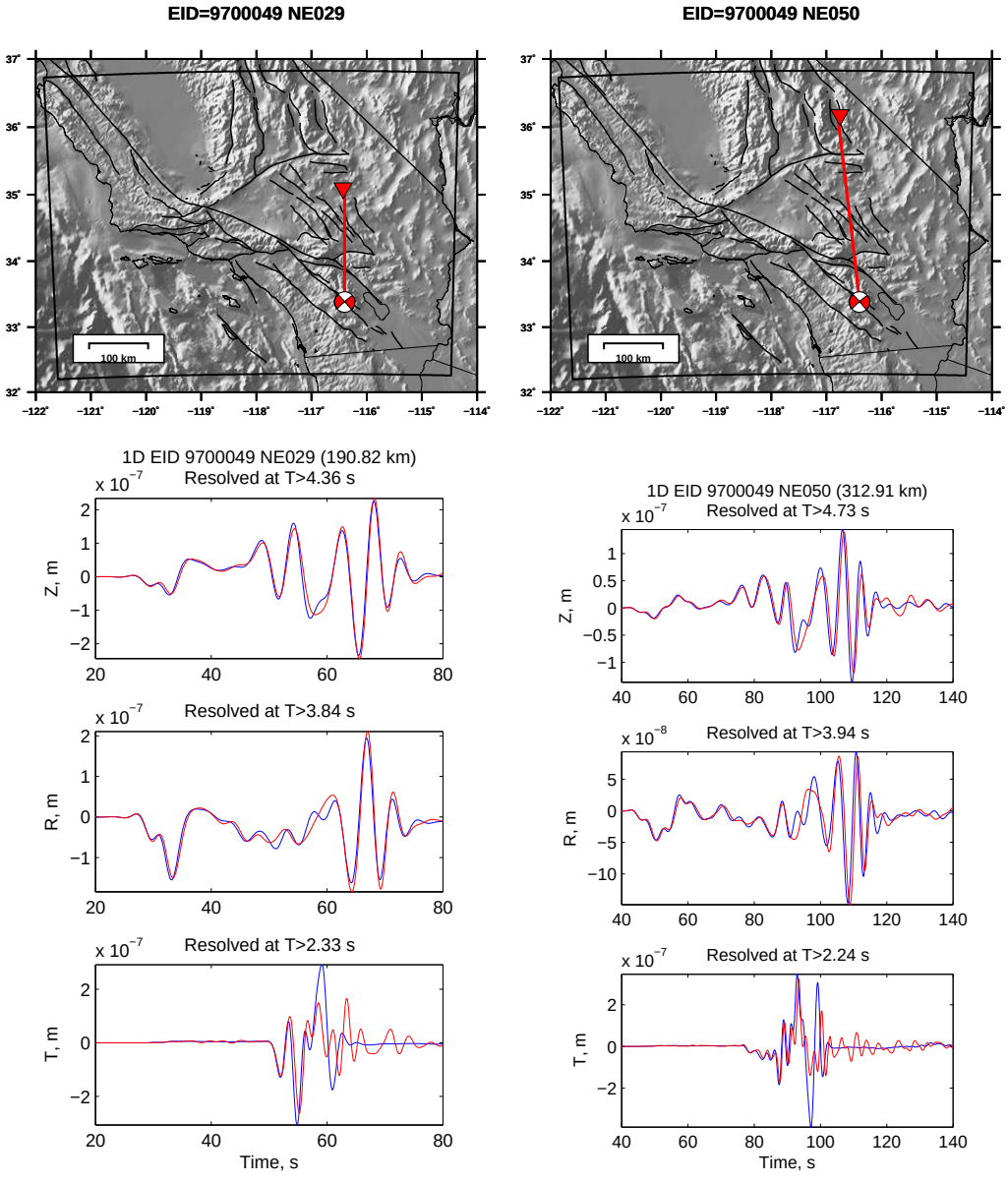

(a) station NE029 (b) station NE050

Figure 3.39: Waveforms for path 9700049 propagating northwest in the 1D model.
Same as Figure 3.38, but for the 1D model instead of the homogeneous model. The topographic effects are strongest for the nodal Love wave on the transverse component.

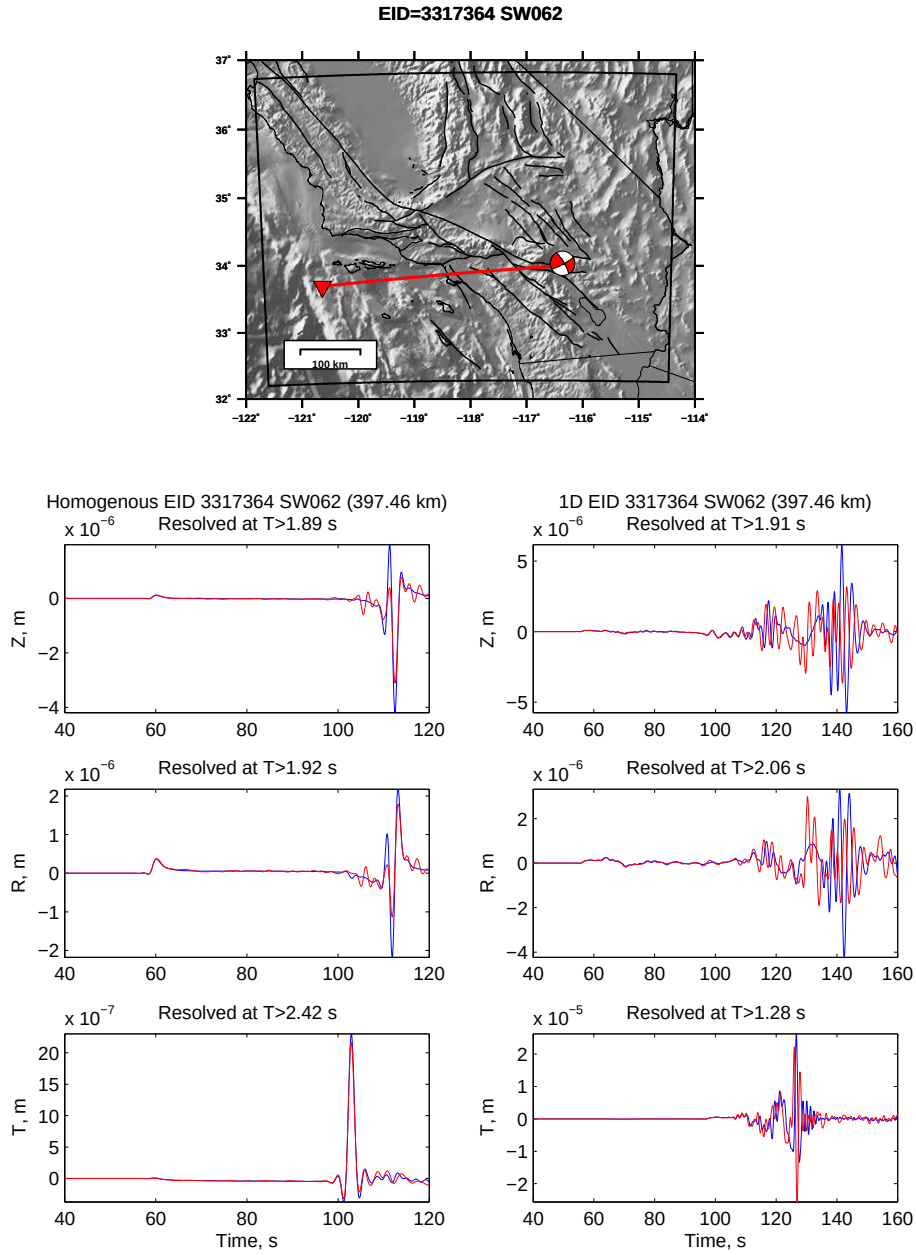

(a) Homogeneous (b) 1D

Figure 3.40: Topographic effects for path 3317364 to SW062.
The effect is shown for the vertical (top), radial (middle), and transverse (bottom) components. The blue and red waveforms are produced by meshes whose surface is flat or with topography, respectively. This is an example for a path with a station oceanward of the continental shelf which produces strong topographic effects in the 1D model of Figure 3.20. There are strong amplitude differences in the vertical and radial components in the 1D model due to the effects of topography. The topographic effects in the homogenous model are less noticeable compared to the 1D model.

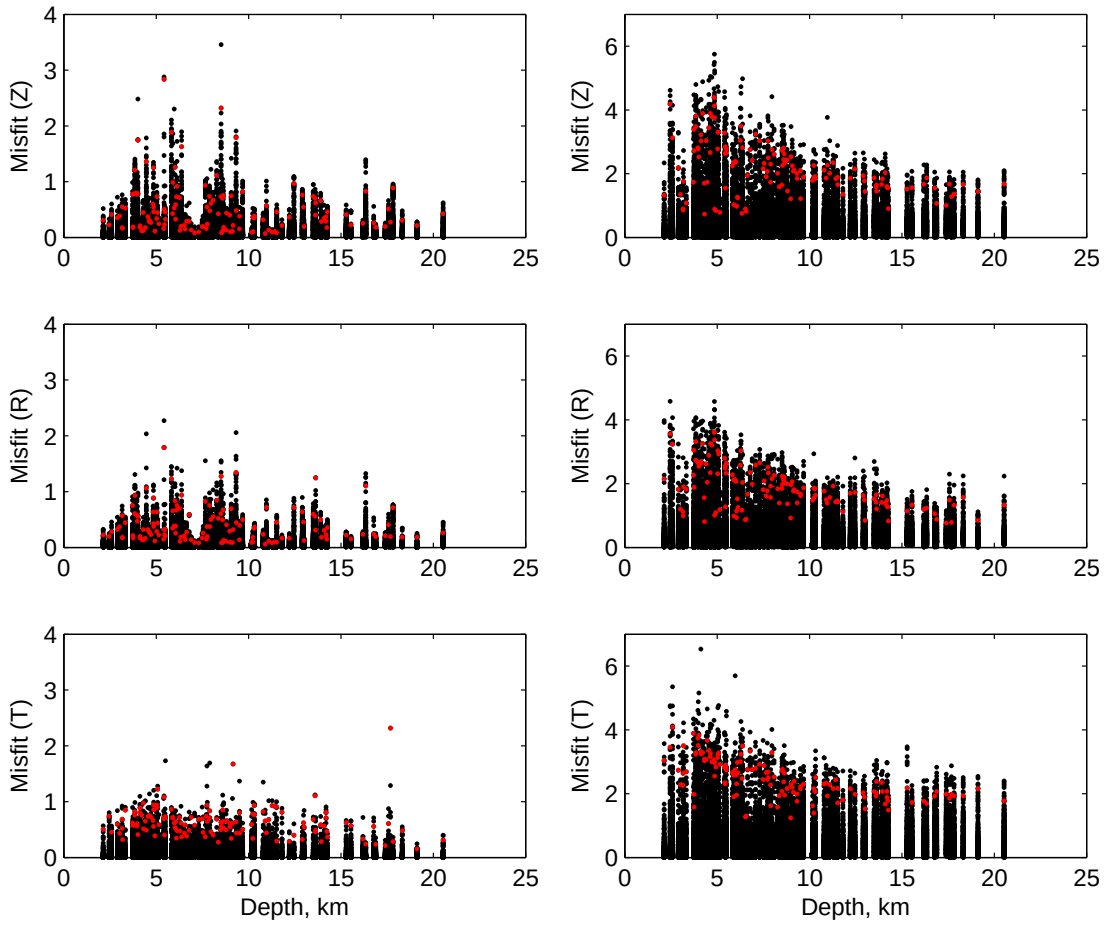

(a) Homogeneous (b) 1D

Figure 3.41: Topographic effects as a function of source depth.
All 43,155 paths are plotted as black dots in each figure for the vertical (top), radial (middle), and transverse (bottom) components. For each of the 137 sources, a red dot is plotted for the 90% cumulative sum (e.g., Figure 3.7) of the topographic effects over all 315 stations. Shallower sources have larger maximum single-station misfit values and larger spread for both the 1D and the homogeneous models for all components. We interpret this to be a result of shallower sources generating stronger surface waves that interact with the topography.

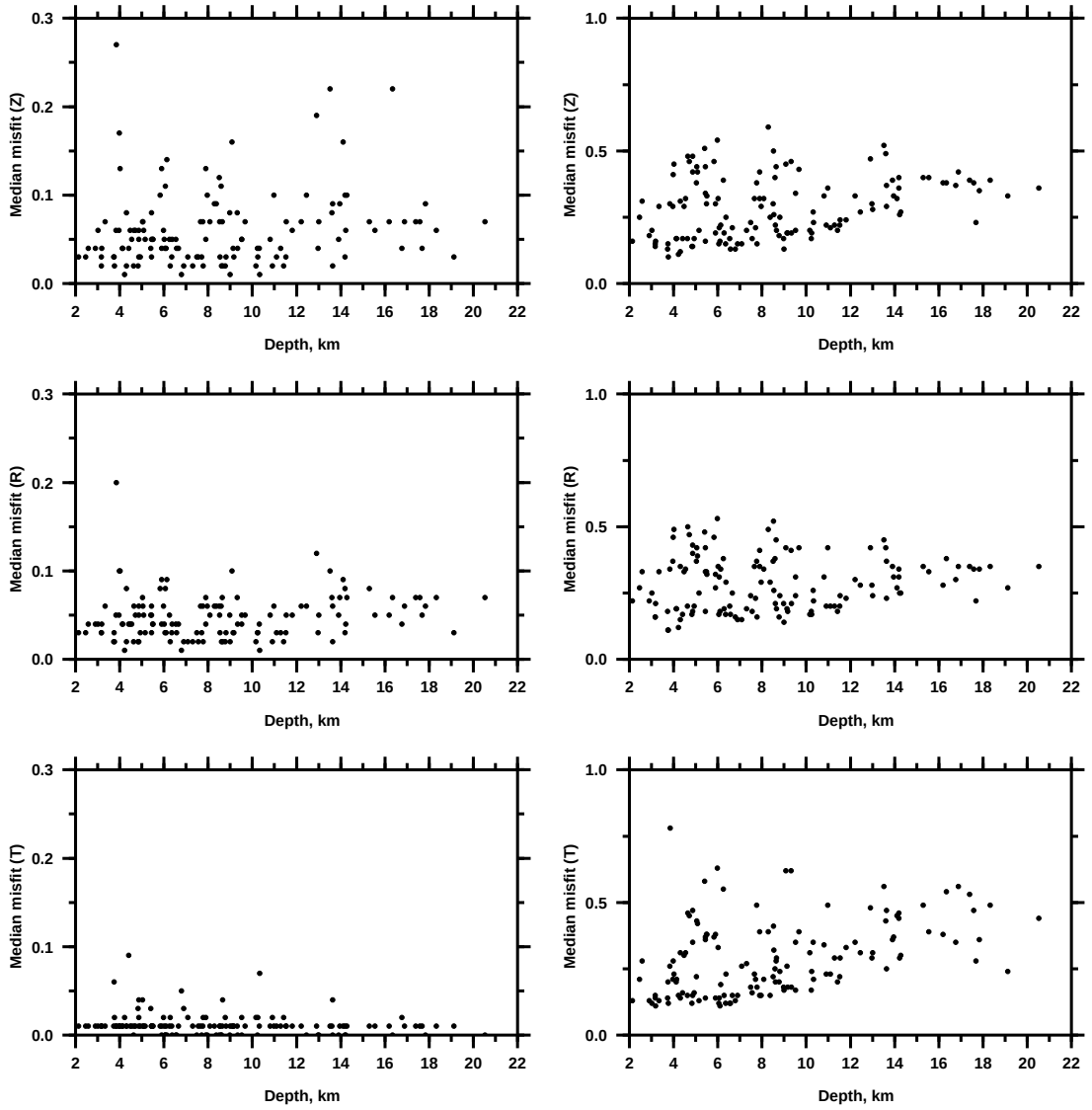

(a) Homogeneous (b) 1D

Figure 3.42: Topographic effects as a function of source depth.
Same as Figure 3.41, but here we compute the median over all stations for each source. Note that the y-axis scale is much smaller than in Figure 3.41, indicating that the topographic effects are generally weak when considering all stations. In the 1D model results, there is a hint of increasing topographic effects with increasing source depth, but further simulations would be needed to investigate this possible relationship.

Chapter 4
Conclusion and future work

4.1 Conclusion

We have conducted a numerical study to investigate the effects of topography on the seismic wavefield at periods of 1 s and longer. This is the period range below which (1) there are large uncertainties in most 3D wave-speed models for the crust and (2) computational cost poses challenges to running a large systematic study (such as this one). Our analysis should be considered in the context of previous studies (*Lee et al.*, 2008; *Rodgers et al.*, 2010; *Köhler et al.*, 2012) that identify much larger effects of topography at shorter periods (higher frequencies). As 3D seismic imaging methods march into the higher frequency realm at industry scales (*Virieux and Operto*, 2009; *Sirgue et al.*, 2010; *Plessix et al.*, 2013) and regional earthquake scales (*Chen et al.*, 2007; *Tape et al.*, 2009a), it will be important to take into account the effects of topography.

The emphasis of our study is on homogeneous and 1D models because at this stage we do not want the added complexity of 3D wave-speed structures on our synthetic seismograms. Nevertheless, the technique we use—the spectral element method within the code SPECFEM3D (*Komatitsch and Tromp*, 1999; *Komatitsch et al.*, 2004)—will compute synthetic seismograms in the same manner as we have done here and discussed in Chapter 2: identify a wave-speed model, compute a hexahedral mesh using GEOCUBIT (*Casarotti et al.*, 2008), then perform wavefield simulations in models with a flat surface or with realistic topography.

Here we summarize our key points based on the results presented in Chapter 3:

1. As demonstrated in previous studies (e.g., *Ma et al.*, 2007; *Lee et al.*, 2008, 2009), we see that the effects of topography are generally weak but can be pronounced in certain circumstances. In waveform modeling of source or structure effects, the details—small-scale effects such as topography—matter in interpretation.

   This study confirms that interference between incident waves and topography creates a significant difference on the surface waves compared to the body waves (*Ma et al.*, 2007) (Figure 3.2).

2. The strongest effects of topography on seismic waveforms occur for source-station paths that are approximately nodal for the seismic radiation. In these directions, the wavefield is relatively low amplitude and prone to the influences of scattering from nearby topography or multipathing (in the 1D model) due to non-great-circle wave propagation. The source maps, which show the topographic effects at all stations for one source, reveal systematic patterns which are dominated by the source effect (Figures 3.12, 3.16, 3.19). Even though the source effect is dominant, it is also clear that the topography breaks some of the symmetry

of the source pattern in both the homogeneous and 1D models (e.g., Figures 3.11, 3.15)

3. The station maps, which show the topographic effects at all sources for one station, minimize the effect of the source by combining paths from all 137 sources into the same representation. Any systematic patterns in these maps can be attributed to topographic effects that are *not* resulting from source effects (such as nodal paths). We identify topographic 'hotspot' regions in California within the Sierra Nevada and the San Bernardino mountains (Figures 3.22–3.25). Even though the source parameters vary for earthquakes in these regions, the strong topographic effects persist toward certain stations. We can think of these as 'regional' path-specific effects, whereby any source in a particular region will impart topographic effects in certain directions.

4. The source map with 90% of the cumulative sum of the quantification of topography misfit over all 315 stations (Figure 3.8) provides clear patterns with length scales smaller than $\sim$50 km. However, it also reveals very strong differences between sources right next to each other, implying that source depth or mechanism is more important than the topography in the source region.

5. The station map with 90% of the cumulative sum of the quantification of topography misfit over all 137 sources shows moderate topographic effects in the San Joaquin valley, large systematic differences west of the oceanward side of the continental shelf, and less topographic effects in the Mojave desert. These effects are noticeable in amplitude and post surface wave coda for the homogeneous model and with addition of phase difference for the 1D model (Figure 3.20).

6. The homogeneous and 1D models provide complementary views of the topographic effects. In the homogeneous case, there are no Love waves and no dispersion, so the wavefield is simpler but also unrealistic. The wave-speed structure along any path is identical, so all differences (small as they may be) in the waveforms can be attributed exclusively to the topography.

   The 1D model generates Love waves and dispersive waves and therefore produces seismograms that are more realistic. However by imposing topographic variations on the 1D model, we change the thickness of the uppermost layer (Table 2.1). Therefore our seismograms include the effects of topography as well as the effects of changes in the wave-speed structure along each path.

7. Generally, topographic effects decay with increasing cut-off period when the waveforms are

low-pass filtered. This, however, depends on the misfit function and is only relevant for periods that are numerically resolved (Figure 3.4).

8. The topographic effects generally increase with distance but it is also shown that this is not always true at some specific stations (Figure 3.26).

9. Between the three components, the vertical and radial components are more sensitive to topography than the transverse component confirming previous studies (*Geli et al.*, 1988; *Bard*, 1982) (Figure 3.6).

10. Shallower sources have a larger maximum single-station effect and larger spread for both 1D and homogeneous models for all components. The relationship between topographic effects and source depth is inconclusive (Figure 3.41).

11. Shortest resolvable period tests (Chapter 2) are critical for quantifying the topographic effects, since one must first know the shortest period above which the synthetic seismograms are numerically accurate, prior to quantifying the effects of topography. This does not seem to be standard practice within simulation-based studies of topography (Table 1.1).

4.2 Future work

This study identifies several challenges associated with quantifying the effects of topography. Despite the efforts of numerous studies (Table 1.1)—most of them based on synthetic seismograms—there remains no direct way to separate the topographic effects from observed seismic waveforms. We conclude with possible directions for building upon the results of our study.

1. The choice of misfit function is an important step in any problem. We chose a direct waveform difference of the full-length seismogram (Eq. 2.5), but alternative misfit analyses could be conducted without any additional simulations. In particular, measurements that calculate differences over different frequency ranges and different time windows could help distinguish the topographic effects due to scattering (amplitude differences) versus path deviations (phase differences) (*Tromp et al.*, 2005; *Kristeková et al.*, 2006). Or the misfit analysis could be performed on amplitude and phase spectra (e.g., Figure 3.3), rather than on time series.

2. One could perform systematic simulations to investigate how earthquakes—notably the moment tensor orientation and the depth (*Lee et al.*, 2009) —influence the topographic effects. By using a relatively large set of 137 earthquakes, we can make generalizations, but these points could be strengthened with a well-designed numerical experiment.

3. The addition of realistic errors to our synthetic seismograms would provide an additional step toward comparisons with real data. However, this would minimize the role of nodal stations, which will tend to be below the noise level. Including realistic errors would probably require a misfit function such as Equation (2.4) that does not involve relative amplitudes.

4. The regional earthquake wavefield at periods 1 s and longer is dominated by surface waves. The teleseismic wavefield is routinely used to infer variations in crustal properties. A systematic study similar to ours could be performed using a range of incident plane waves, rather than a set of different earthquakes, in order to quantify the effects of topography on the teleseismic wavefield (*Tong et al.*, 2014). Or, at shorter length scales, it would be interesting to evaluate the effects of topography on industry scale problems (*Bleibinhaus and Rondenay*, 2009).

5. The question remains: What specific waveforms in real seismograms arise from topographic effects? To bridge the gap from our study to real data, one would naturally consider synthetic seismograms in a 3D wave-speed model. However, it is unclear how to modify a 3D wave-speed model with topography to represent a 3D wave-speed model without topography. Two approaches have been used. One is a method to flatten a 3D wave-speed model by demolishing or "bulldozing" all features above zero elevation (*Ma et al.*, 2007). But this might create ambiguity to define whether the perturbations in waveforms are coming from topography or from wave-speed differences due to the different paths. Another approach is by pushing or pulling the wave-speed model from above and below zero elevation respectfully towards a flat surface (*Aagaard et al.*, 2008). In this case, a surface wave might "see" a similar depth profile along each path; yet body waves could have identical paths but with different velocity structures along them.

   Synthetic simulations with complex wave-speed models show that topography matters. We advocate taking into account the topography, since it is one less effect to worry about when interpreting 3D synthetic seismograms in comparison with observed waveforms.

References

Aagaard, B. T., et al. (2008), Ground-motion modeling of the 1906 San Francisco earthquake, part II: Gound-motion estimates for the 1906 earthquake and scenario events, *Bull. Seis. Soc. Am.*, *98*(2), 1012–1046.

Amante, C., and B. W. Eakins (2009), ETOPO1 1 Arc-Minute Global Relief Model: Procedures, Data Sources and Analysis, NOAA Technical Memorandum NESDIS NGDC-24, 19 pp.

Anderson, J. G. (2004), Quantitative measure of the goodness-of-fit of synthetic seismograms, 13th World Conference on Earthquake Engineering, Vancouver, B.C., Canada, August 1–6, 2004, Paper No. 243, 14 pp.

Bard, P.-Y. (1982), Diffracted waves and displacement field over two-dimensional elevated topographies, *Geophys. J. Int.*, *71*(3), 731–760.

Bielak, J., et al. (2009), The ShakeOut earthquake scenario: Verification of three simulation sets, *Geophys. J. Int.*, *180*, 375–404.

Bleibinhaus, F., and S. Rondenay (2009), Effects of surface scattering in full-waveform inversion, *Geophysics*, *74*(6), WCC69–WCC77.

Brossier, R., J. Virieux, and S. Operto (2008), Parsimonious finite-volume frequency-domain method for 2-DP–SV-wave modelling, *Geophys. J. Int.*, *175*(2), 541–559.

Carcione, J. M. (1994), The wave equation in generalized coordinates, *Geophysics*, *59*(12), 1911–1919.

Carrington, L., D. Komatitsch, M. Laurenzano, M. M. Tikir, D. Michéa, N. Le Goff, A. Snavely, and J. Tromp (2008), High-frequency simulations of global seismic wave propagation using SPECFEM3D_GLOBE on 62K processors, in *International Conference for High Performance Computing, Storage, and Analysis (SC 2008)*, IEEE, doi:10.1109/SC.2008.5215501.

Casarotti, E., M. Stupazzini, S. J. Lee, D. Komatitsch, A. Piersanti, and J. Tromp (2008), CUBIT and seismic wave propagation based upon the spectral-element method: An advanced unstructured mesher for complex 3D geological media, in *Proceedings of the 16th International Meshing Roundtable*, edited by M. L. Brewer and D. Marcum, pp. 579–597, Springer, Berlin.

Chaljub, E., P. Moczo, S. Tsuno, P.-Y. Bard, J. Kristek, M. Käser, M. Stupazzini, and M. Kristekova (2010), Quantitative comparison of four numerical predictions of 3D ground motion in the Grenoble Valley, France, *Bull. Seis. Soc. Am.*, *100*(4), 1427–1455.

Chen, P., L. Zhao, and T. H. Jordan (2007), Full 3D tomography for the crustal structure of the Los Angeles region, *Bull. Seis. Soc. Am.*, *97*(4), 1094–1120.

Dumbser, M., and M. Käser (2006), An arbitrary high-order discontinuous Galerkin method for elastic waves on unstructured meshes-II. The three-dimensional isotropic case, *Geophys. J. Int.*, *167*(1), 319–336.

Dunham, E. M., D. Belanger, L. Cong, and J. E. Kozdon (2011), Earthquake ruptures with strongly rate-weakening friction and off-fault plasticity, part 2: Nonplanar faults, *Bull. Seis. Soc. Am.*, *101*(5), 2308–2322.

Dziewonski, A., T.-A. Chou, and J. H. Woodhouse (1981), Determination of earthquake source parameters from waveform data for studies of global and regional seismicity, *J. Geophys. Res.*, *86*(B4), 2825–2852.

Frankel, A., and R. W. Clayton (1986), Finite difference simulations of seismic scattering: Implications for the propagation of short-period seismic waves in the crust and models of crustal heterogeneity, *J. Geophys. Res.*, *91*(B6), 6465–6489.

Gagnon, J.-S., S. Lovejoy, and D. Schertzer (2006), Multifractal earth topography, *Nonlinear Processes in Geophysics*, *13*(5), 541–570.

Geli, L., P.-Y. Bard, and B. Jullien (1988), The effect of topography on earthquake ground motion: a review and new results, *Bull. Seis. Soc. Am.*, *78*(1), 42–63.

Guidotti, R., M. Stupazzini, C. Smerzini, R. Paolucci, and P. Ramieri (2011), Numerical study on the role of basin geometry and kinematic seismic source in 3D ground motion simulation of the 22 February 2011 Mw 6.2 Christchurch earthquake, *Seis. Res. Lett.*, *82*(6), 767–782.

Hartzell, S. H., D. L. Carver, and K. W. King (1994), Initial investigation of site and topographic effects at Robinwood Ridge, California, *Bull. Seis. Soc. Am.*, *84*(5), 1336–1349.

Jennings, C. W. (1994), Fault activity map of California and adjacent areas, with locations and ages of recent volcanic eruptions, Calif. Div. Mines and Geology, Geologic Data Map No. 6, map scale 1:750,000.

Köhler, A., C. Weidle, and V. Maupin (2012), On the effect of topography on surface wave propagation in the ambient noise frequency range, *J. Seis.*, *16*(2), 221–231.

Komatitsch, D., and J. Tromp (1999), Introduction to the spectral element method for three-dimensional seismic wave propagation, *Geophys. J. Int.*, *139*, 806–822.

Komatitsch, D., J. Ritsema, and J. Tromp (2002), The spectral-element method, Beowulf computing, and global seismology, *Science*, *298*, 1737–1742.

Komatitsch, D., Q. Liu, J. Tromp, P. Süss, C. Stidham, and J. H. Shaw (2004), Simulations of ground motion in the Los Angeles basin based upon the spectral-element method, *Bull. Seis. Soc. Am.*, *94*(1), 187–206.

Kristeková, M., J. Kristek, P. Moczo, and S. M. Day (2006), Misfit criteria for quantitative comparison of seismograms, *Bull. Seis. Soc. Am.*, *96*(5), 1836–1850.

Latychev, K., J. X. Mitrovica, J. Tromp, M. E. Tamisiea, D. Komatitsch, and C. C. Christara (2005), Glacial isostatic adjustment on 3-D Earth models: A finite-volume formulation, *Geophys. J. Int.*, *161*(2), 421–444.

Lee, S.-J., H.-W. Chen, Q. Liu, D. Komatitsch, B.-S. Huang, and J. Tromp (2008), Three-dimensional simulations of seismic-wave propagation in the Taipei basin with realistic topography based upon the spectral-element method, *Bull. Seis. Soc. Am.*, *98*(1), 253–264.

Lee, S.-J., D. Komatitsch, B.-S. Huang, and J. Tromp (2009), Effects of topography on seismic-wave propagation: An example from northern Taiwan, *Bull. Seis. Soc. Am.*, *99*(1), 314–325.

Lee, S.-J., Q. Liu, J. Tromp, D. Komatitsch, W.-T. Liang, and B.-S. Huang (2014), Toward real-time regional earthquake simulation II: Real-time online earthquake simulation (ROS) of Taiwan earthquakes, *J. Asian Earth Sci.*, *87*, 56–68.

Ma, S., R. J. Archuleta, and M. T. Page (2007), Effects of large-scale surface topography on ground motions, as demonstrated by a study of the San Gabriel Mountains, Los Angeles, California, *Bull. Seis. Soc. Am.*, *97*(6), 2066–2079.

Magnoni, F., E. Casarotti, A. Michelini, A. Piersanti, D. Komatitsch, D. Peter, and J. Tromp (2014), Spectral-element simulations of seismic waves generated by the 2009 LÁquila earthquake, *Bull. Seis. Soc. Am.*, *104*(1), 73–94.

Mandelbrot, B. B., and J. R. Wallis (1969), Computer experiments with fractional Gaussian noises: Part 1, averages and variances, *Water Resources Research*, *5*(1), 228–241, doi: 10.1029/WR005i001p00228.

Martin, R., D. Komatitsch, C. Blitz, and N. Le Goff (2008), Simulation of seismic wave propagation in an asteroid based upon an unstructured MPI spectral-element method: Blocking and non-blocking communication strategies, *Lecture Notes in Computer Science*, *5336*, 350–363.

Pelletier, J., and D. Turcotte (1996), Scale-invariant topography and porosity variations in fluvial sedimentary basins, *J. Geophys. Res.*, *101*(B12), 28,165–28,175.

Peter, D., et al. (2011), Forward and adjoint simulations of seismic wave propagation on fully unstructured hexahedral meshes, *Geophys. J. Int.*, *186*, 721–739.

Pickering, G., J. M. Bull, D. J. Sanderson, and P. V. Harrison (1994), Fractal fault displacements: a case study from the moray firth, scotland, in *Fractals and Dynamic Systems in Geoscience*, pp. 105–119, Springer.

Pickering, G., J. Bull, and D. Sanderson (1999), Fault populations and their relationship to the scaling of surface roughness, *J. Geophys. Res.*, *104*(B2), 2691–2701.

Plessix, R. E., P. Milcik, H. Rynja, A. Stopin, K. Matson, and S. Abri (2013), Multiparameter full-waveform inversion: Marine and land examples, *Leading Edge*, *32*(9), 1030–1038.

Pyrak-Nolte, L. J., L. R. Myer, and N. G. Cook (1990), Transmission of seismic waves across single natural fractures, *J. Geophys. Res.*, *95*(B6), 8617–8638.

Rodgers, A. J., N. A. Petersson, and B. Sjogreen (2010), Simulation of topographic effects on seismic waves from shallow explosions near the North Korean nuclear test site with emphasis on shear wave generation, *J. Geophys. Res.*, *115*(B11).

Shearer, P. M. (2009), *Introduction to Seismology*, 2 ed., Cambridge U. Press, Cambridge, UK.

Sirgue, L., O. I. Barkved, J. Dellinger, J. Etgen, U. Albertin, and J. H. Kommedal (2010), Full waveform inversion: the next leap forward in imaging at Valhall, *First Break*, *28*(4), 65–70.

Stupazzini, M., R. Paolucci, and H. Igel (2009), Near-fault earthquake ground-motion simulation in the Grenoble Valley by a high-performance spectral element code, *Bull. Seis. Soc. Am.*, *99*(1), 286–301.

Tang, C., and P. Bak (1988), Critical exponents and scaling relations for self-organized critical phenomena, *Physical Review Letters*, *60*(23), 2347.

Tape, C., Q. Liu, A. Maggi, and J. Tromp (2009a), Adjoint tomography of the southern California crust, *Science*, *325*, 988–992.

Tape, C., Q. Liu, A. Maggi, and J. Tromp (2009b), Seismic tomography and imaging of the southern California crust, in *2009 Southern California Earthquake Center Annual Meeting, Proceedings and Abstracts*, vol. 19, p. 188.

Tape, C., Q. Liu, A. Maggi, and J. Tromp (2010), Seismic tomography of the southern California crust based on spectral-element and adjoint methods, *Geophys. J. Int.*, *180*, 433–462.

Tong, P., C.-w. Chen, D. Komatitsch, P. Basini, and Q. Liu (2014), High-resolution seismic array imaging based on an SEM-FK hybrid method, *Geophys. J. Int.*, *197*(1), 369–395.

Tromp, J., C. Tape, and Q. Liu (2005), Seismic tomography, adjoint methods, time reversal, and banana-doughnut kernels, *Geophys. J. Int.*, *160*, 195–216.

Virieux, J., and S. Operto (2009), An overview of full-waveform inversion in exploration geophysics, *Geophysics*, *74*(6), WCC1–WCC26.

Wessel, P., and W. H. F. Smith (1991), Free software helps map and display data, *Eos Trans. Am. Geophys. Un.*, *72*(41), 441 ff.

Appendix A
Supplemental Information

A.1 Topographic scale of southern California

Spectral analysis is one of the most common methods to analyze the scaling properties of a topography (*Pelletier and Turcotte*, 1996; *Pickering et al.*, 1999; *Gagnon et al.*, 2006). First, we quantify the characteristics of the topography in southern California by taking a Fourier Transform of topographic profiles (Figures A.1 and A.2). From computing the mean of all profiles in each direction (x and y), we can observe that the largest elevation corresponds to small wavenumber and the smallest elevation to large wavenumber in a power law manner. When we plot them in log/log scale, the elevation linearly decreases with increasing wavenumber. This is expected because spectral amplitudes of fractal geometry of a variety of natural process are power function of wave number (*Mandelbrot and Wallis*, 1969; *Tang and Bak*, 1988; *Pickering et al.*, 1994; *Pelletier and Turcotte*, 1996; *Gagnon et al.*, 2006). The large amplitudes in the spectra for $k < 5.10^{-5}$ m^{-1} or $\log_{10} k < -4.3$ m^{-1} may be related to the gradual change in topography that occurs at the oceanward of the continental shelf in the southwest region of our model. We estimate a best-fitting line from the average of all profiles for each direction. The line in Figure A.1 is given by

$$\log_{10} A = m \, . \, \left(\log_{10} k\right) + b \tag{A.1}$$

where both m_x and $m_y = -1.15$ m^3 for the profiles in the x and y-direction respectively.

A.2 Amplitude spectra for selected seismograms

We present comparisons of amplitude spectra for seismograms produced in models with and without topography. One example was shown in Figure 3.3; Figures A.7–A.13 show examples for the time series presented in Chapter 3.

A.3 List of sources and stations

We present two tables that summarizes the sources and stations used in this study. The sources are a subset of earthquakes previously used in (*Tape et al.*, 2009a).

Table A.1: List of earthquake sources used in the study. The sources are a subset from (*Tape et al.*, 2009a). Each is listed as a moment tensors, which is a mathematical representation of the fault mechanism. The majority of the moment tensors here are double couples. The basis chosen is the GCMT (*Dziewonski et al.*, 1981) convention of up (r), south (θ), east (ϕ); the units are N-m.

EID	Lon (deg)	Lat (deg)	Depth (km)	M_{rr} (N-m)	$M_{\theta\theta}$ (N-m)	$M_{\phi\phi}$ (N-m)	$M_{r\theta}$ (N-m)	$M_{r\phi}$ (N-m)	$M_{\theta\phi}$ (N-m)
3298292	-117.22	34.04	16.19	-1.84e+15	8.55e+14	9.81e+14	1.48e+15	7.63e+14	1.02e+15
3317364	-116.36	34.04	4.01	6.44e+13	-1.53e+15	1.47e+15	1.76e+14	3.07e+14	8.98e+14
3320736	-116.25	34.44	7.96	8.16e+15	4.53e+16	-5.34e+16	-3.98e+16	2.43e+15	7.80e+16
3320884	-116.40	34.86	6.35	-9.38e+14	-2.38e+15	3.32e+15	2.93e+15	5.72e+14	3.20e+15
3320940	-116.39	34.87	3.16	-2.35e+14	-1.15e+14	3.50e+14	2.65e+14	-1.52e+14	4.60e+14
3320951	-116.39	34.83	4.31	-9.65e+13	-1.51e+13	1.12e+14	1.20e+14	-8.36e+13	2.61e+14
3320954	-116.39	34.86	3.16	4.35e+14	2.45e+13	-4.60e+14	4.08e+14	1.96e+14	6.27e+14
3321426	-116.29	34.80	6.06	3.30e+12	2.42e+14	-2.46e+14	-3.02e+13	-1.67e+13	2.61e+14
3321590	-116.40	34.87	3.33	-3.22e+14	-1.19e+16	1.22e+16	5.12e+15	1.49e+15	1.28e+16
3324595	-116.26	34.61	3.75	2.66e+14	-5.71e+13	-2.09e+14	1.35e+12	1.14e+13	1.10e+14
7112721	-116.92	34.12	5.40	7.87e+14	-2.43e+15	1.64e+15	-4.81e+14	-1.23e+15	-1.12e+14
7177729	-116.37	34.80	5.44	-1.14e+14	3.97e+14	-2.82e+14	5.11e+14	-1.88e+14	5.72e+14
9038699	-117.72	33.95	12.98	1.21e+14	-7.74e+14	6.53e+14	2.42e+14	4.29e+14	-1.87e+14
9064093	-116.92	34.12	5.98	-1.01e+10	-4.11e+15	4.11e+15	-2.11e+15	-1.97e+15	2.87e+14
9064568	-117.65	34.37	9.51	1.70e+15	-1.53e+15	-1.68e+14	-5.29e+14	1.56e+14	5.07e+14
9069997	-116.84	34.32	6.02	-7.27e+14	-4.29e+15	5.02e+15	-1.77e+15	1.79e+14	3.90e+13
9070083	-116.85	34.32	5.48	-8.49e+13	-5.16e+14	6.01e+14	-2.34e+14	-4.47e+13	1.62e+14
9085734	-116.37	34.07	2.58	-5.59e+13	-1.33e+14	1.89e+14	-8.65e+13	1.28e+14	2.20e+14
9086693	-116.36	34.04	3.98	-1.94e+13	-8.35e+14	8.54e+14	1.74e+14	7.77e+13	2.21e+14
9093975	-118.23	34.01	6.29	2.14e+14	-1.63e+14	-5.10e+13	1.15e+14	4.11e+13	1.37e+14
9094270	-118.31	35.09	7.71	8.65e+13	-2.69e+14	1.83e+14	1.53e+13	1.57e+14	-1.38e+14
9095528	-118.47	35.74	5.03	-2.19e+15	2.17e+13	2.17e+15	-8.41e+14	6.96e+14	-6.40e+14
9096656	-116.71	33.64	13.60	3.34e+14	-6.17e+14	2.83e+14	-1.08e+14	3.19e+14	1.73e+13
9096972	-118.61	34.39	8.78	3.09e+14	-1.83e+14	-1.27e+14	-1.70e+14	-2.17e+13	2.00e+14
9105672	-116.84	34.32	5.89	-8.19e+13	-4.50e+14	5.32e+14	-2.22e+14	-5.11e+13	1.52e+14
9109131	-116.31	34.69	3.72	-3.21e+14	-3.58e+14	6.79e+14	4.18e+14	-1.14e+14	5.14e+14
9109254	-116.25	34.42	6.79	1.11e+15	-2.22e+15	1.12e+15	1.46e+15	-5.77e+15	3.35e+15
9109287	-116.30	34.71	6.65	-2.22e+14	-4.60e+13	2.68e+14	-5.71e+14	1.44e+14	1.09e+15
9109442	-116.28	34.69	3.18	-8.56e+14	-1.22e+14	9.77e+14	-1.25e+15	8.81e+14	3.08e+15
9109496	-116.34	34.68	7.55	-2.72e+14	7.83e+13	1.94e+14	3.95e+14	-4.57e+13	4.28e+14
9109636	-116.36	34.71	9.52	-3.00e+14	-7.73e+14	1.07e+15	6.68e+14	-1.85e+14	1.33e+15
9110685	-116.14	34.35	3.96	-2.57e+13	-1.73e+15	1.76e+15	-2.30e+14	1.28e+14	2.58e+14
9111353	-116.14	34.35	4.47	-4.19e+13	-1.37e+15	1.41e+15	-2.67e+14	4.95e+13	1.02e+15
9112735	-116.34	34.71	9.34	8.38e+13	-2.13e+14	1.29e+14	3.33e+13	5.27e+14	1.06e+15
9113909	-116.40	34.86	4.86	2.57e+14	3.51e+14	-6.08e+14	3.31e+14	1.91e+14	4.83e+14
9114042	-116.27	34.52	7.77	3.12e+14	-3.43e+11	-3.12e+14	-9.43e+12	5.49e+13	1.26e+13
9114612	-116.36	34.70	6.89	-1.34e+14	1.67e+14	-3.29e+13	1.38e+14	-6.66e+13	5.97e+13
9114763	-116.21	34.33	11.53	7.76e+13	-2.48e+14	1.70e+14	5.63e+13	1.92e+14	4.35e+14
9114775	-116.41	34.86	4.93	-9.46e+13	-1.08e+14	2.03e+14	1.47e+14	-3.58e+13	2.16e+14
9114812	-116.41	34.86	3.02	2.21e+15	1.82e+15	-4.03e+15	8.59e+15	2.01e+15	2.14e+16
9114858	-116.38	34.83	5.15	5.96e+13	-2.23e+14	1.64e+14	-1.48e+14	-1.27e+14	5.67e+14
9117942	-116.27	34.52	2.90	2.42e+14	8.12e+14	-1.05e+15	5.73e+14	-1.62e+12	7.53e+14
9119414	-116.36	34.85	5.90	8.20e+12	6.04e+14	-6.12e+14	-7.53e+13	-4.15e+13	6.49e+14
9120741	-116.30	34.79	6.57	-1.06e+14	4.10e+14	-3.05e+14	1.49e+14	-2.35e+14	6.97e+14
9122706	-116.41	34.83	8.36	-7.49e+13	-3.64e+14	4.38e+14	-2.30e+14	4.05e+14	2.19e+15
9128775	-117.01	34.10	4.71	1.47e+14	-7.88e+14	6.41e+14	1.22e+14	-3.08e+14	-2.97e+14
9130422	-116.26	34.59	10.23	3.34e+14	7.80e+13	-4.12e+14	3.21e+14	1.26e+14	4.47e+14
9132433	-117.00	34.10	4.63	4.12e+13	-2.28e+14	1.87e+14	4.22e+13	-8.85e+13	-6.17e+13
9140050	-117.24	34.06	16.34	-5.58e+12	7.66e+13	-7.11e+13	1.48e+13	-2.46e+14	1.77e+15
9147453	-116.27	34.80	6.05	2.33e+13	7.18e+13	-9.51e+13	-4.24e+13	-8.92e+13	2.11e+14
9151000	-118.31	35.09	7.49	8.77e+13	-2.66e+14	1.78e+14	-6.75e+13	1.47e+14	-1.59e+14
9155518	-116.30	34.79	6.53	-2.19e+14	1.72e+15	-1.50e+15	8.06e+14	-5.93e+14	2.87e+15
9165761	-118.92	34.56	17.69	4.31e+14	-4.50e+14	1.86e+13	4.39e+14	9.16e+13	6.46e+13
9169867	-116.77	34.27	5.82	-3.41e+12	-3.65e+14	3.69e+14	-7.59e+13	5.14e+13	-8.62e+13
9171064	-117.17	35.58	6.13	-2.41e+12	-1.82e+14	1.84e+14	2.70e+13	-9.79e+12	2.74e+14
9171679	-119.03	34.89	14.27	2.34e+14	-9.32e+14	6.98e+14	-5.59e+13	-6.16e+14	-7.87e+14
9173365	-118.42	34.28	7.08	1.66e+15	-8.79e+14	-7.85e+14	-1.82e+14	3.10e+14	8.37e+14
9173374	-118.42	34.29	7.30	4.19e+14	-5.13e+14	9.42e+13	2.12e+14	2.61e+14	3.38e+14
9627557	-116.14	33.82	9.68	-5.24e+08	-2.62e+14	2.62e+14	-1.40e+14	-5.38e+13	2.91e+14
9627721	-116.94	34.29	8.28	-4.29e+13	-6.68e+15	6.73e+15	2.35e+15	-1.11e+15	-4.92e+15
9627953	-116.94	34.29	7.90	-1.31e+14	-2.49e+14	3.80e+14	4.10e+14	-1.28e+14	-3.21e+14

Continued on next page

Table A.1 – continued from previous page

EID	Lon (deg)	Lat (deg)	Depth (km)	M_{rr} (N-m)	$M_{\theta\theta}$ (N-m)	$M_{\phi\phi}$ (N-m)	$M_{r\theta}$ (N-m)	$M_{r\phi}$ (N-m)	$M_{\theta\phi}$ (N-m)
9631385	-117.52	35.11	4.22	3.88e+14	-4.07e+14	1.86e+13	1.73e+14	-6.28e+13	1.33e+14
9644101	-117.71	33.87	2.46	3.36e+13	-1.78e+14	1.45e+14	-2.46e+13	8.50e+13	1.45e+13
9652545	-117.44	34.23	8.64	-7.74e+12	-3.28e+14	3.36e+14	-1.90e+14	2.24e+14	6.25e+13
9655209	-116.75	34.03	15.29	1.69e+14	-2.86e+14	1.17e+14	1.58e+13	1.94e+14	-1.56e+14
9666905	-116.76	34.26	4.86	2.02e+13	-2.42e+14	2.22e+14	-1.49e+14	1.25e+14	-6.21e+13
9700049	-116.40	33.38	9.07	-6.84e+11	-1.85e+14	1.86e+14	1.14e+13	-3.10e+12	2.57e+13
9703873	-118.40	34.05	6.37	1.73e+14	-1.03e+15	8.58e+14	-5.33e+14	-4.47e+14	2.27e+15
9716853	-118.28	33.93	19.12	4.10e+14	-2.06e+14	-2.05e+14	6.12e+14	-1.36e+14	3.26e+14
9718013	-116.50	33.51	15.54	-2.57e+15	-1.53e+16	1.79e+16	1.36e+16	1.31e+16	-1.18e+13
9734033	-116.70	34.12	9.32	-4.86e+13	-4.09e+14	4.58e+14	2.27e+14	-1.13e+14	-1.57e+14
9735129	-117.75	33.96	12.45	1.12e+13	-4.84e+14	4.73e+14	-1.04e+14	-1.34e+14	-3.65e+13
9742277	-116.43	33.39	12.91	-2.65e+13	-1.03e+15	1.06e+15	2.47e+14	1.90e+14	-1.89e+13
9753485	-118.66	34.36	11.42	1.85e+15	-1.78e+15	-7.12e+13	1.63e+15	-1.06e+14	4.05e+14
9753489	-118.66	34.37	11.10	3.99e+14	-3.56e+14	-4.29e+13	3.49e+14	9.92e+13	2.98e+14
9753497	-118.66	34.37	11.52	4.42e+14	-4.49e+14	7.71e+12	1.96e+14	6.63e+13	-5.23e+12
9753949	-118.67	34.36	10.33	9.70e+13	-1.09e+14	1.17e+13	2.89e+14	1.60e+14	-1.77e+13
9755013	-118.67	34.36	10.90	2.15e+14	-2.09e+14	-5.94e+12	1.91e+14	6.29e+13	-4.02e+13
9775765	-116.30	34.52	4.83	-7.72e+14	3.78e+14	3.94e+14	-4.56e+14	-9.34e+13	-5.68e+14
9805021	-116.44	34.57	9.00	1.70e+14	1.49e+13	-1.85e+14	1.07e+14	-3.47e+13	7.82e+13
9818433	-117.78	33.91	8.59	-6.05e+13	-3.81e+15	3.87e+15	-5.05e+14	-3.73e+14	-1.53e+15
9853417	-116.57	33.51	13.51	3.35e+12	-2.03e+14	2.00e+14	-9.21e+11	-2.77e+13	8.37e+13
9854597	-116.27	34.81	7.89	-4.62e+13	-9.82e+14	1.03e+15	-2.69e+14	4.60e+14	4.49e+15
9875657	-118.67	35.32	3.75	-5.25e+14	2.28e+14	2.97e+14	3.00e+14	-1.49e+14	-2.83e+14
9875665	-118.66	35.31	4.13	-2.39e+14	-1.93e+14	4.32e+14	2.39e+14	-9.13e+13	-7.37e+13
9882325	-118.66	35.32	4.41	-5.54e+14	1.69e+12	5.53e+14	7.06e+14	-4.11e+14	-3.56e+14
9882329	-118.66	35.31	4.12	-1.39e+15	-8.62e+14	2.25e+15	1.32e+15	-3.12e+14	-6.55e+14
9915709	-116.02	33.75	8.54	-1.86e+14	1.34e+14	5.18e+13	1.32e+13	-1.88e+14	1.94e+14
9930549	-116.67	34.62	9.16	1.61e+14	-1.04e+14	-5.67e+13	9.51e+13	-2.33e+14	-3.89e+14
9941081	-118.65	34.40	13.64	-3.39e+13	-1.76e+13	5.15e+13	6.10e+14	8.48e+13	1.74e+14
9983429	-119.14	35.01	11.81	6.37e+15	-6.41e+15	3.98e+13	2.95e+14	1.25e+15	-1.10e+15
10006857	-120.01	34.41	10.97	-1.28e+14	-2.03e+15	2.16e+15	5.15e+14	-2.02e+13	-2.15e+14
10059745	-116.84	34.35	10.31	3.53e+14	-6.31e+14	2.78e+14	-5.40e+13	-3.25e+14	1.69e+14
10094253	-118.63	33.83	11.28	2.82e+14	-2.93e+14	1.05e+13	1.92e+13	-3.02e+13	6.70e+13
10097009	-119.20	35.00	13.01	4.84e+14	-6.24e+14	1.40e+14	-4.93e+14	-4.77e+14	1.10e+15
10148369	-116.77	34.02	17.58	3.67e+13	-3.19e+14	2.82e+14	4.64e+14	2.59e+14	1.83e+14
10148421	-116.77	34.02	18.32	3.61e+14	-1.15e+15	7.89e+14	8.68e+14	6.55e+14	4.37e+14
10187953	-116.79	33.92	20.53	9.23e+13	-3.03e+14	2.11e+14	1.28e+14	1.82e+14	-1.50e+13
10223765	-116.04	33.71	13.95	-7.72e+13	-7.27e+14	8.04e+14	3.58e+14	2.96e+14	-2.76e+13
10370141	-117.30	34.11	14.20	1.05e+15	-2.11e+15	1.06e+15	1.38e+15	1.54e+15	4.19e+15
10972299	-117.46	34.27	10.80	3.01e+14	-2.79e+14	-2.17e+13	2.26e+14	1.28e+14	2.81e+14
12659440	-119.33	33.67	14.10	2.88e+15	-1.61e+15	-1.27e+15	1.69e+14	-2.08e+14	1.43e+15
12887732	-118.08	35.71	4.30	1.55e+13	-2.20e+14	2.04e+14	2.82e+13	-5.92e+13	-3.17e+13
13692644	-117.43	34.17	7.75	-1.69e+13	-2.51e+14	2.68e+14	7.04e+13	-4.64e+13	6.41e+13
13813696	-116.76	33.50	17.83	1.04e+13	-1.97e+14	1.87e+14	7.47e+13	-8.82e+13	8.23e+12
13935988	-116.85	34.31	4.55	-2.74e+15	-1.73e+16	2.00e+16	-7.16e+15	-2.52e+15	-1.00e+15
13936432	-116.85	34.32	5.51	-1.04e+14	-1.97e+14	3.00e+14	-1.49e+14	-1.02e+14	-2.29e+14
13936596	-116.84	34.31	5.43	-1.36e+13	-2.46e+14	2.60e+14	-6.41e+13	-7.58e+13	-1.63e+14
13936812	-116.85	34.31	4.87	2.23e+15	-2.27e+15	3.41e+13	-1.17e+14	-2.82e+14	-4.35e+13
13938812	-116.84	34.31	3.84	-1.47e+14	-1.26e+15	1.41e+15	-4.39e+14	-8.98e+13	-1.62e+12
13939856	-116.84	34.30	5.44	-5.49e+13	-3.76e+14	4.31e+14	-1.49e+14	-7.67e+13	-8.71e+13
13945908	-116.13	34.36	8.08	-4.59e+13	-2.09e+15	2.13e+15	-3.47e+14	1.59e+14	-6.73e+12
14000376	-118.74	34.29	8.60	1.94e+14	-3.16e+14	1.22e+14	-1.53e+13	-1.54e+14	-1.14e+12
14007388	-117.57	35.64	2.13	3.51e+13	-2.02e+14	1.66e+14	1.37e+13	-8.42e+13	5.30e+13
14073800	-116.05	33.72	12.20	1.47e+11	-4.72e+14	4.72e+14	1.96e+14	2.30e+14	-7.47e+13
14077668	-119.44	34.39	8.66	1.07e+15	-1.10e+15	3.04e+13	8.28e+14	2.02e+14	4.02e+13
14079184	-117.45	34.14	6.26	2.52e+13	-2.44e+14	2.19e+14	6.48e+13	8.71e+13	4.04e+13
14095628	-118.63	35.39	7.66	-3.26e+14	-1.06e+16	1.10e+16	5.89e+15	-1.82e+15	-1.21e+16
14116920	-117.44	34.12	5.08	2.66e+13	-2.26e+14	1.99e+14	5.16e+13	8.34e+13	1.87e+13
14116972	-117.44	34.13	5.04	1.18e+14	-1.71e+15	1.60e+15	3.48e+14	5.35e+14	6.83e+13
14118096	-116.39	33.96	8.51	-5.53e+13	-6.42e+14	6.98e+14	2.47e+14	-2.97e+14	2.99e+14
14138080	-119.19	35.00	10.16	6.53e+15	-6.94e+15	4.14e+14	-4.63e+15	-2.92e+15	-9.47e+14
14139108	-120.03	33.69	16.88	7.69e+14	-7.94e+14	2.53e+13	2.48e+14	-2.47e+14	1.69e+14
14139160	-120.03	33.69	17.40	7.49e+14	-7.74e+14	2.46e+13	2.42e+14	-2.40e+14	1.65e+14
14151344	-116.57	33.54	13.91	6.15e+15	-4.22e+16	3.60e+16	1.24e+16	2.57e+16	-1.74e+16

Continued on next page

Table A.1 – continued from previous page

EID	Lon (deg)	Lat (deg)	Depth (km)	M_{rr} (N-m)	$M_{\theta\theta}$ (N-m)	$M_{\phi\phi}$ (N-m)	$M_{r\theta}$ (N-m)	$M_{r\phi}$ (N-m)	$M_{\theta\phi}$ (N-m)
14155260	-117.01	34.06	14.19	1.04e+16	-1.51e+16	4.75e+15	6.16e+15	7.02e+15	4.36e+15
14158696	-117.02	34.06	13.63	3.45e+13	-2.09e+14	1.75e+14	8.50e+13	7.82e+13	2.26e+14
14165408	-119.75	33.69	3.85	5.76e+13	-3.20e+14	2.62e+14	-1.40e+14	-1.48e+14	6.43e+14
14186612	-119.02	35.02	10.24	4.79e+15	-4.74e+15	-4.49e+13	-2.22e+15	7.64e+14	6.27e+14
14186928	-119.04	35.02	9.13	2.37e+14	-2.50e+14	1.29e+13	8.21e+12	6.08e+13	2.82e+13
14187364	-118.47	35.38	8.81	3.87e+13	-1.46e+14	1.07e+14	-7.19e+13	-1.04e+14	-3.47e+13
14204000	-117.55	35.13	4.63	-1.45e+13	-1.42e+14	1.57e+14	8.22e+13	2.04e+13	1.30e+14
14219360	-117.58	35.62	8.98	-2.27e+13	-1.03e+14	1.26e+14	-8.47e+13	2.68e+13	2.83e+14
14239184	-117.11	33.86	16.77	-9.84e+13	-9.31e+13	1.91e+14	-1.64e+14	3.03e+14	5.51e+13
14383980	-117.76	33.95	14.23	9.04e+16	-1.46e+17	5.59e+16	-2.82e+16	7.23e+16	-4.03e+16
14408052	-116.42	34.81	6.10	0.00e+00	-1.97e+16	1.97e+16	-4.67e+15	1.28e+16	2.35e+16
14418600	-117.79	35.41	8.50	-6.29e+12	-7.06e+14	7.13e+14	-9.35e+13	-1.58e+13	4.82e+14

Table A.2: List of stations used in the study. Here we list the location in UTM and lot-lan coordinates, and the elevation for the simulations that are conducted using a topographic surface.

Station	X (m)	Y (m)	Elevation (m)	Lon (degree)	Lat (degree)
NE001	402194.51	3823693.98	846.32	-118.07	34.55
NE002	432199.44	3823692.06	917.61	-117.74	34.55
NE003	402237.80	3853694.03	695.19	-118.07	34.82
NE004	432236.82	3853700.68	807.48	-117.74	34.83
NE005	462201.48	3823698.55	904.66	-117.41	34.56
NE006	402193.90	3883696.41	804.88	-118.07	35.09
NE007	462232.80	3853694.51	821.30	-117.41	34.83
NE008	432276.83	3883699.57	765.90	-117.74	35.10
NE009	462265.56	3883691.82	722.35	-117.41	35.10
NE010	492201.84	3823691.28	997.08	-117.08	34.56
NE011	402245.45	3913699.15	1028.20	-118.08	35.36
NE012	492227.18	3853697.69	772.38	-117.08	34.83
NE013	432228.72	3913700.48	744.03	-117.75	35.37
NE014	492252.68	3883694.37	937.42	-117.08	35.10
NE015	462208.91	3913690.87	920.99	-117.42	35.37
NE016	522201.89	3823692.41	1030.55	-116.76	34.56
NE017	402210.34	3943693.13	2012.60	-118.08	35.63
NE018	522221.20	3853699.13	687.32	-116.76	34.83
NE019	432274.39	3943690.99	736.37	-117.75	35.64
NE020	492278.35	3913692.41	1045.86	-117.08	35.37
NE021	522239.44	3883696.11	534.75	-116.76	35.10
NE022	462244.92	3943702.00	664.62	-117.42	35.64
NE023	552202.91	3823690.87	904.79	-116.43	34.56
NE024	522256.59	3913694.46	1077.27	-116.75	35.37
NE025	492213.66	3943691.89	692.13	-117.09	35.64
NE026	402270.21	3973698.57	2308.32	-118.08	35.90
NE027	552216.19	3853698.83	660.27	-116.43	34.83
NE028	432232.64	3973694.63	742.39	-117.75	35.91
NE029	552227.18	3883697.06	579.01	-116.43	35.10

Continued on next page

Table A.2 – continued from previous page

Station	X (m)	Y (m)	Elevation (m)	Lon (degree)	Lat (degree)
NE030	462282.28	3973692.30	1419.04	-117.42	35.91
NE031	522272.63	3943694.16	932.07	-116.75	35.64
NE032	552235.80	3913696.64	728.14	-116.42	35.37
NE033	492239.98	3973692.66	1403.34	-117.09	35.91
NE034	582206.11	3823697.75	538.65	-116.10	34.55
NE035	402244.05	4003695.27	2594.76	-118.09	36.17
NE036	582213.48	3853696.80	552.59	-116.10	34.82
NE037	432194.25	4003699.64	2118.65	-117.75	36.18
NE038	582217.22	3883697.20	293.43	-116.10	35.09
NE039	462231.22	4003695.46	1020.52	-117.42	36.18
NE040	552242.04	3943697.58	137.34	-116.42	35.64
NE041	522197.33	3973695.01	42.48	-116.75	35.91
NE042	582217.31	3913698.96	321.42	-116.09	35.37
NE043	492266.48	4003694.81	2733.61	-117.09	36.18
NE044	612212.98	3823690.86	206.92	-115.78	34.55
NE045	402222.55	4033693.34	2172.23	-118.09	36.45
NE046	612214.38	3853693.04	1163.95	-115.77	34.82
NE047	552245.89	3973699.89	997.72	-116.42	35.91
NE048	432248.77	4033694.24	2013.86	-117.76	36.45
NE049	582213.86	3943690.97	449.03	-116.09	35.64
NE050	522211.46	4003697.46	563.32	-116.75	36.18
NE051	612210.88	3883696.56	1097.18	-115.77	35.09
NE052	462271.86	4033699.60	630.33	-117.42	36.45
NE053	612202.60	3913690.33	1294.59	-115.77	35.36
NE054	492203.54	4033698.41	1476.52	-117.09	36.45
NE055	582206.63	3973695.44	849.76	-116.09	35.91
NE056	552247.41	4003692.48	748.82	-116.42	36.18
NE057	642224.62	3823692.41	318.19	-115.45	34.55
NE058	642220.05	3853698.65	749.41	-115.44	34.82
NE059	612279.80	3943697.68	993.71	-115.76	35.63
NE060	522224.47	4033701.28	728.48	-116.75	36.45
NE061	642209.49	3883695.13	1570.40	-115.44	35.09
NE062	582195.72	4003701.27	773.34	-116.09	36.18
NE063	642283.61	3913694.38	1054.09	-115.43	35.36
NE064	612261.34	3973694.15	884.28	-115.76	35.90
NE065	552246.46	4033697.53	674.02	-116.42	36.45
NE066	642260.36	3943693.54	944.92	-115.43	35.63
NE067	672242.43	3823691.31	1039.06	-115.12	34.54
NE068	672232.12	3853691.47	742.16	-115.12	34.81
NE069	672214.38	3883692.94	1159.98	-115.11	35.08
NE070	612237.92	4003691.97	1751.09	-115.75	36.17
NE071	582270.85	4033698.23	1024.36	-116.08	36.45
NE072	642230.87	3973694.03	1369.97	-115.42	35.90
NE073	672280.06	3913697.47	1388.09	-115.10	35.35
NE074	672247.08	3943701.59	1258.24	-115.10	35.62

Continued on next page

Table A.2 – continued from previous page

Station	X (m)	Y (m)	Elevation (m)	Lon (degree)	Lat (degree)
NE075	612209.37	4033702.24	1698.48	-115.75	36.44
NE076	702267.50	3823698.67	446.49	-114.80	34.54
NE077	642195.14	4003695.86	1339.01	-115.42	36.17
NE078	702251.54	3853693.69	642.14	-114.79	34.81
NE079	702226.64	3883701.10	709.64	-114.78	35.08
NE080	672206.80	3973695.94	983.21	-115.09	35.89
NE081	702284.14	3913700.75	908.96	-114.77	35.35
NE082	642242.78	4033700.50	917.56	-115.41	36.44
NE083	702241.69	3943699.68	610.54	-114.77	35.62
NE084	672248.95	4003693.38	548.34	-115.08	36.16
NE085	702280.74	3973701.97	722.45	-114.76	35.89
NE086	672282.71	4033703.26	1482.45	-115.08	36.44
NE087	702220.64	4003692.42	506.19	-114.75	36.16
NE088	702241.11	4033697.36	708.02	-114.74	36.43
NW001	372234.60	3853696.75	790.42	-118.40	34.82
NW002	372197.78	3883691.78	1369.15	-118.40	35.09
NW003	342225.82	3853697.76	997.85	-118.72	34.82
NW004	342196.19	3883697.48	595.01	-118.73	35.09
NW005	372257.85	3913697.96	1144.18	-118.41	35.36
NW006	312210.14	3853697.07	1728.45	-119.05	34.81
NW007	342264.56	3913696.93	490.59	-118.74	35.36
NW008	312278.86	3883700.53	112.61	-119.06	35.08
NW009	372232.47	3943695.67	924.69	-118.41	35.63
NW010	282277.72	3853692.54	1181.87	-119.38	34.80
NW011	312264.27	3913696.08	118.88	-119.07	35.35
NW012	342248.92	3943699.30	885.87	-118.74	35.63
NW013	282261.84	3883693.33	228.12	-119.39	35.07
NW014	312258.11	3943692.96	258.82	-119.07	35.62
NW015	282255.63	3913695.43	87.69	-119.40	35.34
NW016	372213.00	3973694.73	2164.65	-118.42	35.90
NW017	252244.57	3853699.31	1366.67	-119.71	34.80
NW018	342240.26	3973691.92	757.54	-118.75	35.90
NW019	252235.47	3883696.51	812.00	-119.72	35.07
NW020	282259.13	3943698.84	85.65	-119.40	35.62
NW021	312260.41	3973691.15	151.66	-119.08	35.89
NW022	252237.32	3913695.01	554.96	-119.73	35.34
NW023	372199.46	4003695.15	1847.52	-118.42	36.17
NW024	222200.26	3853693.35	830.26	-120.04	34.79
NW025	342239.01	4003696.97	979.57	-118.75	36.17
NW026	222198.19	3883699.01	823.47	-120.05	35.06
NW027	282272.10	3973692.45	61.31	-119.41	35.89
NW028	252250.15	3943694.78	127.02	-119.73	35.61
NW029	312271.43	4003701.77	119.07	-119.09	36.16
NW030	222208.00	3913694.83	643.59	-120.06	35.33
NW031	372281.49	4033695.60	2565.58	-118.42	36.44

Continued on next page

Table A.2 – continued from previous page

Station	X (m)	Y (m)	Elevation (m)	Lon (degree)	Lat (degree)
NW032	252274.00	3973695.83	59.45	-119.74	35.88
NW033	192235.66	3853693.81	211.18	-120.36	34.78
NW034	282205.13	4003700.70	75.02	-119.42	36.16
NW035	222230.07	3943691.90	463.93	-120.07	35.60
NW036	342244.79	4033692.27	1396.68	-118.76	36.44
NW037	192239.93	3883697.74	325.14	-120.37	35.05
NW038	312200.85	4033693.46	183.51	-119.09	36.43
NW039	192257.29	3913691.81	493.97	-120.39	35.32
NW040	252218.91	4003700.71	57.85	-119.75	36.15
NW041	222264.77	3973701.33	244.70	-120.08	35.87
NW042	282237.98	4033696.93	88.17	-119.43	36.43
NW043	192197.92	3943701.34	415.65	-120.40	35.59
NW044	162257.64	3853692.10	-48.05	-120.69	34.77
NW045	162268.12	3883695.25	-38.46	-120.70	35.04
NW046	222221.10	4003692.68	107.22	-120.09	36.14
NW047	162202.39	3913703.02	138.80	-120.72	35.31
NW048	252264.89	4033693.24	72.98	-119.76	36.42
NW049	192242.69	3973697.89	461.66	-120.41	35.86
NW050	162242.31	3943697.50	292.00	-120.73	35.58
NW051	132265.29	3853699.35	-443.43	-121.02	34.76
NW052	222280.47	4033693.52	69.60	-120.10	36.41
NW053	192211.03	4003698.82	374.29	-120.42	36.13
NW054	132281.45	3883691.56	-446.61	-121.03	35.03
NW055	162206.71	3973696.63	271.48	-120.74	35.85
NW056	132223.08	3913699.76	-231.21	-121.04	35.30
NW057	132271.62	3943694.33	97.32	-121.06	35.57
NW058	192283.38	4033697.82	265.46	-120.43	36.40
NW059	162276.67	4003693.51	535.04	-120.75	36.12
NW060	102256.46	3853693.40	-567.16	-121.34	34.75
NW061	102279.08	3883697.81	-477.42	-121.36	35.02
NW062	132245.89	3973693.83	401.37	-121.07	35.84
NW063	102227.47	3913696.28	-725.37	-121.37	35.29
NW064	162271.83	4033695.07	966.49	-120.77	36.39
NW065	102193.80	3943695.94	-515.38	-121.39	35.56
NW066	132236.94	4003694.53	183.42	-121.08	36.11
NW067	102268.54	3973692.69	65.15	-121.40	35.83
NW068	132244.84	4033696.41	337.15	-121.10	36.38
NW069	102270.62	4003694.65	696.49	-121.42	36.10
NW070	102201.04	4033701.89	1035.41	-121.43	36.37
SW001	372277.11	3823691.98	1003.82	-118.39	34.55
SW002	402247.25	3793694.30	1345.99	-118.06	34.28
SW003	372233.53	3793700.89	379.90	-118.39	34.28
SW004	342262.57	3823699.38	690.23	-118.72	34.54
SW005	402212.18	3763696.91	72.32	-118.06	34.01
SW006	342214.14	3793692.79	334.55	-118.71	34.27

Continued on next page

Table A.2 – continued from previous page

Station	X (m)	Y (m)	Elevation (m)	Lon (degree)	Lat (degree)
SW007	372195.01	3763700.03	50.35	-118.38	34.01
SW008	342264.74	3763697.06	-51.94	-118.71	34.00
SW009	312240.99	3823693.05	1396.74	-119.05	34.54
SW010	402273.69	3733699.91	4.89	-118.06	33.74
SW011	312280.18	3793690.35	148.04	-119.04	34.27
SW012	372254.34	3733699.24	60.27	-118.38	33.74
SW013	312235.33	3763690.80	-237.23	-119.03	34.00
SW014	342229.53	3733693.09	-911.49	-118.70	33.73
SW015	282211.46	3823695.20	1001.99	-119.37	34.53
SW016	402246.67	3703694.09	-508.15	-118.05	33.47
SW017	282246.30	3793697.00	-23.94	-119.36	34.26
SW018	372226.34	3703689.93	-739.22	-118.38	33.47
SW019	312198.18	3733692.54	-896.79	-119.03	33.73
SW020	282198.07	3763691.13	-197.98	-119.36	33.99
SW021	342200.76	3703690.42	-560.65	-118.70	33.46
SW022	252264.27	3823692.29	557.95	-119.70	34.53
SW023	282251.74	3733695.52	-1277.75	-119.35	33.72
SW024	312261.66	3703693.76	-100.37	-119.02	33.46
SW025	402223.56	3673689.59	-720.34	-118.05	33.20
SW026	252203.04	3793700.09	-189.71	-119.69	34.26
SW027	372203.66	3673693.01	-1173.09	-118.37	33.20
SW028	252244.16	3763695.63	141.51	-119.68	33.99
SW029	342271.80	3673698.63	-1153.97	-118.69	33.19
SW030	282221.70	3703692.21	-1478.17	-119.34	33.45
SW031	252203.38	3733694.87	-1798.15	-119.67	33.72
SW032	312240.13	3673698.09	-1202.36	-119.01	33.19
SW033	222214.84	3823700.05	562.42	-120.03	34.52
SW034	402204.47	3643697.48	-879.51	-118.05	32.93
SW035	222241.21	3793696.93	-585.96	-120.02	34.25
SW036	372279.63	3643696.19	-1144.42	-118.37	32.93
SW037	222279.68	3763695.08	20.28	-120.01	33.98
SW038	342256.12	3643698.57	-1069.98	-118.69	32.92
SW039	252265.77	3703692.97	-119.02	-119.67	33.45
SW040	282200.56	3673690.18	-747.82	-119.34	33.18
SW041	222237.49	3733697.19	-119.36	-120.00	33.71
SW042	312226.03	3643692.61	-1617.10	-119.01	32.92
SW043	192244.84	3823691.12	304.15	-120.35	34.51
SW044	402282.95	3613694.68	-543.37	-118.04	32.66
SW045	192267.41	3793689.68	-450.71	-120.34	34.24
SW046	252245.62	3673694.73	-456.46	-119.66	33.18
SW047	372267.36	3613690.80	-810.51	-118.36	32.66
SW048	222206.73	3703700.53	-929.38	-119.99	33.44
SW049	282282.09	3643698.44	-370.11	-119.33	32.91
SW050	192210.89	3763692.49	-95.08	-120.33	33.97
SW051	342246.62	3613688.71	-1139.89	-118.68	32.65

Continued on next page

Table A.2 – continued from previous page

Station	X (m)	Y (m)	Elevation (m)	Lon (degree)	Lat (degree)
SW052	192259.82	3733693.52	-1035.92	-120.32	33.70
SW053	312219.74	3613699.50	-670.58	-119.00	32.65
SW054	222280.32	3673691.37	-1167.12	-119.98	33.17
SW055	252235.57	3643697.75	-1328.31	-119.65	32.91
SW056	162261.85	3823690.17	-104.79	-120.68	34.50
SW057	162280.72	3793689.46	-638.75	-120.67	34.23
SW058	192228.98	3703698.78	-775.26	-120.31	33.43
SW059	282278.71	3613687.88	-251.28	-119.32	32.64
SW060	162221.73	3763693.27	-1604.90	-120.66	33.96
SW061	222272.59	3643697.22	-1073.08	-119.97	32.90
SW062	162269.45	3733694.99	-1295.11	-120.64	33.69
SW063	192210.42	3673694.16	-742.76	-120.30	33.16
SW064	252235.33	3613690.93	-787.86	-119.64	32.63
SW065	162238.25	3703690.11	-1362.44	-120.63	33.42
SW066	132264.65	3823697.23	-986.32	-121.00	34.49
SW067	132279.92	3793696.30	-977.78	-120.99	34.22
SW068	132218.55	3763700.17	-2235.80	-120.98	33.95
SW069	192204.46	3643690.77	-733.49	-120.29	32.89
SW070	222275.86	3613693.21	-1303.56	-119.96	32.63
SW071	162221.31	3673697.52	-3029.48	-120.62	33.15
SW072	132264.75	3733690.53	-3283.07	-120.97	33.68
SW073	132234.06	3703696.75	-3519.67	-120.95	33.41
SW074	192211.40	3613699.69	-3229.53	-120.28	32.62
SW075	102251.07	3823690.14	-1853.51	-121.33	34.48
SW076	162217.82	3643695.04	-3900.47	-120.61	32.88
SW077	102263.31	3793699.15	-2574.72	-121.32	34.21
SW078	102199.68	3763702.12	-3232.11	-121.30	33.94
SW079	132218.07	3673693.04	-2121.58	-120.94	33.14
SW080	102244.86	3733691.26	-3476.62	-121.29	33.67
SW081	162228.12	3613693.77	-3813.47	-120.60	32.61
SW082	102214.40	3703696.53	-3707.19	-121.28	33.40
SW083	132217.15	3643690.52	-3749.66	-120.93	32.87
SW084	102199.85	3673691.85	-3812.07	-121.26	33.13
SW085	132231.26	3613689.19	-3833.75	-120.92	32.60
SW086	102202.06	3643699.42	-3880.56	-121.25	32.86
SW087	102220.06	3613697.07	-3842.86	-121.24	32.59
SE001	432256.88	3793695.19	1398.69	-117.74	34.28
SE002	432225.27	3763700.34	246.26	-117.73	34.01
SE003	462263.60	3793692.47	1322.90	-117.41	34.29
SE004	462235.45	3763699.21	316.24	-117.41	34.02
SE005	432196.26	3733695.73	230.51	-117.73	33.74
SE006	492268.73	3793697.22	1742.73	-117.08	34.29
SE007	462208.68	3733696.19	542.05	-117.41	33.74
SE008	492244.03	3763693.51	668.30	-117.08	34.02
SE009	432262.86	3703691.80	-19.79	-117.73	33.47

Continued on next page

Table A.2 – continued from previous page

Station	X (m)	Y (m)	Elevation (m)	Lon (degree)	Lat (degree)
SE010	522273.50	3793698.35	1886.78	-116.76	34.29
SE011	492219.51	3733691.13	584.05	-117.08	33.75
SE012	462276.26	3703694.14	599.58	-117.41	33.47
SE013	522252.31	3763694.33	1739.25	-116.76	34.02
SE014	492195.17	3703690.09	360.41	-117.08	33.47
SE015	522230.03	3733691.65	1638.28	-116.76	33.74
SE016	432239.49	3673689.84	-794.45	-117.73	33.20
SE017	552279.24	3793695.86	976.33	-116.43	34.28
SE018	462252.63	3673693.78	-10.68	-117.41	33.20
SE019	552261.55	3763690.59	1041.28	-116.43	34.01
SE020	522206.68	3703690.31	1211.72	-116.76	33.47
SE021	492264.20	3673690.31	356.18	-117.08	33.20
SE022	552241.45	3733697.75	206.78	-116.44	33.74
SE023	432218.78	3643689.21	-975.01	-117.72	32.93
SE024	582195.12	3793700.03	609.79	-116.11	34.28
SE025	462230.42	3643694.75	-608.62	-117.40	32.93
SE026	582272.97	3763693.38	1359.92	-116.11	34.01
SE027	522275.46	3673690.51	1094.84	-116.76	33.20
SE028	552219.09	3703695.15	1323.67	-116.44	33.47
SE029	492240.49	3643691.92	212.06	-117.08	32.93
SE030	582255.08	3733698.34	243.65	-116.11	33.74
SE031	432200.72	3613689.89	-452.98	-117.72	32.66
SE032	552194.41	3673693.89	941.09	-116.44	33.20
SE033	612206.71	3793690.02	844.50	-115.78	34.28
SE034	522250.25	3643691.82	474.32	-116.76	32.93
SE035	582233.70	3703693.54	-24.00	-116.11	33.47
SE036	462209.62	3613697.03	-301.45	-117.40	32.66
SE037	612195.56	3763690.51	771.78	-115.78	34.01
SE038	492216.95	3613694.86	22.23	-117.08	32.66
SE039	612272.21	3733693.42	1069.75	-115.79	33.74
SE040	552260.90	3643694.44	1009.73	-116.44	32.93
SE041	582208.75	3673690.07	72.46	-116.12	33.20
SE042	522223.97	3613694.45	596.95	-116.76	32.66
SE043	612251.67	3703696.56	-25.94	-115.79	33.47
SE044	642222.87	3793698.58	240.92	-115.45	34.28
SE045	642215.16	3763694.99	542.71	-115.46	34.01
SE046	582273.64	3643699.78	207.95	-116.12	32.93
SE047	642201.35	3733692.72	333.56	-115.47	33.74
SE048	552231.88	3613695.81	941.13	-116.44	32.66
SE049	612226.45	3673689.93	-71.00	-115.80	33.20
SE050	642274.40	3703693.13	651.88	-115.47	33.47
SE051	672245.33	3793692.47	211.48	-115.13	34.27
SE052	582241.88	3613698.94	993.17	-116.12	32.66
SE053	612196.30	3643695.71	53.85	-115.80	32.93
SE054	672240.84	3763694.93	609.26	-115.14	34.00

Continued on next page

Table A.2 – continued from previous page

Station	X (m)	Y (m)	Elevation (m)	Lon (degree)	Lat (degree)
SE055	642248.73	3673693.48	-41.31	-115.47	33.19
SE056	672229.00	3733698.71	243.58	-115.14	33.73
SE057	672210.02	3703692.71	600.61	-115.15	33.46
SE058	612255.28	3613692.76	68.60	-115.80	32.66
SE059	642217.01	3643695.14	-40.02	-115.48	32.92
SE060	702275.03	3793693.87	822.03	-114.80	34.27
SE061	702273.68	3763701.45	215.79	-114.81	34.00
SE062	672276.77	3673700.74	467.63	-115.15	33.19
SE063	702263.95	3733699.23	212.72	-114.82	33.73
SE064	642273.08	3613699.45	0.42	-115.48	32.65
SE065	702245.64	3703698.31	148.25	-114.82	33.46
SE066	672243.48	3643697.33	35.01	-115.16	32.92
SE067	702218.77	3673698.69	333.67	-114.83	33.19
SE068	672202.93	3613695.22	23.48	-115.16	32.65
SE069	702277.14	3643691.19	198.93	-114.84	32.91
SE070	702233.52	3613694.13	28.18	-114.84	32.64

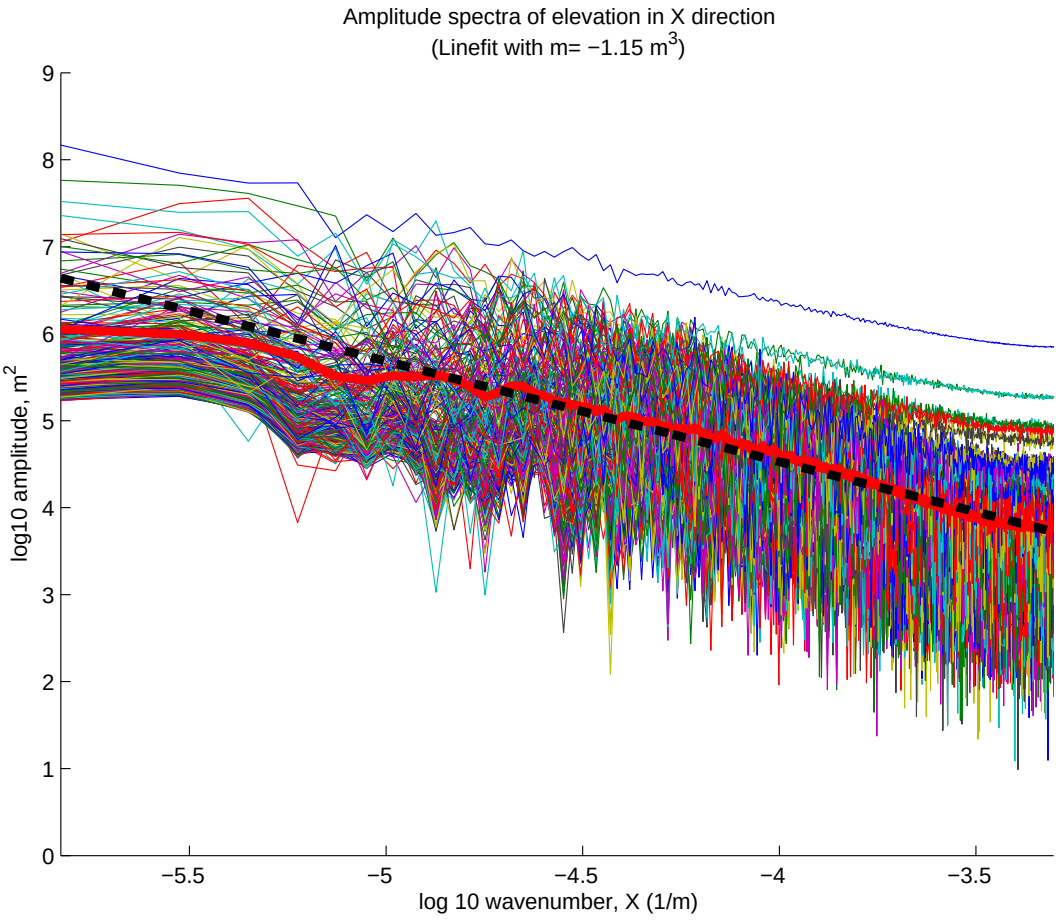

Figure A.1: Amplitude spectrum of topography in the x direction.
Each curve is the amplitude spectrum, obtained via Fourier transform, of an east-west profile through the topography of southern California (Figure 1.1). The x-axis is $\log_{10} k$ and the y-axis is $\log_{10} A(k)$ The average amplitude is plotted in red and a linear line fit is plotted in black dash. The slope of the line fit is -1.15 m^3. This figure shows that southern California exhibits the characteristic power-law relationship of topography.

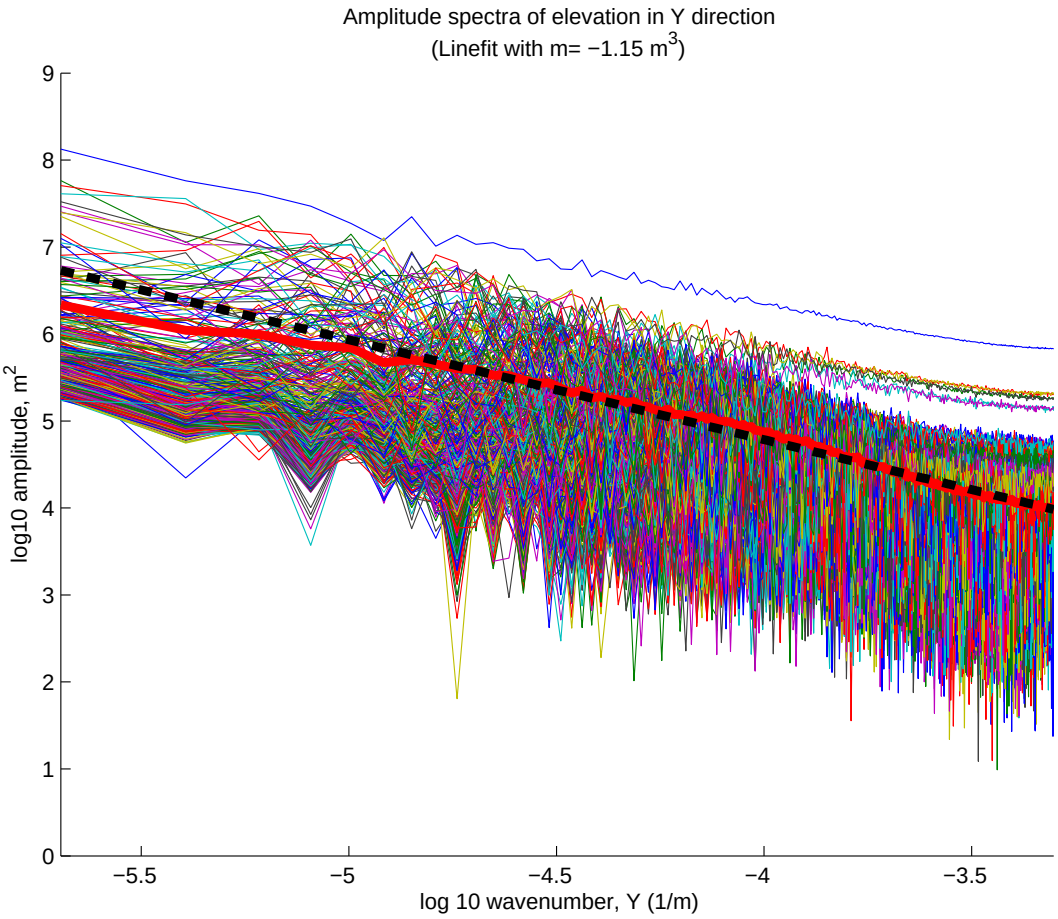

Figure A.2: Amplitude spectrum of topography in the y direction.
Same as Figure A.1, but for the y direction. The best-fitting slope is -1.15 m^3.

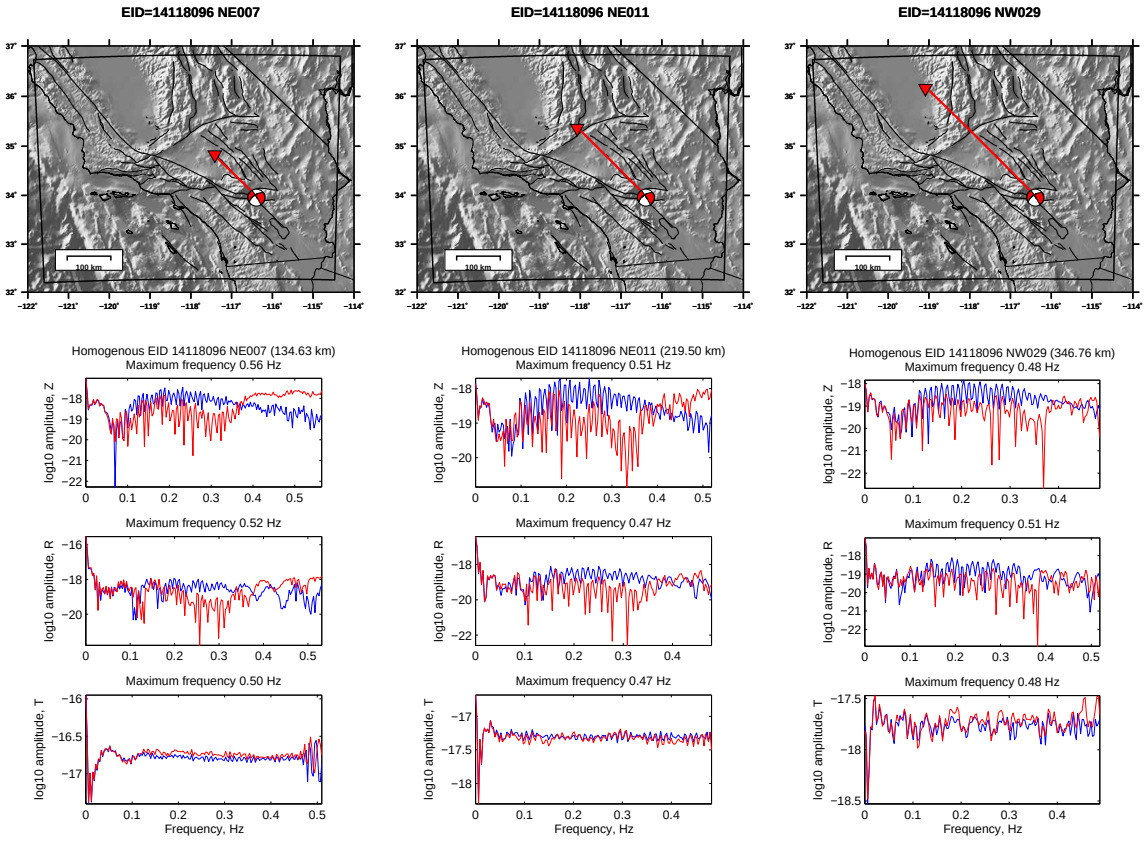

(a) NE007 (b) NE011 (c) NW029

Figure A.3: Amplitude spectra for waveforms in Figure 3.31.

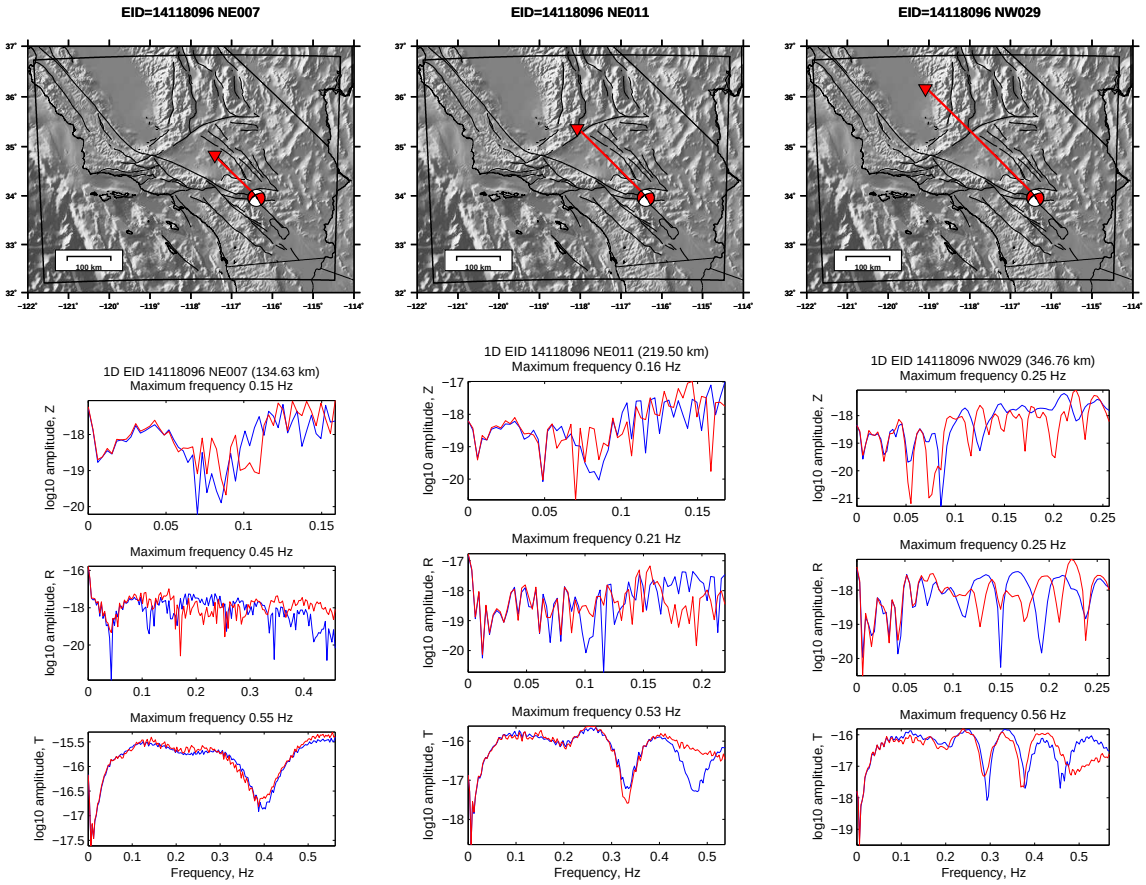

(a) NE007 (b) NE011 (c) NW029

Figure A.4: Amplitude spectra for waveforms in Figure 3.32.

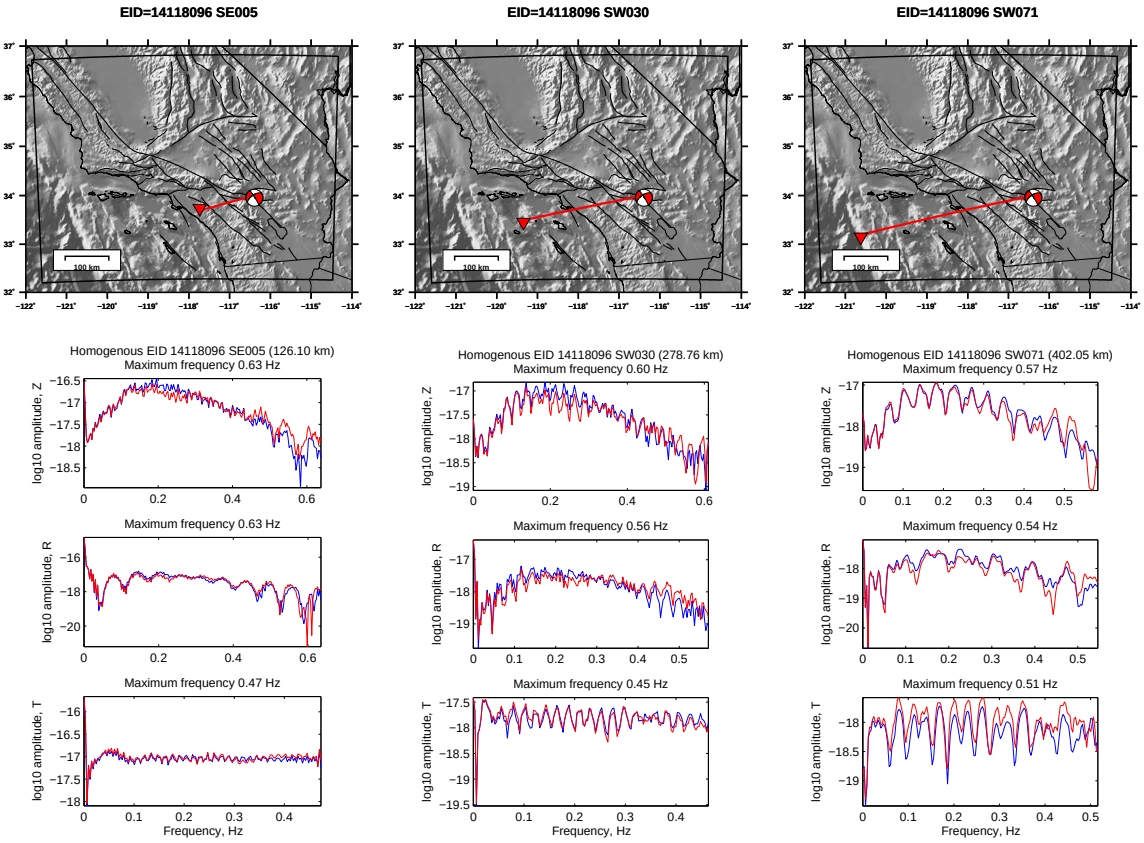

(a) SE005 (b) SW030 (c) SW071

Figure A.5: Amplitude spectra for waveforms in Figure 3.33.

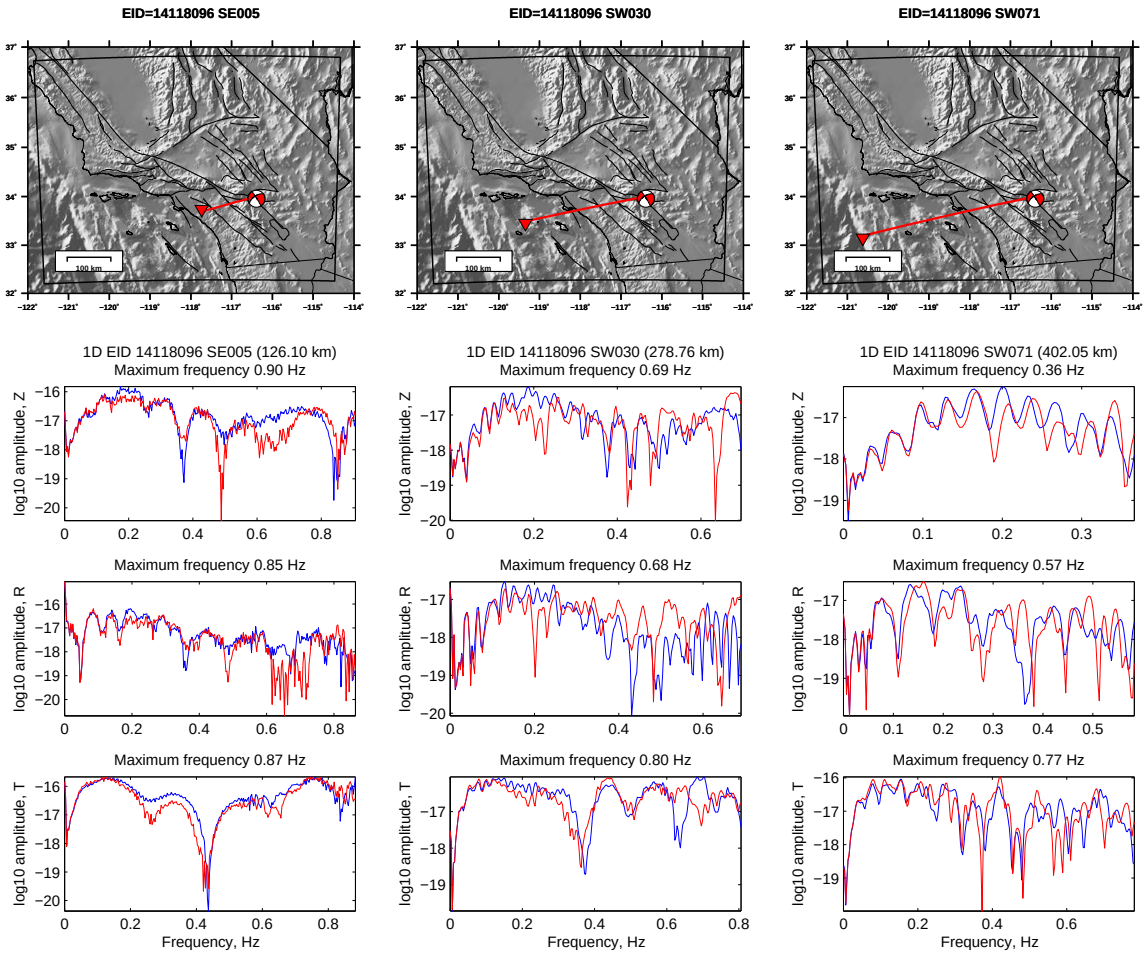

(a) SE005 (b) SW030 (c) SW071

Figure A.6: Amplitude spectra for waveforms in Figure 3.34.

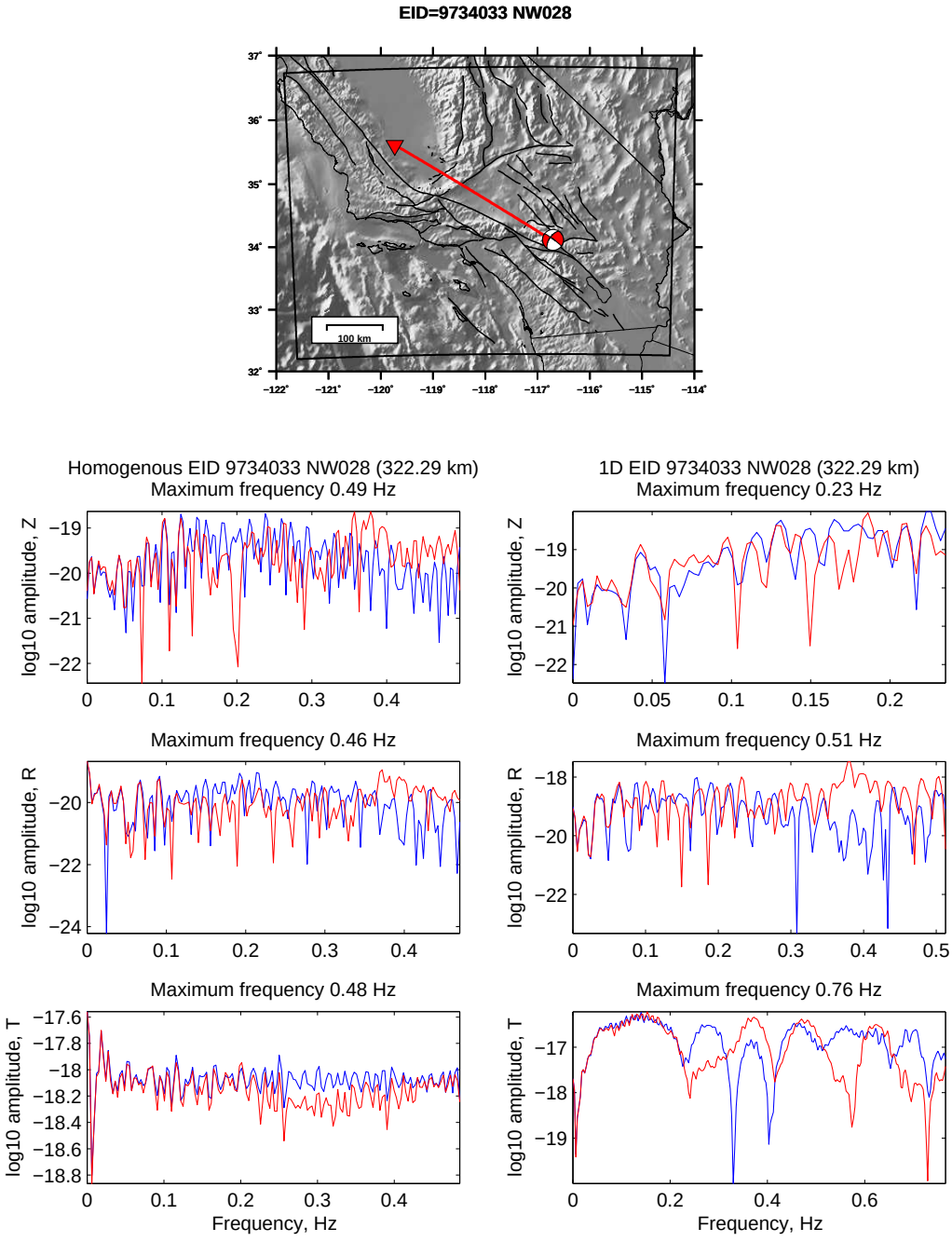

(a) Homogeneous (b) 1D

Figure A.7: Amplitude spectra for waveforms in Figure 3.35.

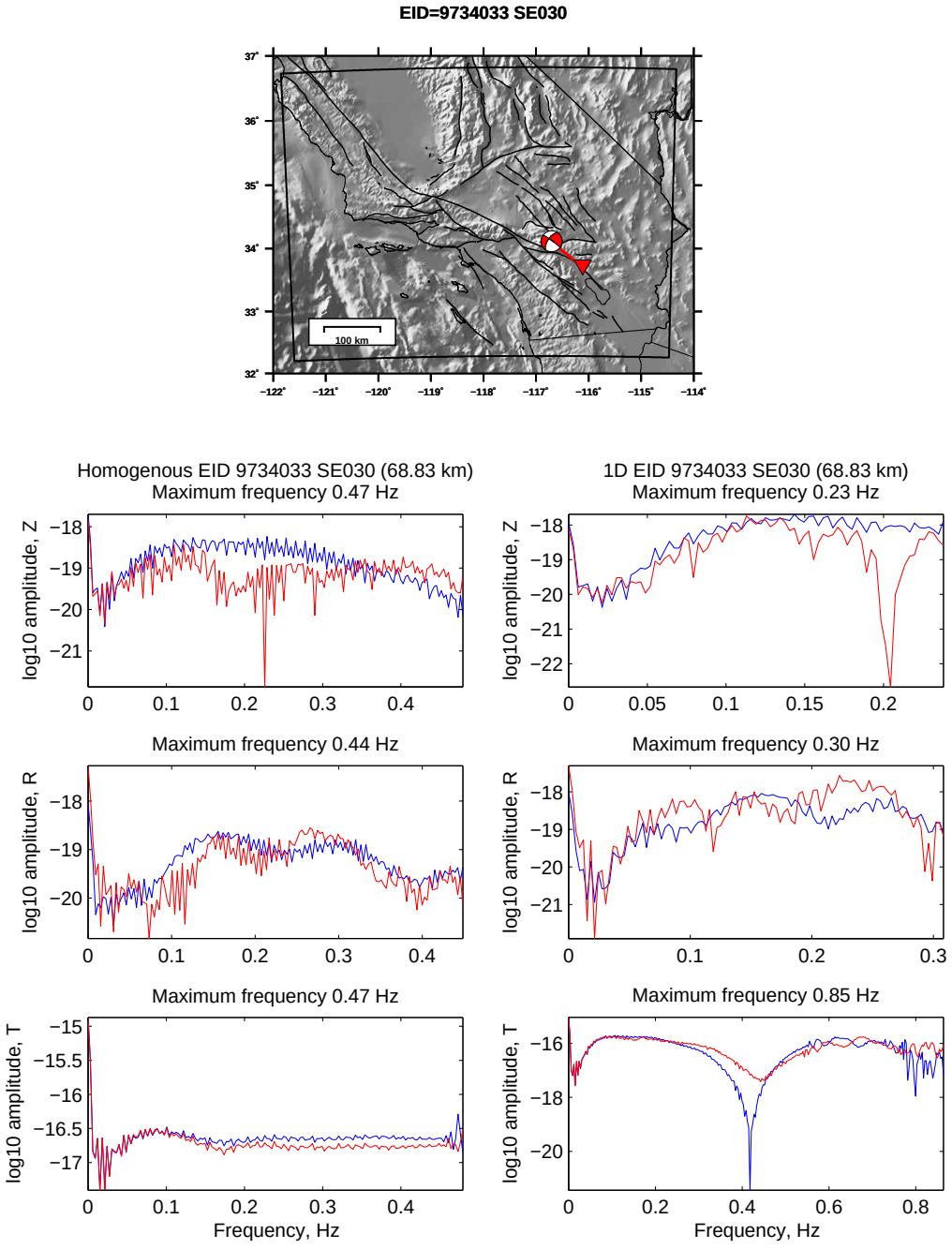

(a) Homogeneous (b) 1D

Figure A.8: Amplitude spectra for waveforms in Figure 3.21.

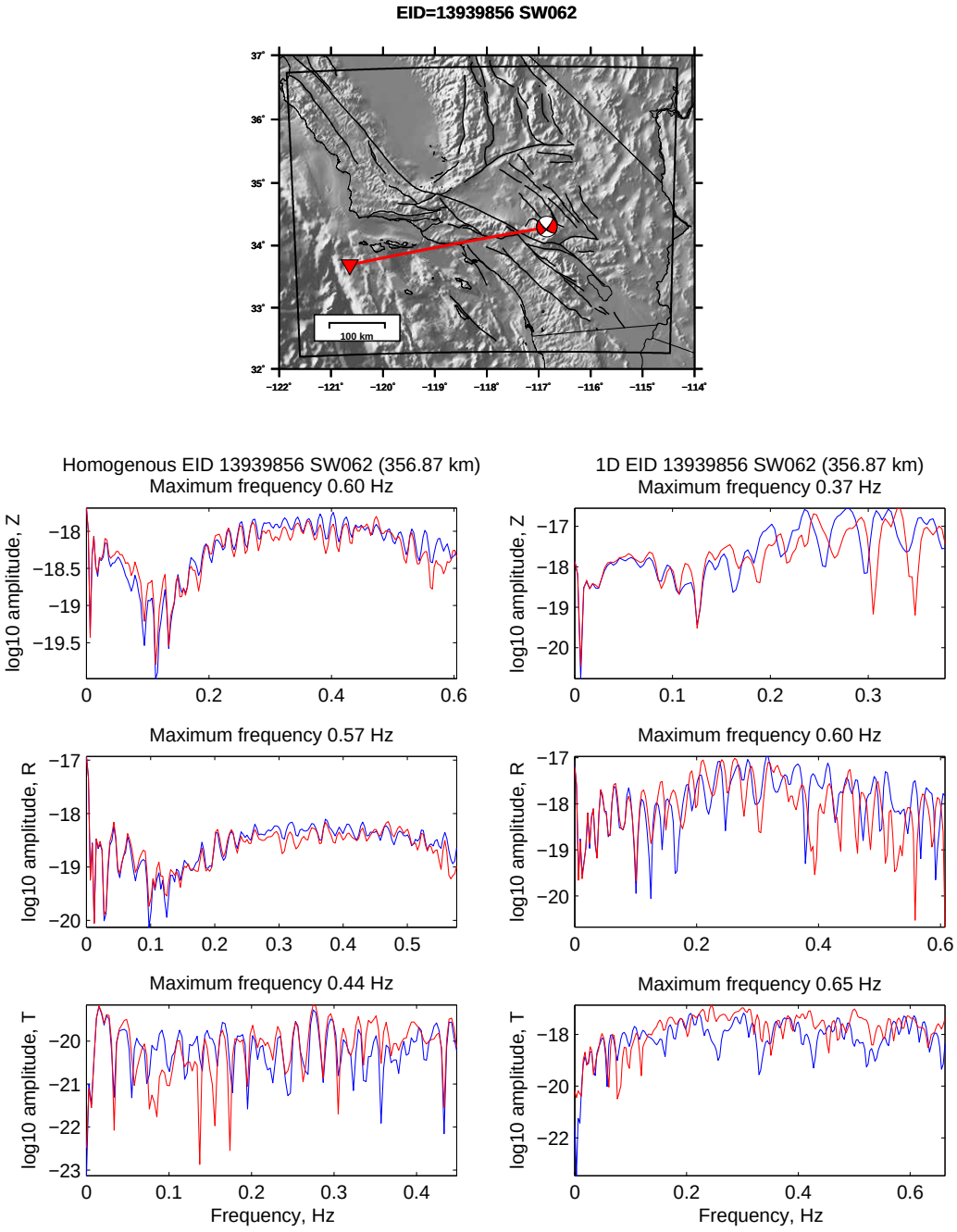

(a) Homogeneous (b) 1D

Figure A.9: Amplitude spectra for waveforms in Figure 3.36.

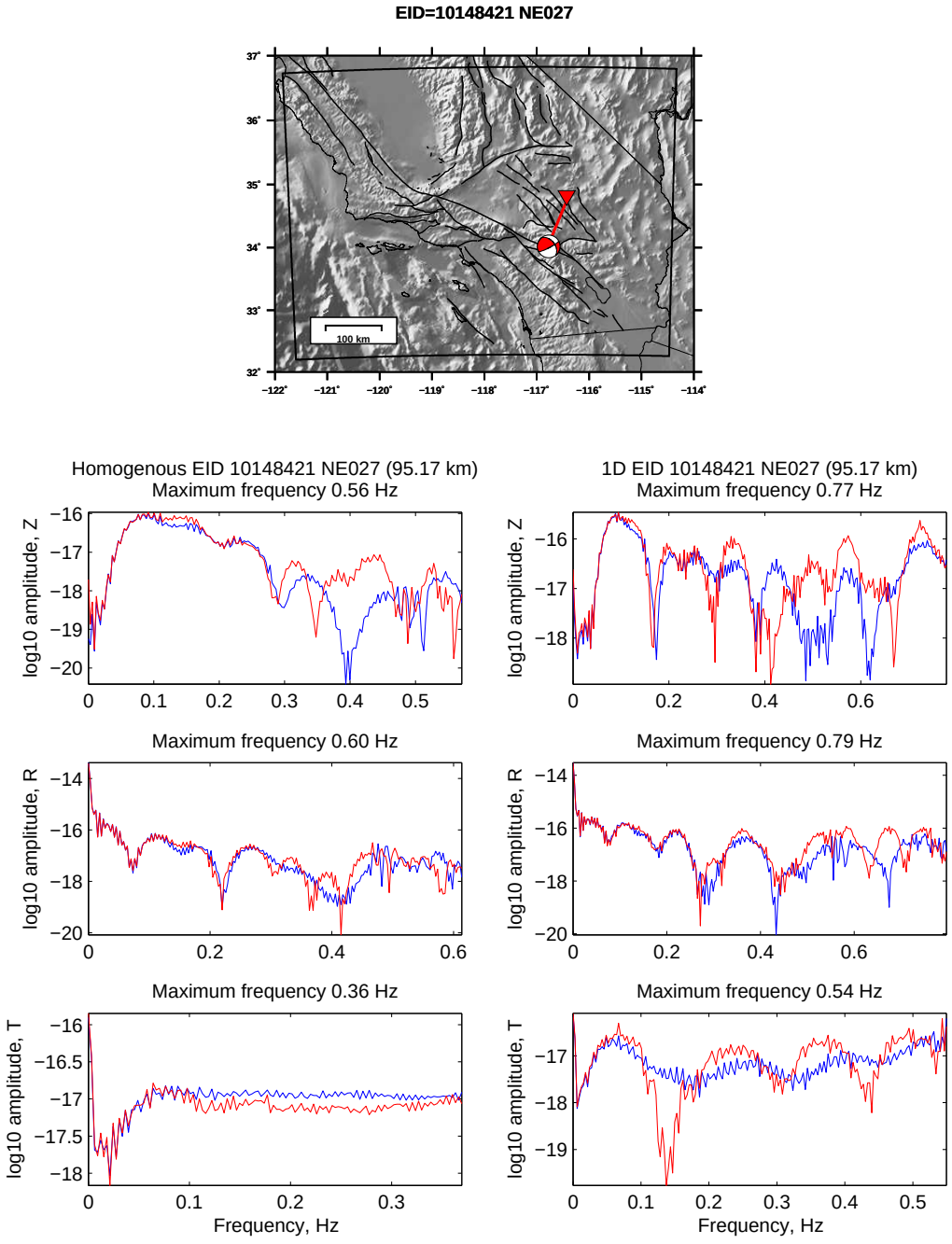

(a) Homogeneous (b) 1D

Figure A.10: Amplitude spectra for waveforms in Figure 3.37.

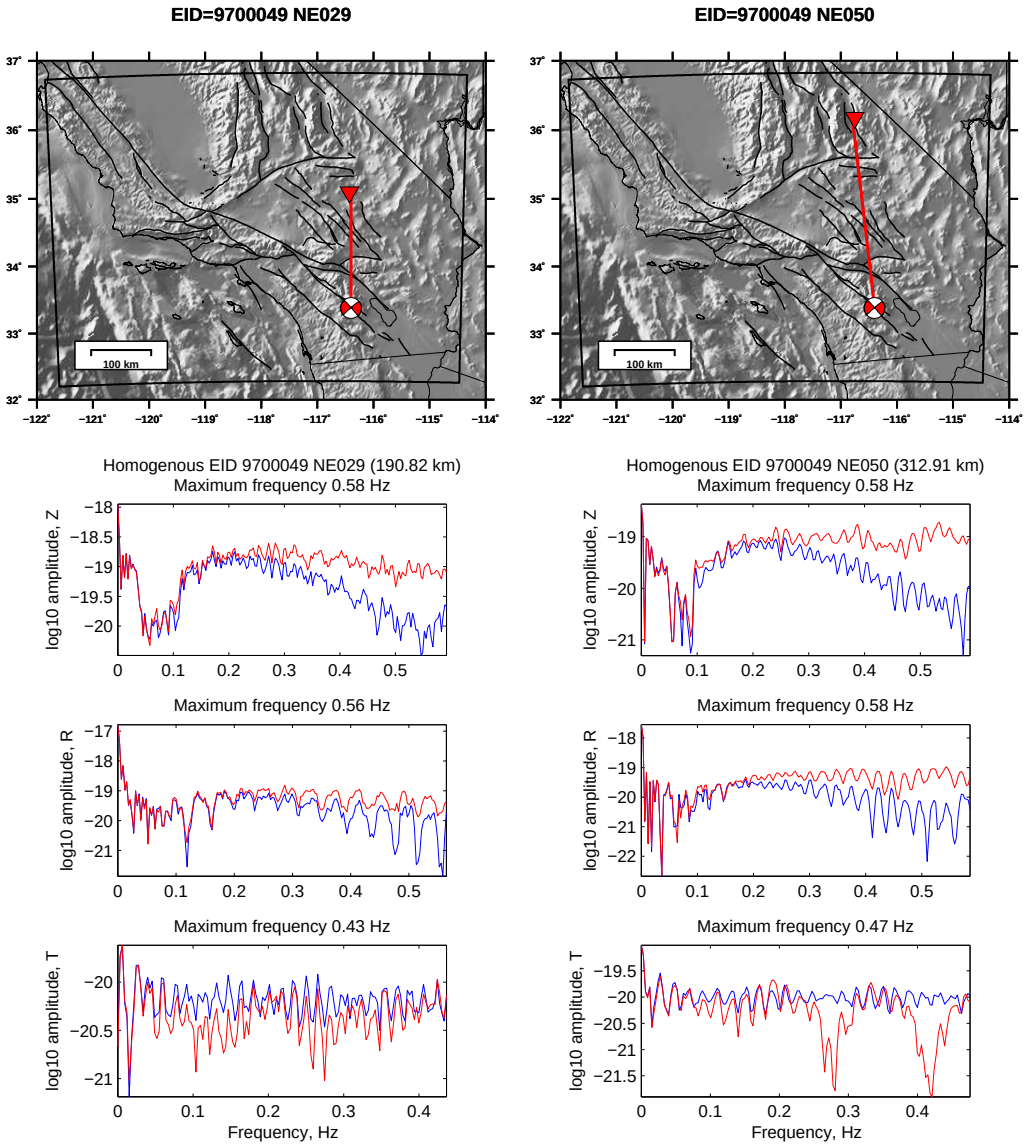

(a) NE029 (b) NE050

Figure A.11: Amplitude spectra for waveforms in Figure 3.38.

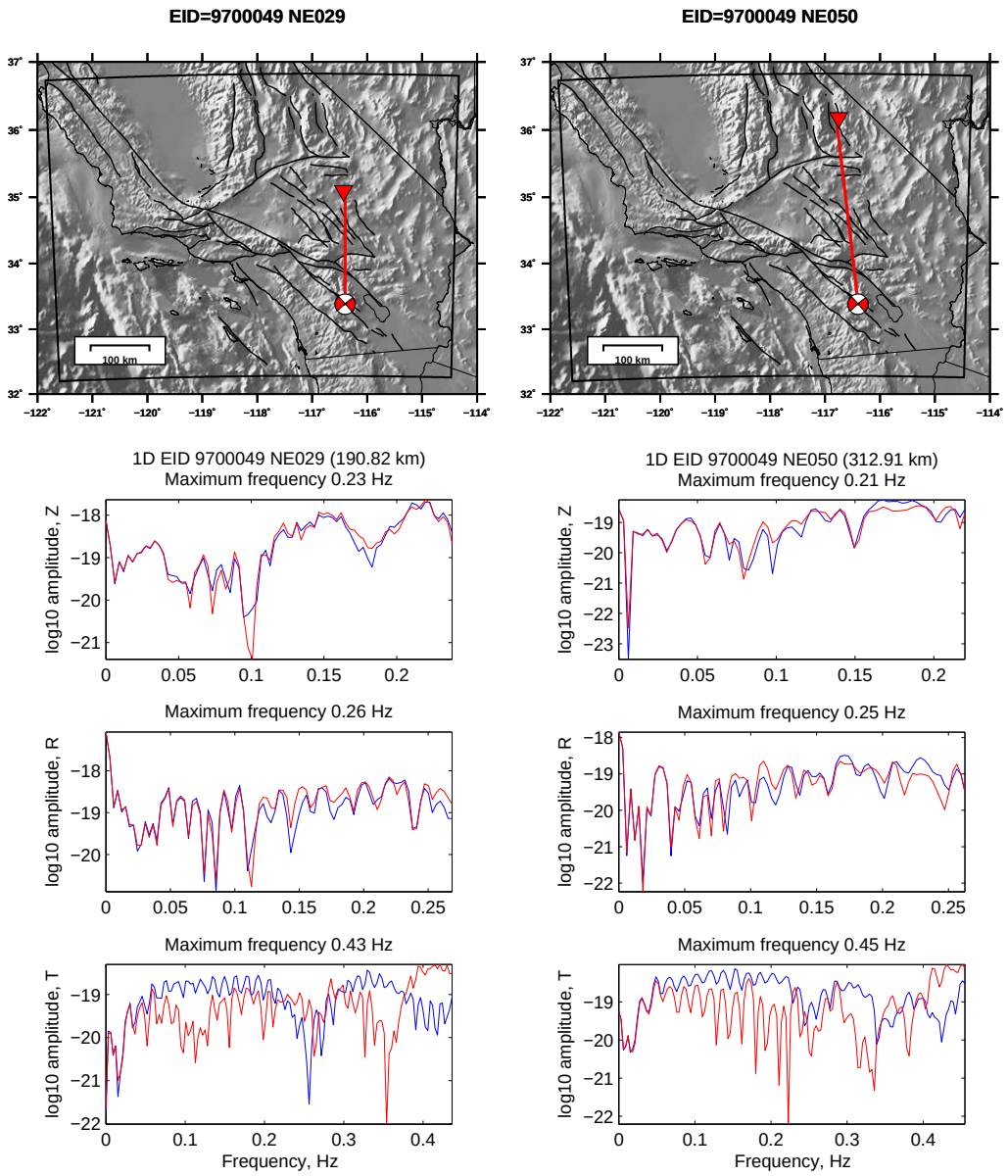

(a) NE029 (b) NE050

Figure A.12: Amplitude spectra for waveforms in Figure 3.39.

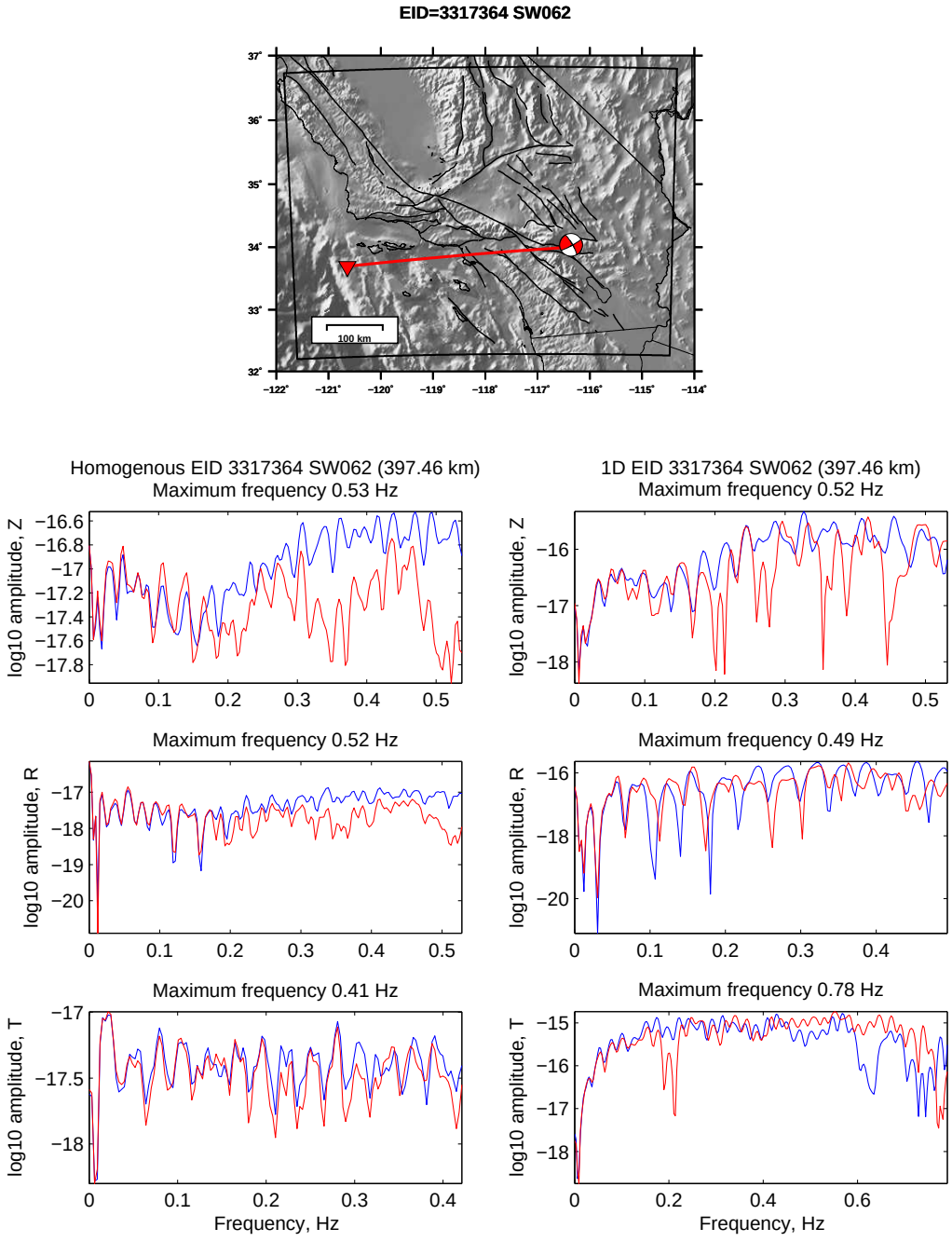

(a) Homogeneous (b) 1D

Figure A.13: Amplitude spectra for waveforms in Figure 3.40.